Characterization of Heterogeneous Reservoir Rocks Using Multi-scale Image Reconstruction and Octree Structures

Dissertation

for the award of the degree

„Doctor of Natural Sciences“

Doctorate in Geosciences

at the Faculty of Chemistry, Pharmaceutical Sciences, Geography and Geosciences of the Johannes Gutenberg University Mainz

Abolfazl Moslemipour

born in Gorgan, Iran

Mainz, (2024)

Supervisors:

Advisors:

Day of the oral examination: 22.07.2025

Printed and/or published with the support of the German Academic Exchange Service.

Acknowledgements

While completing this PhD thesis, I was supported by many people, who I want to thank at this point.

I want to express my sincere thanks to my caring supervisors. …, my first supervisor, for his unconditional help, comments, discussions and generous support for this project and …, my second supervisor, for his valuable scientific guidance, many useful hints and help during this thesis and my time at JGU. In Addition to be great leaders, I found them as passionate friends and colleagues with high level of professional ethics.

In addition, special thanks to … for his thoughtful consultancy and instructive collaboration and his valuable comments and suggestions. Furthermore, thanks … for his valuable comments and suggestions that have enhanced the applicability of the present study.

Also, I want to thank the DAAD for awarding Co-tutelle Doctoral Scholarship to carry out this research at JGU.

I want to acknowledge Math2Market for providing us with the GeoDict software license, which enabled us to perform image processing, modeling, and simulations. Also, I want to acknowledge DESY (Hamburg, Germany), a member of the Helmholtz Association HGF, for the provision of experimental facilities. Parts of this thesis were carried out at the PETRA III synchrotron storage ring and we would like to thank … for assistance in using the photon imaging beamline HEREON IBL P05. In addition, I would like to thank … and … for their all support and acquisition of a micro-CT scanner under grant number 411334776.

Then, I would like to thank my parents who endured my absence with patience, while keeping their encouraging support to me following my dreams.

Finally, I wish to express my deepest gratitude to my wife who stood by me through this journey, and none of this would have been possible without her selfless support and sacrifice.

Abstract

Researchers commonly use multi-scale modeling to characterize heterogeneous rock samples. Despite their utility, these models face significant challenges. One major issue is the tradeoff between resolution and field of view (FoV) during imaging. Although various novel approaches attempt to address this issue, they often produce unrealistic results or incur high computational costs. In this study, we present methods for the multi-scale reconstruction of pore networks and images for three heterogeneous rocks using octree structures. We performed multi-scale image reconstruction on Berea Sandstone (BS) and Edward Brown Carbonate (EBC) rocks, and multi-scale reconstruction of pore networks on Indiana Limestone (ILS) rock. We scanned all samples at low (LR) and high (HR) resolutions using X-ray microtomography. In our novel multi-scale direct numerical simulation (DNS) reconstruction approach, we reconstructed multi-scale images using the Octree structure to reduce computational cost. In addition, we also presented a novel method for multi-scale pore network modeling (PNM) reconstruction using an artificial neural network to connect the PNMs at different scales in octree structure. The results showed good agreement with the HR images and experimental properties. We concluded that using the Octree structure decreased runtime up to three times for the multi-scale DNS reconstruction. For multi-scale PNM reconstruction, the runtime was nearly equal to the normal method. Additionally, the memory used for the multi-scale DNS reconstruction was reduced by 20 to 130 times, and for multi-scale PNM reconstruction, by up to three times. To further reduce computational costs, we also introduced new multi-scale upscaling methods. The first method, which utilized the Octree structure and unresolved clusters, was applied to the BS rock images for multi-scale DNS upscaling. The second method was applied to the ILS rock images for multi-scale PNM upscaling. We concluded that the multi-scale DNS upscaling method, while maintaining accuracy, reduced runtime up to eight times and memory consumption up to two times. Similarly, the multi-scale PNM upscaling method reduced runtime up to two times and memory consumption about three times, without reducing accuracy.

Keywords:

Digital Rock Physics, Heterogeneous rock, Multi-scale reconstruction, Octree, Multi-scale modeling, Memory consumption, Run time, Artificial Neural Network

چکیده

محققان معمولاً از مدل‌سازی چند مقیاسی برای توصیف نمونه‌های سنگ ناهمگن استفاده می‌کنند. علیرغم کاربرد آنها، این مدل ها با چالش های قابل توجه ای روبرو هستند. یکی از مسائل مهم، مبادله بین وضوح و میدان دید (FoV) در طول تصویربرداری است. اگرچه رویکردهای جدید مختلف سعی در پرداختن به این موضوع دارند، اما اغلب نتایج غیرواقعی تولید می‌کنند یا هزینه‌های محاسباتی بالایی را متحمل می‌شوند. در این مطالعه، ما روش‌هایی را برای بازسازی چند مقیاسه شبکه حفرات و تصاویر برای سه سنگ ناهمگن با استفاده از ساختارهای درخت هشت تایی[1] ارائه می‌کنیم. ما بازسازی تصویر چند مقیاسه را روی سنگ‌های ماسه‌سنگ بریا (BS) و کربنات ادوارد براون (EBC) و بازسازی چند مقیاسه شبکه حفرات را روی سنگ آهک ایندیانا (ILS) انجام دادیم. ما تمام نمونه ها را با وضوح کم (LR) و بالا (HR) با استفاده از میکروتوموگرافی اشعه ایکس اسکن کردیم. در رویکرد جدید شبیه‌سازی عددی مستقیم چند مقیاسه (DNS)، تصاویر چند مقیاسه را با استفاده از ساختار درخت هشت تایی برای کاهش هزینه‌های محاسباتی بازسازی کردیم. علاوه بر این، ما همچنین یک روش جدید برای بازسازی شبکه حفرات چند مقیاسه (PNM) با استفاده از یک شبکه عصبی مصنوعی برای اتصال شبکه حفرات در مقیاس‌های مختلف در ساختار درخت هشت تایی ارائه کردیم. نتایج تطابق خوبی با تصاویر HR و ویژگی های تجربی نشان داد. ما به این نتیجه رسیدیم که استفاده از ساختار درخت هشت تایی زمان اجرا را تا سه برابر برای بازسازی چند مقیاسه DNS کاهش داد. برای بازسازی چند مقیاسه PNM، زمان اجرا تقریباً برابر با روش معمولی بود. علاوه بر این، حافظه مورد استفاده برای بازسازی چند مقیاسه DNS، 20 تا 130 برابر و برای بازسازی چند مقیاسی PNM تا سه برابر کاهش یافت. برای کاهش بیشتر هزینه‌های محاسباتی،

1 Octree

روش‌های جدید ارتقاء مقیاس چند مقیاسه را نیز معرفی کردیم. روش اول، که از ساختار درخت هشت تایی و خوشه‌های حل نشده استفاده می‌کرد، روی تصاویر سنگ BS برای ارتقاء مقیاس DNS چند مقیاسه اعمال شد. روش دوم بر روی تصاویر سنگ ILS برای ارتقاء مقیاس PNM چند مقیاسه اعمال شد. ما به این نتیجه رسیدیم که روش ارتقاء مقیاس DNS چند مقیاسه، با حفظ دقت، زمان اجرا را تا هشت برابر و مصرف حافظه را تا دو برابر کاهش داد. به طور مشابه، روش افزایش مقیاس PNM چند مقیاسه، زمان اجرا را تا دو برابر و مصرف حافظه را حدود سه برابر، بدون کاهش دقت، کاهش داد.

کلمات کلیدی:

فیزیک دیجیتال مغزه، سنگ ناهمگن، بازسازی چند مقیاسه، درخت هشت تایی، مدل سازی چند مقیاسه، مصرف حافظه، زمان اجرا، شبکه عصبی مصنوعی

Zusammenfassung

Zur Charakterisierung heterogener Gesteinsproben verwenden Forscher häufig mehrskalige Modelle. Trotz ihres Nutzens stehen diese Modelle vor erheblichen Herausforderungen. Ein Hauptproblem ist der Kompromiss zwischen Auflösung und Sichtfeld (FoV) bei der Bildgebung. Obwohl verschiedene neue Ansätze versuchen, dieses Problem zu lösen, führen sie oft zu unrealistischen Ergebnissen oder verursachen hohe Rechenkosten. In dieser Studie stellen wir Methoden für die mehrskalige Rekonstruktion von Porennetzwerken und Bildern für drei heterogene Gesteine unter Verwendung von Octree-Strukturen vor. Wir haben eine mehrskalige Bildrekonstruktion für Berea Sandstone (BS) und Edward Brown Carbonate (EBC) sowie eine mehrskalige Rekonstruktion von Porennetzen für Indiana Limestone (ILS) durchgeführt. Wir haben alle Proben mit niedriger (LR) und hoher (HR) Auflösung mittels Röntgenmikrotomographie gescannt. In unserem neuartigen Multiskalen-Rekonstruktionsansatz der direkten numerischen Simulation (DNS) rekonstruierten wir Multiskalenbilder unter Verwendung der Octree-Struktur, um die Rechenkosten zu senken. Darüber hinaus haben wir eine neuartige Methode für die mehrskalige Rekonstruktion von Porennetzwerken (PNM) vorgestellt, bei der ein künstliches neuronales Netzwerk verwendet wird, um die PNMs auf verschiedenen Skalen in der Octree-Struktur zu verbinden. Die Ergebnisse zeigten eine gute Übereinstimmung mit den HR-Bildern und experimentellen Eigenschaften. Wir kamen zu dem Schluss, dass die Verwendung der Octree-Struktur die Laufzeit für die DNS-Rekonstruktion in mehreren Maßstäben um das Dreifache verringert. Bei der mehrskaligen PNM-Rekonstruktion war die Laufzeit fast genauso lang wie bei der normalen Methode. Außerdem konnte der Speicherbedarf für die DNS-Rekonstruktion um das 20- bis 130-fache und für die PNM-Rekonstruktion um das bis zu 3-fache reduziert werden. Um die Rechenkosten weiter zu senken, haben wir auch neue Multiskalen-Upscaling-Methoden eingeführt. Die erste Methode, die die Octree-Struktur und unaufgelöste Cluster nutzte, wurde auf die BS-Felsbilder für die Multiskalen-DNS-Upscaling angewandt. Die zweite Methode wurde auf die ILS-Felsbilder für die Multiskalen-PNM-Hochskalierung angewandt. Wir kamen zu dem Schluss, dass die Multiskalen-DNS-Upscaling-Methode unter Beibehaltung der Genauigkeit die Laufzeit um das Achtfache und den Speicherverbrauch um das Zweifache reduzierte. In ähnlicher Weise reduzierte die Multiskalen-PNM-Upscaling-Methode die Laufzeit um das Zweifache und den Speicherverbrauch um das Dreifache, ohne die Genauigkeit zu verringern.

Schlüsselwörter:

Digitale Gesteinsphysik, Heterogenes Gestein, Mehrskalige Rekonstruktion, Octree, Mehrskalige Modellierung, Speicherverbrauch, Laufzeit, Künstliches Neuronales Netz

Decleration

No portion of the work referred to in the thesis has been submitted in support of an application for another degree or qualification of this or any other university or other institute of learning. In addition, I confirm that all work provided is entirely my own and has not been copied, plagiarized, or otherwise derived from another person’s work without proper citation or acknowledgment.

Publications

The presented journal format thesis is comprising three peer-reviewed papers and one manuscript as direct outcomes of the PhD thesis. The first paper has been published and available online, while the second and third papers are still under review. The fourth paper is in preparation for submission to a journal.

1. "Image-Based Multi-scale Reconstruction of Unresolved Microporosity in 3D Heterogeneous Rock Digital Twins Using Cross-Correlation Simulation and Watershed Algorithm" *Transport in Porous Media* 151, no. 10 (2024): 2215-2240.

   My contribution to this paper included conceptualization, data collection, methodology, formal analysis and investigation, validation, writing the first draft, and writing - review and editing. Moreover, preliminary versions of this paper were presented in two different conferences: the first one as poster at Interpore 2023, the 15th Annual International Conference on porous media, Edinburg, Scotland and the second one as oral presentation at Interpore German Chapter Meeting 2023, Catholic University of Eichstätt-Ingolstadt, Germany. This paper aims to present a novel and more efficient and robust method for reconstructing multi-scale images of two heterogeneous rock samples: a sandstone and a carbonate. The new introduced approach addresses issues found in previous studies such as the need for high- and low-resolution scans of specific rock locations, accurate multi-scale image reconstruction, and high computational costs. Computations were performed only on unresolved regions and reduced computational costs using the watershed algorithm. By considering new overlapping areas in the cross-correlation function equation, connections were preserved between micro-micro and macro-micro pores. The best match templates containing a significant number of micro-pores were selected. First, the LR images were segmented into three phases: pore, matrix, and unresolved porosity. Then, the watershed segmentation algorithm was used to divide the unresolved region into smaller parts, called unresolved templates. This technique reduces computational costs. Next, best-match templates of the same size

from the HR images were extracted using a novel approach based on the cross-correlation function equation to replace the low-resolution images. Unlike previous similar study, this approach can extract the best match template in any direction, uses a specific overlapping area to preserve connections between pores of different scales (macro-macro and micro-macro links), and selects templates with an acceptable number of micro-pores. Furthermore, petrophysical and morphological image properties were calculated and validated against the high-resolution image properties.

2. "Efficient Multi-Scale Image Reconstruction of Heterogenous Rocks with Unresolved Porosity Using Octree Structures" *Computational Geosciences* 29, no. 3 (2025): 24.

   My contribution to this paper included conceptualization, data collection, methodology, formal analysis and investigation, validation, writing the first draft, and writing - review and editing. Moreover, a preliminary version of this paper has been presented as an extended abstract in EAGE Annual 2024, the 85th Conference & Exhibition, Oslo, Norway. In this paper, the approach introduced in paper 1 (CWMR) was modified and presented a new model for multi-scale image reconstruction using the Octree structure, which reduces memory consumption and computational cost. This approach is called Octree CCSIM-based Watershed Multi-scale Reconstruction (OCWMR). Therefore, initially the low-resolution image was segmented into three distinct phases: pore, matrix, and unresolved porosity. Then, the voxel size of the unresolved phase was reduced and preserved the voxel size of the pore and the matrix phases constant, and thus the low-resolution image was transformed into an Octree structure. Subsequently, the watershed segmentation algorithm was employed to break down the unresolved regions of the image into smaller sections known as unresolved templates. For more accurate multi-scale images, a sensitivity analysis was performed on the watershed algorithm parameters. Following this initial optimization, the cross-correlation function equation was used to find best-match templates from high-resolution images. These thus selected templates were then integrated into the Octree structure. Finally, this structure was converted to a single resolution image to reconstruct the

multi-scale image. 10 different realizations were reconstructed using the OCWMR approach. Furthermore, petrophysical and morphological image properties were calculated and validated against the reconstructed image properties using the classical CWMR approach.

3. "Multi-scale pore network fusion and upscaling of microporosity using artificial neural network." Marine and Petroleum Geology 177 (2025): 107349.

   My contribution to this paper included conceptualization, data collection, methodology, formal analysis and investigation, validation, writing the first draft, and writing - review and editing. Moreover, a preliminary version of this paper has been presented as oral presentation in Interpore 2023, the 15th Annual International Conference on porous media, Edinburg, Scotland. In this paper, a novel fusion and a novel upscaling method were presented for multi-scale pore network modeling (PNM) that addresses three basic problems: computational cost, accuracy, and the connection between rock scales. This method divides the multi-scale image into two phases: resolved porosity with a large voxel size and unresolved area with a small voxel size. It then extracts the PNM from the resolved porosity and generates stochastic PNMs for unresolved areas. The PNM extracted from the resolved porosity contains large pores, while the stochastic PNM of unresolved area includes small pores. Next, an artificial neutral network (ANN) is used trained on the pores and throats of the PNM extracted from the HR image. This ANN connects the PNMs of resolved and unresolved porosities efficiently. This paper also introduces a new upscaling method for the reconstructed multi-scale PNM. This method reduces computational cost while preserving accuracy. It achieves this by introducing base pores and adding new throats in place of existing pores and throats in unresolved areas. The effectiveness of the generated multi-scale PNM and upscaled PNM is compared with one of previous studies to assess the importance of connection between scales. This method is also validated by comparing results with laboratory results of the rock sample.

Table of contents

List of figures

List of tables

Chapter 1

Introduction

1.1 Introduction

One of the primary challenges in the petroleum industry today is computing reservoir rock properties at a micro-scale. This task is crucial for understanding the behavior of large-scale porous media. Over the past decade, Digital Rock Physics (DRP) has advanced rapidly, allowing for a deeper understanding of displacement processes in reservoirs. As a result, many companies in the petroleum industry have developed their own digital core technologies. The rise of this method stems from the ability to construct highly complex rock models. These models not only replicate the geometry of the rocks but also effectively simulate multiphase flows, offering significant predictive power [1, 2].

In this method, the process begins with constructing a 2D or 3D model using calculated parameters and functions. These functions assess the differences between the properties of the constructed model and the actual rock. After constructing the model, researchers calculate the fluid flow properties on the model using different approaches. There are several approaches for 2D or 3D model reconstruction, with most relying on random models and rock formation processes. It's essential to use specific functions to minimize the differences between the original model and the 2D or 3D model to achieve accurate results. Depending on the model and the reservoir rock, selecting one or more appropriate functions is crucial for reliable outcomes. Additionally, some of these functions utilize multi-processing methods and applications based on graphical processing units, which significantly increase computational speed.

Various DRP methods are currently used to calculate fluid flow pressure and velocity in porous media. These methods fall into two main categories. The first category involves solving flow equations directly on images. The second category uses a network of pores and throats. The first method, known as Direct Numerical Simulation (DNS), directly performs calculations on images. The second method is called Pore Network Modeling (PNM). DNS aims to solve flow-governing equations using a digital 3D voxel-based representation of the pore space with appropriate boundary conditions. In contrast, PNM simulates porous media by studying fluid transport within a network of pores and throats. In this model, pores represent void spaces, while throats represent the connections between them. These methods are widely used in fields like petroleum engineering, geoscience, geology, purification, and fuel cell research. It predicts the geometrical properties of porous media on a macroscale, such as porosity, permeability, diffusion, formation

resistance factors, capillary pressure, and thermal conductivity. Additionally, DRP accurately describes flow mechanisms at the microscale, including multiphase flow, wettability, trapped phases, dissolution, and convection at the pore level [3].

One of the most intriguing approaches in DRP is the use of artificial intelligence and neural networks. This technique can calculate various petrophysical and fluid flow properties of rocks, such as porosity, permeability, capillary pressure, relative permeability, and relative diffusivity. A key advantage of neural networks is their high processing speed, which reduces the need for powerful computing systems. They can also be applied in pre-processing tasks, such as enhancing image resolution. In image processing, one challenge is segmentation, particularly minimizing user bias when selecting threshold values. In the past, these values were chosen manually based on experimental results. Neural networks help automate and improve this process.

Moreover, artificial intelligence methods are highly effective in analyzing heterogeneous reservoir rocks, which often contain a wide range of pores, such as natural vugs and fractures. These rocks are particularly important because they hold large volumes of oil reserves. However, understanding their behavior is challenging due to the complexity of their geometry. Digital Rock Physics (DRP) plays a crucial role in addressing this challenge. The variation in pore sizes within heterogeneous rocks sets them apart from other rock types. To address this complexity, multi-scale modeling techniques have been developed, allowing for more accurate modeling of heterogeneous rocks.

All multi-scale models have been applied to images with a limited Field of View (FoV). As the FoV increases, the number of pixels (voxels) grows significantly, making it nearly impossible to model such large domains. However, some methods can reduce the number of pixels while preserving the void spaces in the image. One such method is the Octree approach, which combines images with different resolutions to construct the desired image. This technique divides the voxels of an image into eight smaller, equal-sized regions in 3D space, and this process can continue as needed. Although the Octree method has not been used for pore-scale modeling until now, this study will explore its application in modeling heterogeneous multi-scale rocks.

1.2 Research statement

Evaluating flow and particle transport at the micro/micron and mesoscale levels is crucial for understanding the behavior of porous media on the Darcy scale. However, laboratory methods often involve high computational costs and require significant time to achieve the desired results. To address these challenges, numerical methods have emerged as valuable tools for studying porous media. These methods have numerous applications in fields such as petroleum engineering, chemical engineering, and beyond. Micro/micron and mesoscale models are particularly useful for revealing the effects of flow and transport within porous media. They also provide a means to calculate Darcy scale properties. A key driver of progress in this area is the advancement of 3D imaging techniques, including CT scanning, scanning electron microscopy (SEM), and Focused Ion Beam (FIB) methods. These techniques allow researchers to extract various properties from images of porous spaces, such as the distribution and relationship between solid and pore phases, which significantly impact chemical processes. Flow properties can also be obtained directly or through Pore Network Modeling (PNM). One challenge in this field is the presence of pores of different sizes, especially in heterogeneous rocks. Capturing all pores in a large Field of View (FoV) is difficult due to the tradeoff between resolution and FoV. To overcome this limitation, it is necessary to model rock space in a multi-scale form by combining multiple images with different resolutions. The Octree method is one effective approach for producing images with both large FoV and high resolution. This method replaces high-resolution images in regions where the pores are very small, making it a valuable tool for multi-scale modeling. However, studies conducted so far have not clearly defined scale connectivity, often relying on a trial-and-error approach to achieve the desired results. Establishing clear scale connectivity is essential for general application across various cases. In light of these challenges, there is a need for new methods with high processing speeds for modeling heterogeneous rocks in a multi-scale form.

This research will present various methods for reconstructing and modeling heterogeneous rocks in a large FoV. These methods will utilize Octree structures and Artificial Neural Networks (ANN) to reconstruct and determine scale connectivity, accommodating a wide range of pore sizes. Additionally, to reduce computational costs and increase the accuracy of these methods, rock images at different scales will be combined to form an Octree image.

1.3 Objectives

This thesis aims to address several objectives. The first objective focuses on multi-scale modeling by constructing Octree images with a large FoV while reducing computational costs. The primary goal is to achieve multi-scale reconstruction and modeling of various heterogeneous rocks using DNS and PNM. This will involve the application of artificial intelligence and the Octree structure to identify optimal scale connectivity. Finally, the accuracy and speed of all methods will be compared, and the results of the models will be validated against high-resolution images and experimental data.

1.4 Research Questions

1. What are the benefits of using an octree structure?
2. How does combining multi-scale reconstruction and modeling using both DNS or PNM methods along with octree structure impact the speed and accuracy of calculations in creating optimal scale connectivity?
3. What properties should be used as inputs to an ANN to establish scale connectivity in PNM?
4. What are the pros and cons of DNS and PNM methods for multi-scale modeling?

1.5 Assumptions

1. The octree structure uses fewer voxels than a standard image but retains all the image details in voxels of varying sizes. This results in high modeling accuracy with reduced computational cost.
2. Multi-scale modeling using the DNS method closely aligns with the actual rock behavior because it performs direct calculations on the primary image. Although the DNS method is computationally intensive, the new reconstruction and modeling technique reduces computational cost by minimizing the number of voxels in the final image. Similarly, multi-scale networks reconstructed using PNM align well with the actual rock behavior. However, the inherent simplifications in the PNM method may lower calculation accuracy. These simplifications, though, help to reduce computational costs in PNM approaches.

Additionally, the new method for establishing scale connectivity further decreases computational speed by reducing the number of pores and throats in the final PNM.

3. Two properties are essential for reconstructing multi-scale networks: the diameter of the pores and their 3D coordinates. The ANN uses this information to decide whether to place a throat between them.
4. The DNS method offers higher accuracy than PNM methods because it directly performs multi-scale modeling by merging image data. However, this method has a high computational cost. In contrast, the PNM method is faster and uses less memory due to its simplified assumptions. Yet, because it relies on simplified representations of pores and throats, the PNM method has lower accuracy than DNS.

1.6 Dissertation structure

This doctoral dissertation is organized into five chapters, summarized as follows:

Chapter one introduces the importance and methods of multi-scale modeling. Chapter two reviews studies on reconstruction, multi-scale modeling, octree structures, and artificial intelligence. Chapter three explains the methods used for multi-scale reconstruction and multi-scale modeling, including DNS and PNM. Chapter four presents the results of the modeling and their interpretations. Finally, chapter five offers research conclusions and suggestions for future studies.

Chapter 2

Literature review

2.1 Pore-scale modeling

The unbiased quantification of porous media properties is essential in various applications such as hydrology [4], geosciences and petroleum engineering [1, 5-9], underground hydrogen storage [10], carbon capture and storage [11], soil science [12], biology [13], and CO_2 injection [14, 15]. A large percentage of rocks in the world have quite heterogeneous structures (e.g., tight sandstone, shale and carbonate rock) [16-19]. Heterogeneous rock samples have pores at various scales. Computed tomography (CT) scanner (medical or micro-CT scan), Scanning Electron Microscope (SEM), and Focused Ion Beam SEM (FEB-SEM) are the main pore geometry imaging techniques at distinct scales and FoVs. The inverse relationship between resolution and FoV in imaging devices makes it impossible to capture pores of different sizes in one image [20-22]. However, this is vital to include all pores in the pore scale modelling [23-25]. For example, smaller pores can alter the permeability and substantially increase the porosity of rocks, influencing single and multi-phase flow properties. Therefore, modelling heterogeneous rock samples at the pore scale is a challenging task due to the presence of pores at various scales. Two main numerical approaches can be used for modeling a porous medium at the pore scale [4, 26-36]. The first method is Direct Numerical Simulation (DNS), which entails numerically solving the governing equations by a 3D digital representation of a pore space and appropriate boundary conditions. Another approach is Pore Network Modeling (PNM), which is based on the modeling of an extracted network from images [21]. This method is based on the simplification of porous medium images to a series of spherical pores and cylindrical throats [32, 34]. It can preserve the accuracy while reducing the computational cost [32, 34, 37-39].

2.2 Multi-scale Modeling

Despite improvements in DNS and PNM approaches, the modeling of heterogeneous rocks is still complicated. Therefore, some techniques have been introduced to fuse images (for DNS modeling) or fuse pore networks (for the PNM approach) from various scales to reconstruct multi-scale images and multi-scale pore networks [21, 23, 40-43].

2.2.1 Multi-scale DNS

Many studies focus on using DNS to model rock samples [7, 27, 29, 31, 35, 36, 44, 45]. However, multi-scale DNS modelling can be implemented in various ways [23, 46]. For example, one can initially reconstruct a multi-scale image and then perform pore-scale modelling on it. In this way, two main methods have been proposed, including statistical data-driven based [47-51] and deep neural network-based models [52-59]. While deep neural network-based reconstructions offer proper multi-scale image results, they require a large amount of training data and high computational costs. Therefore, statistical methods are a more favorable option for achieving suitable multi-scale image reconstruction with fewer memory-consuming data and reduced computational costs.

Statistical reconstructions utilize statistical data collected from images at different scales to reconstruct a multi-scale image. Studies that have employed statistical techniques for multi-scale image reconstruction exhibit lower computational costs but often generate images significantly deviating from the actual rock structures. For example, Gerke et al. (2015) constructed a multi-scale image of shales by merging multiple images constructed stochastically [60]. The merging process involved substituting information from higher-resolution imaging methods into non-spatially resolved phases to obtain combined images at increasing resolutions. Three stochastically reconstructed images were overlaid with decreasing scale, and the final fused image highlighted the multi-scale pore geometry in the solids. A multi-scale image of tight sandstone was thus modelled by combining digital core images at two different scales [61]. A multi-scale tight porous medium was created by coupling digital cores of two different scales using clay particles as bridging constituents. The process involved two steps: reconstruction of a micron-scale and a nanometer-scale digital core image, and replacement of clay pixels in the micron-scale with the nanometer-scale image. This was a simplified treatment, as the structure of different clay types in tight oil sandstones may vary. The replacement process was based on randomness. Moreover, this approach demands a lot of memory and high computational cost. In another research, more realistic multi-scale images were generated [12]. Their process encompassed the rescaling and integration of 2D images into a cohesive structure through correlation functions and stochastic reconstruction. The final step was superimposing all phases into a single 2D image by substituting relevant pieces of micro-CT images into the macroscale image. However, some connectivity information for

small-resolution contrast images might have been lost during the superposition process. Elimination of such bias is extremely hard even with the improvement of the superposition approaches [12, 62]. Therefore, Ji et al. (2019) introduced a multicomponent superposition algorithm to integrate the reconstructed models of different phases in a shale rock [63]. They resampled the high-resolution (HR) image into the same size and resolution as the low-resolution (LR) image using a bi-cubic interpolation method. Subsequently, they considered some superposition assumptions for the rock phases. The final multi-scale model was reconstructed by integration of HR and resampled LR images according to these superposition assumptions. The limitation of their research was the randomness in the integration procedure.

Some studies aimed to enhance the accuracy of reconstructed images within the statistical reconstruction framework by incorporating certain assumptions. Although these assumptions elevated the computational costs, they yielded more realistic multi-scale models [64-68]. For example, Li et al. (2020) proposed a method to integrate HR and LR images by down-sampling a training image (TI) into grids [69]. They calculated the probability density function (PDF) and objective porosity for each grid, reconstructing the LR image with added constraints for large pores. However, the study's drawback was that the added HR structure deviated from reality, resulting in discrepancies in micro-macro connectivity and permeability results. Wang et al. (2018) introduced a local-similarity statistic reconstruction (LSSR) method for multi-scale image reconstruction, enhancing pore connectivity [70]. The method involved obtaining an LR tomogram, extracting a cylindrical sub-plug, and scanning it at high resolution for overlap. HR and LR image cubes were segmented, and dictionaries were trained using a sparse representation algorithm. Despite its efficacy, the drawback was the requirement for HR and LR scans from the same rock location for accurate reconstruction. Wu et al. (2019) also introduced an algorithm for constructing multi-scale images of heterogeneous rock samples [9]. They constructed first a 3D template of HR images. By utilizing this scan template and considering an overlap region (OL) on LR images, they subsequently computed the cross-correlation function (CCF) to select the best-matched pattern from the HR template, inserting it into the LR image. However, the template selection process on the LR image was deemed vague, and the overlap region on the resampled LR image lacked finer resolution information for optimal template matching on the HR image. Moreover, the OL is selected on the resampled LR image, which could not be used for finding the best match template on the HR image because it doesn’t contain any information about the finer

resolution. As a consequence, there is a significant discontinuity between macro-macro and micro-macro pores in the multi-scale images.

2.2.2 Multi-scale PNM

Various studies have been used multi-scale PNM to reconstruct a multi-scale model, some of which are summarized in the following. Jiang et al. in 2013, extracted the networks at 3 different scales by micro-CT scan images using the medial axis method, and modeled the equivalent network with larger dimensions according to the different FoV of each of these networks, but with characteristics of the microscale network. However, the number of pores in the network was a factor of the number of pores obtained from the grain density due to the reduction of computational time. Then they performed sensitivity analysis on this factor. Finally, they modeled 2D and 3D networks by combining these networks in equally selected sizes. The final 3D model is shown in Figure 2-1. One of the drawbacks of this research is the lack of validation with experimental data [71].

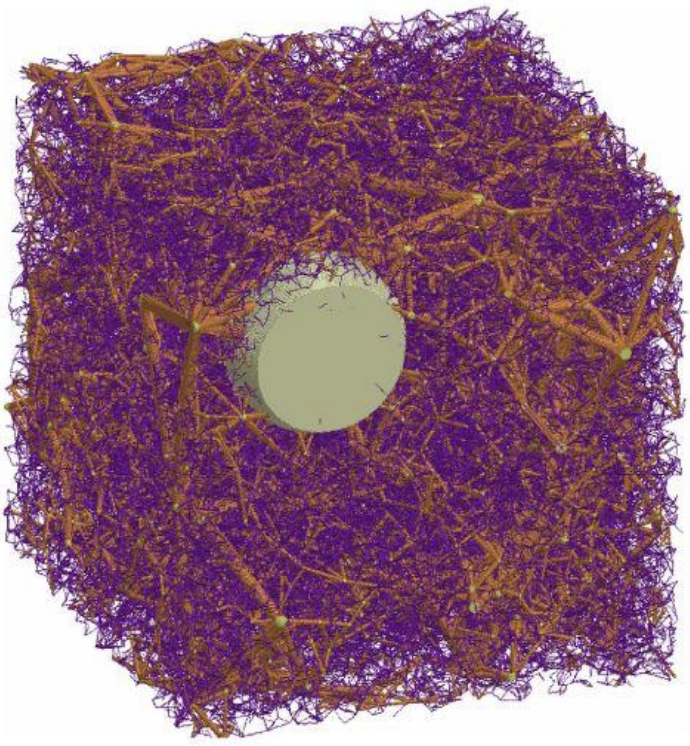

Figure 2-1 Multi-scale network, which was modeled with Jiang et al [71].

Prodanovich et al. in 2014, used a method similar to Jiang's method but paid more attention to the exact location of the micropores. Because the location of micropores affects the capillary pressure curves of the system. They guessed the exact location of the micropores from the micro-CT scan images. They validated their method on sandstone and limestone and plotted capillary pressure and relative permeability curves for the networks. They also investigated the properties of two-phase flows in the system and determined the difference between a network where the micropores are parallel or in series with large pores [72].

Using micro-CT scan images, Bultreys et al. first extracted the network containing the large pore using the maximal ball algorithm and modeled the network containing the micropores by considering the micro-links between the large pores. The micro-links, which were considered as small pores, were added in series and parallel with the network of large pores (Figure 2-2). To validate the models, two networks have been used, one ANN model and the other Estaillades carbonate rock [73]. In another study on two limestones, Bultreys et al. modeled the PNM using the previous method. However, in this study, they also compared the properties of the two-scale network with the single-scale network and finally performed the sensitivity analysis on the properties of the micropore network. Figure 2-3 shows the various methods used by various researchers to add a network of micropores to a network containing large pores [74].

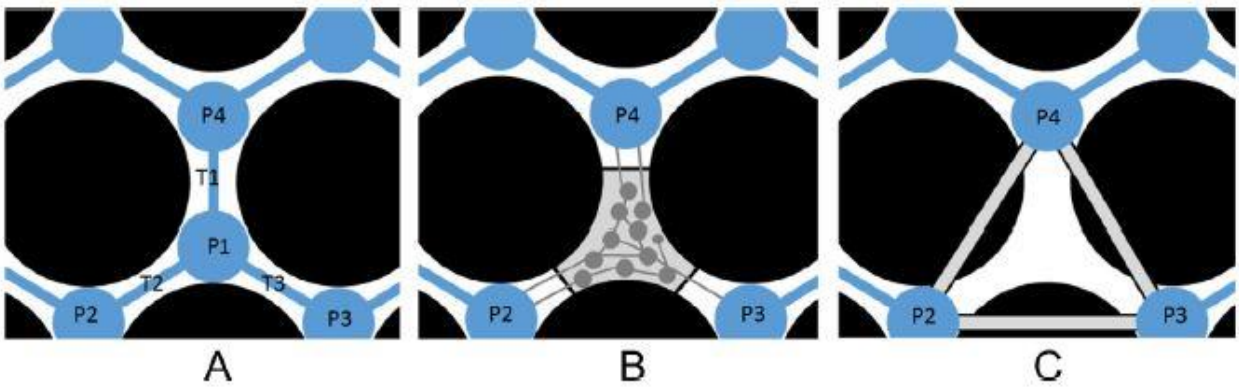

Figure 2-2 (A) The main network, which contains smaller and larger cavities. (B) In this figure, pore P1 is replaced by micropores (C) Micro-links are replaced by micropores [73]

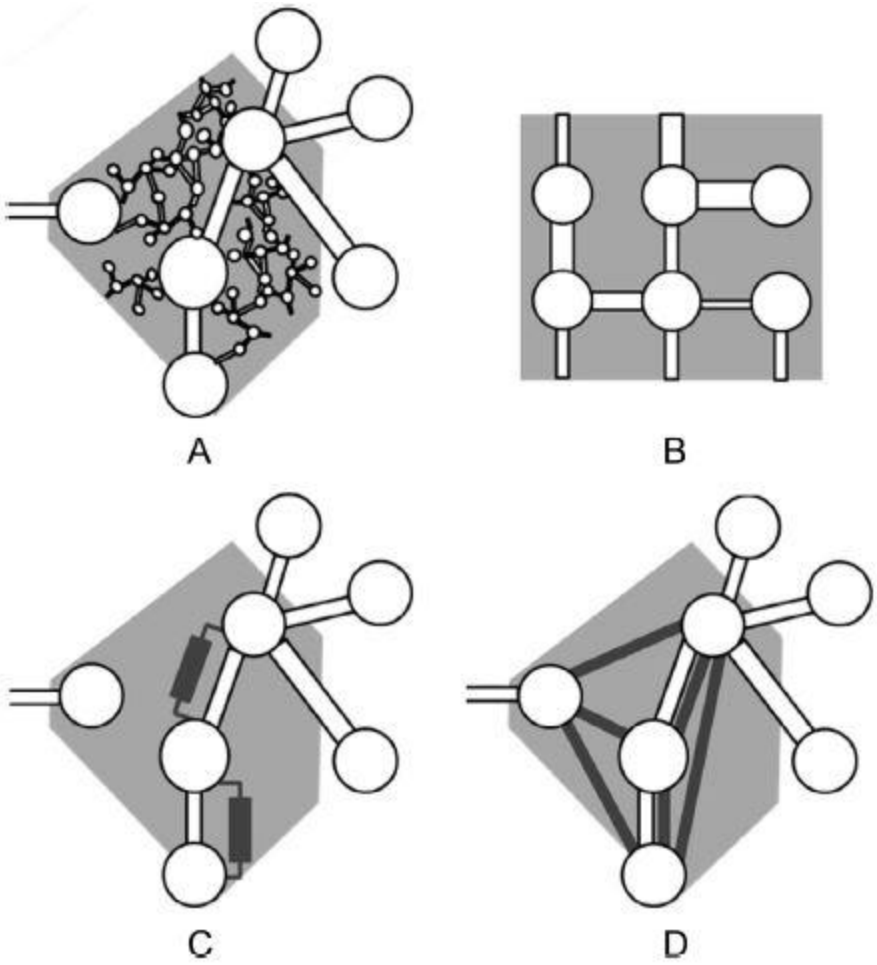

Figure 2-3 (A) PNM where micropores are located between large cavities. (B) PNM with upscaled micropores (C) PNM in which the micropore network is in the form of micro-link parallel to large pores (D) PNM in which the micropore network is in the form of micro-link series to large pores [74]

In 2019, Sadeghnejad and Gostick first modeled a regular equivalent network of carbonate rock without vugs, and then in various realizations added various numbers of vugs statistically to the system, which contained micropores. After investigating the results of various realizations, they concluded that despite the existence of vugs, the porosity increases but the permeability of the system will not necessarily increase. The permeability of the system increases greatly if the vugs present in the system create a percolation path in the rock network and act as a fracture in the rock (Figure 2-4). They also compared the results with the results of a vuggy carbonate rock, which has a good percolation and they achieved close and acceptable results [22]. Also in 2020, Moslemipour

and Sadeghnejad modeled an irregular dual-scale network of vuggy carbonate rock. They first extracted the meso network from the micro-CT images and built an equivalent network with large dimensions according to the extracted network properties from micro-CT images and vugs were then added in a novel way in this network using the extracted properties from medical CT scan images of rock (Figure 2-5). This shows the effect of vugs on the geometry and flow properties of a rock and provides more accurate information due to the heterogeneity of the constructed network [20].

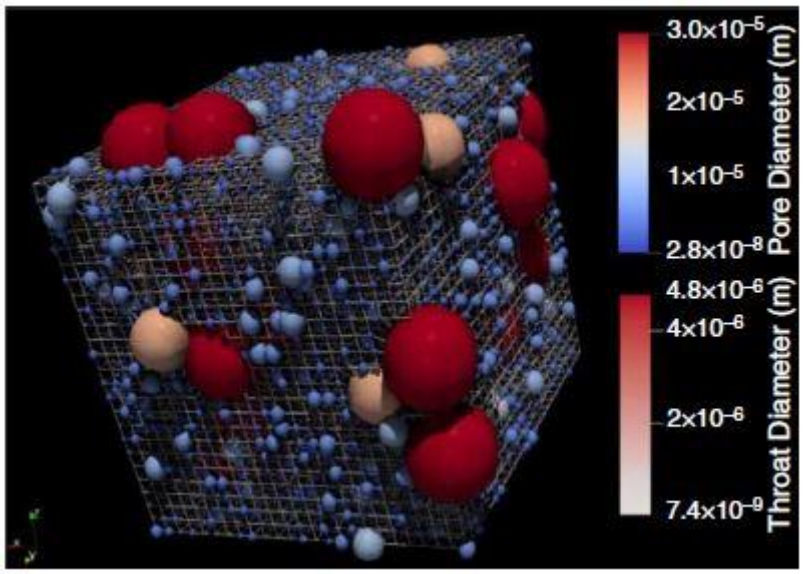

Figure 2-4 Dual-scale PNM constructed with Sadeghnejad and Gostick [22]

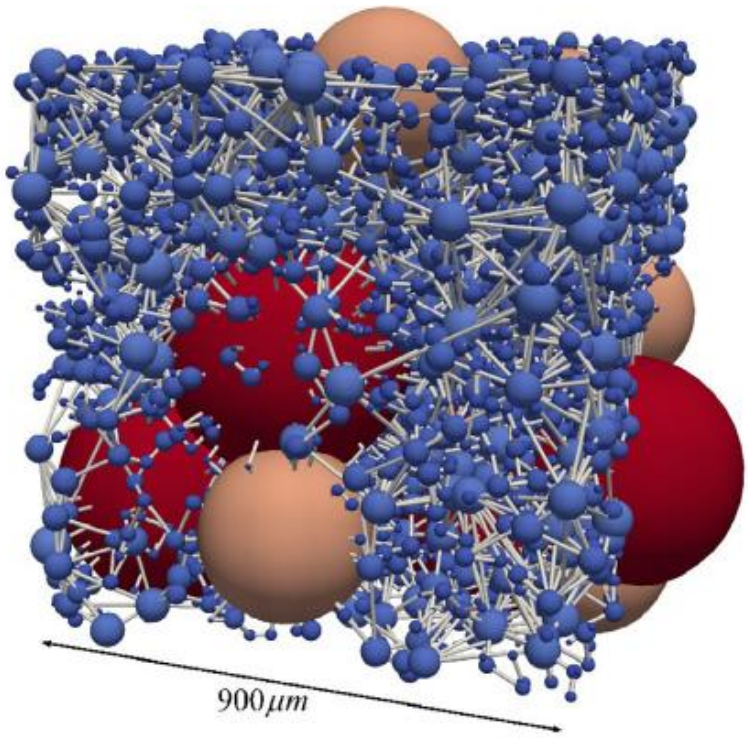

Figure 2-5 Dual-scale PNM constructed with Moslemipour and Sadeghnejad [20]

2.3 Artificial Intelligence

Due to the nonlinearity of neural networks and some learning capabilities in terms of regression analysis, pattern recognition, feature extraction, multi-class classification and generalization, artificial intelligence has become more popular in pore scale modeling. Due to the high usage of artificial intelligence, this approach has been used in PNM and DNS modeling, multi-scale modeling, image reconstruction, image processing and etc. Some of these studies are explained in the following sections.

2.3.1 Predicting properties

Al-Qahtani et al. 2018, extracted the network from 3D images with the watershed algorithm to use them as input data in a convolutional neural network (CNN) to compute the network properties such as porosity, coordination number and average pore sizes. However, in another study, they used binary and grayscale images of rocks as input data of a CNN to calculate porosity, surface area and average pore size and they concluded that the grayscale images from the rock had an error of less than 7%, while the binary image as the input of the neural network had an error of less than 6% [75, 76]. Rabbani et al. 2019 tried a hybrid method to calculate fluid flow properties using a

combination of Lattice-Boltzmann measurement methods, PNM and acceleration through machine learning. First, they found a relationship between the geometry of the throats in the images and their equivalent permeability and calculated the permeability values in different [77]. Sudakov et al. 2019 used machine learning, particularly deep neural networks and reinforcement models, to predict rock sample permeability from digital rock images. The dataset included three-dimensional images from microCT scans and geometric features, which serve as model inputs. Results indicated that 3D convolutional neural networks were more accurate and faster than other models, enhancing the DRP process [78]. Liu et al. (2019) explored using artificial neural networks to predict two phase flow poperties like capillary pressure and relative permeability curves in multiphase flows within porous media. They generated two-phase flow data in capillary tubes with varying cross-sectional shapes and wetting conditions, then used this data to train a neural network. Their goal was to develop a model that could quickly and accurately predict reservoir rock characteristics under different scenarios, outperforming conventional methods [79].

2.3.2 Image reconstruction

One of the most important issues in DRP is the reconstruction of 3D images from 2D images, which include various methods including statistical, process-based and multi-point statistics (MPS) methods. To make a statistical model, it is necessary to calculate the parameters and initial properties. Therefore, the model can be made according to those properties similar to the real 3D model of rock. But after the initial construction of the statistical model, these parameters must be optimized using statistical functions to make the model become more realistic. When a stochastical model of porous media is made then its deviation from the original model is calculated by the statistical function. Then the existing differences will be eliminated and optimize the porous media. Therefore, it can at least compute the porosity of the constructed model correctly. The process-based method is based on a combination of geological information of the area that caused the rock formation, such as sedimentation, compaction, cementation, diagenetic processes, dolomitization and dissolution, as well as tomographic information obtained from CT scan or SEM images. Because this model is based on the fact that the structure of pore often is the result of physical processes. Bryant [80] has developed a process-based method for sedimentary rocks based on modeling rock formation processes such as compaction and cementation by picking spheres of the same size made by Finney [81]. Bakke and Øren [82] presented a reconstruction process-based model that uses rock grain size distribution and other petrographic information obtained from 2D

images. The basis of the proposed method is the construction of sandstone and carbonate rock models based on rock formation processes that reflect the properties of the main rock [83]. The MPS method can use a wide range of properties to construct a large continuous geometry. This method uses geostatistical approaches to construct stochastical patterns. It extracts multiple point patterns from training images using geological information and creates similar behavior in the output reconstructed images [84].

However, artificial intelligence has been used widely in recent studies for image reconstruction. A few kinds of studies have been conducted in this area and the generative adversarial neural network (GAN) networks are used to reconstruct images.

Image reconstruction using GANs typically involves two approaches. In the first, a GAN is trained on a dataset with multiple training samples, allowing the generator to learn the underlying data distribution and produce realistic images based on random or structured latent inputs In the second approach, conditional GANs (cGANs) are used, where the generator receives both a random noise input and specific conditioning data to guide the generation process, often used in supervised reconstruction tasks [85]. Feng et al. 2020 reconstructed 3D structures from a 2D image using a GAN of the BicycleGAN type. One of the remarkable points in their studies in the reconstruction of images using neural networks has been the increase in the speed of reconstruction up to approximately 360 thousand times compared to the conventional methods, which can be very practical in the reconstruction of images with larger sizes [85]. Shams et al. 2019 used a combination of GAN and auto-encoder neural networks to reconstruct 2D and 3D images of multi-scale rocks. The GAN was used to reconstruct the intragranular porosity and the auto-encoder neural network was used to reconstruct the intergranular neural network. The results of this method and its comparison with other methods show that this method is more accurate [55].

2.3.3 Image resolution enhancement

In many cases, the images don't contain good quality due to the trade-off between image resolution and FoV. This is because HR images have a small FoV, which leads to unrealistic results [86]. In fluid flow problems [71, 87] and other numerical methods [88], the image must have a large enough FoV to capture all connections, properties, and rock heterogeneity. Previously, interpolation methods like bilinear, bicubic, and Lanczos were common solutions. However, super-resolution techniques are now preferred. These methods create HR images from one or

multiple LR inputs, providing better detail and accuracy [89]. This method can generate HR image in several realizations. In the past, in addition to the above-mentioned methods, other complex methods based on the reconstruction method were also used to increase the resolution of the images [90, 91]. Machine learning methods have greatly reduced processing time and improved image resolution very well. The relationship between high and low-resolution images is based on a huge amount of training data and is implemented by some methods such as sparse coding (SC) methods [92]. Sparse coding is a great super resolution method that involves several steps to achieve the result. For example, first, the overlapping sections of the input image are cut and pre-processed (calculating the mean difference from normalized). These sections are then sent to an LR dictionary, and the sparse coefficients are sent to a HR dictionary to produce the same sections at high resolution. These reconstructed sections are then collected and the final result is produced [93]. Moreover. the machine learning approach has also been combined with reconstruction techniques and therefore improving the quality of output images. The image resolution of the super resolution convolutional neural networks (SRCNN) is better than previous training and reconstruction methods and also eliminates blurring and noises [94-96]. Moreover, this is very useful in digital rock physics research [97]. Dong et al. 2014 used the CNN method with 3-5 active layers to produce a HR image containing meso and macro scale pores obtained from the bi-cubic method. This method was originally known as the SRCNN method and was later used for deeper and more complex networks [98]. Wang et al. 2019 produced HR images from three different SCRNN models, including SR-Resnet, Enhanced Deep SR (EDSR), and Wide Activation Deep SR (WDSR) [94].

The usual SRCNN methods attempt to get the lowest mean square error (L_2) (Equation 2-1) or the lowest mean absolute error (L_1) (Equation 2-2) in a super-resolution image. This is a powerful method to characterize and improve convergence rates [99]. Images produced with this method have a high signal-to-noise ratio (Equation 2-3) but low perceptual quality. This causes high-frequency texture features to disappear, and only large-scale properties can be examined in this method, which used L_1 and L_2 errors to solve the problem and led to improved results [100, 101]. But to solve this problem completely, they introduced the method of super resolution generative adversarial neural network (SRGAN). This method is obtained by combining the SRCNN method with the discriminator section of the GAN method.

$$L_2 = \frac{1}{N}\sum_{i=1}^{N}\left(I_{1_i}^2 - I_{2_i}^2\right) \tag{2-1}$$

$$L_1 = \frac{1}{N}\sum_{i=1}^{N}\left|I_{1_i}^2 - I_{2_i}^2\right| \tag{2-2}$$

In equation 2-2, N is the total number of pixels in the image. I_1 and I_2 are the pixels of the image, which are to be compared with each other.

$$PSNR = 10\log_{10}\frac{\left[\max(I_1, I_2) - \min(I_1, I_2)\right]^2}{L_2} \tag{2-3}$$

The SRGAN method is used to produce images with a high percentage of similarity to real ones as well as high-texture images [102]. CycleGAN has been introduced as a semi-supervised method that produces HR images using HR and LR unpaired image data [99-103]. Although images produced with this method are very similar to real ones and they have a lower pixel accuracy than the SRCNN method. The micro-CT scan images of rocks have a high amount of noise and high-frequency texture. Therefore, the SRCNN method has a better ability to remove noise and maintain image resolution [104]. Therefore, most studies use the SRCNN method to produce HR images from micro-CT scan images. But a few studies that have used the SRGAN method to produce HR images are described in the following. Johnson et al. 2020 used a GAN, which is named conditional generative adversarial neural network (C-GAN) to produce HR images. The generator of this network is composed of a SRCNN network (U-Net) [105]. Wang et al. 2019 used a SRGAN network to produce HR 2D and 3D images from LR ones. The generator of SRGAN is composed of a SRCNN network that was optimized for both EDSR and SR-Resnet. Therefore, the overall structure of the EDSR network was preserved, but the Rectified Linear Unit (ReLU) Layers were replaced with the Parametric Rectified Linear Unit (PReLU) layers of the SR-Resnet. This operation was considered as a batch normalization in the SRCNN network and caused a few reductions in processing time [96].

2.3.4 Image segmentation

One of the capabilities of artificial intelligence is multi-mineral segmentation. Studies in this field have been performed using SEM or other HR images. Because in these images, minerals can be distinguished from each other better due to higher resolution and less noise [106-108]. Another reason for using these images is the ability to combine them with the Energy Dispersive Spectroscopy (EDS), which will help in distinguishing minerals [106]. These methods cannot detect minerals in the micro-CT images [109, 110]. Another major feature of neural networks is image segmentation, which minimizes user bias in selecting the threshold value. Hebert et al. 2020 used three deep learning networks to characterize rock types and calculate porosity in micro-CT images. These networks are Inception-V3, named Rockclass, which is used to characterize the type of rock from images. The next network is an optimized regression CNN called RegPhi, which is used to calculate the total porosity of an image without segmentation. The last network used is an autoencoder neural network that calculates total porosity with automatic image segmentation. It was found that the results have a small error in calculating the porosity and image segmentation [111]. Wang et al. 2020 used four CNN models to segment 2D and 3D images of rock. Moreover, they achieved a very high level of accuracy by comparing the results with each other and also with the results of existing binary images. The networks used in this study are: SegNet, UNet, ResNet and U-ResNet. After image segmentation and comparison with existing results, it was concluded that UNet and U-ResNet models proposed the best segmentation compared to other methods [106]. Niu et al. 2020 used CNN to segment micro-CT and SEM images of rocks. Because, unlike conventional methods, these networks select the segmentation threshold value automatically. After image segmentation, they calculated the porosity, permeability and pore size distribution on the extracted network from the images. The results show that the difference in the answers obtained by the neural network is much smaller than the conventional methods that used the manual selection of the threshold value [107].

2.4 Octree structure

An Octree is a tree structure data that each internal node has exactly eight children. Octrees are often used to represent a 3D space by recursively dividing that space into eight equal parts (Octants) (Figure 2-6). The Octrees are equivalent to Quad-trees but in 3D space [112]. 3D space modeling is very important in computers that take up a lot of storage space in the system. Octree is a method that can display 3D with less occupied memory space. As mentioned, in order to model

and simulate, it is necessary that the desired structure and image have a large enough field of view to be able to refer to its results. Today, powerful systems and machines have been created for the purpose of modeling on the second largest, which has enabled modeling in the field of view and large dimensions to some extent. But these systems still have problems modeling large models and images because these networks contain hundreds of thousands or even millions of cells [113]. Therefore, improving the runtime performance of simulators is very important. For this reason, the AMR method of adaptive mesh modification and the use of octal tree structures is a wise solution to save, dynamically, both memory resources and computation time, while the given numerical accuracy of the obtained results guarantees This method is well developed in many areas of computational physics (such as fluid dynamics and solid mechanics), but is not widely used for practical reservoir simulation [114].

Recent research has introduced various AMR procedures to capture the local characteristics of transport processes. Bahrainian and Dezfuli 2014 developed a novel unstructured grid generation algorithm that accounts for geological features and well locations in grid resolution. This approach involves defining and constructing the initial grid based on the geological model, adapting the grid geometry to geological features, and controlling grid resolution [115]. Trangenstein 2002 combined HR discretization methods with dynamically adaptive mesh refinement in a two-component, single-phase model for miscible flooding [116]. Pau et al. 2012 proposed an AMR algorithm for compressible two-phase flow in porous media. Their method, implemented within a block-structured AMR framework, allows the grid to adapt dynamically to flow features and enables efficient parallelization. They obtained coarse-scale permeability by averaging fine-scale permeability values [117]. Similar techniques have been applied to compositional simulation [118], thermal problems [119], enhanced oil recovery processes [120], and Discrete Fracture Networks [121], among other applications.

Octree has also many applications, including 3D computer graphics, spatial indexing, unstructured grid, and so on. But this method can be very efficient in the field of pore scale modeling, which has not received much attention to date. Most modeling in this field has high computational costs and requires a large amount of memory space, which makes large FoV modeling virtually impossible. Therefore, the Octree method can be a good idea for multi-scale modeling of

heterogeneous rocks with large FoV, which can model a wide range of pores in these rocks and reduce the computational cost compared to the regular image grid.

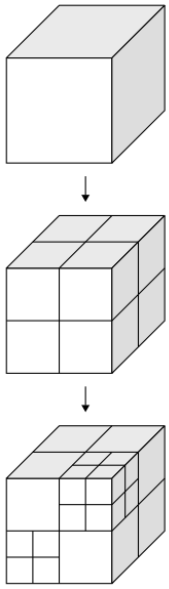

Figure 2-6 Schematic of the Octree method [122]

The methods of Octree and Quad-tree have many applications in various fields to date. Jayaraman et al. 2018 created CNN based on the Quad-tree method (Figure 2-7). This method has transformed the image into a Quad-tree form. Therefore, the non-zero value sections were divided into the smallest part and then the convolution operation was performed on these parts. They called this network the Quadtree Convolution Neural Network (QCNN) and implemented it on various images and achieved good results [123].

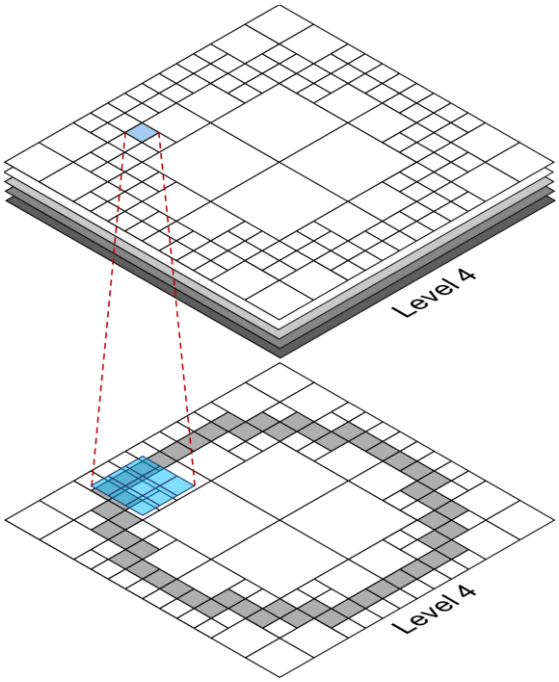

Figure 2-7 The basis of QCNN [123]

Moreover, Wang et al. 2017 presented an Octree Convolution Neural Network (OCNN). They tested this network on various 3D images and compared the result with that of conventional CNNs. This network displayed the input image as an Octree image and gave the average normal vectors, which were stored in the smallest box as input to CNN. All calculations are performed on the GPU and the results are stored as an Octree structure [124]. The Octree is also used for 3D printing, as shown in Figure 2-8. This method voxelized the output files of AutoCAD software, which are vector images. The output image, which is in the form of an Octree image, will then be directly printed in 3D. This method is much faster than the conventional methods and is associated with less occupied memory space [125, 126].

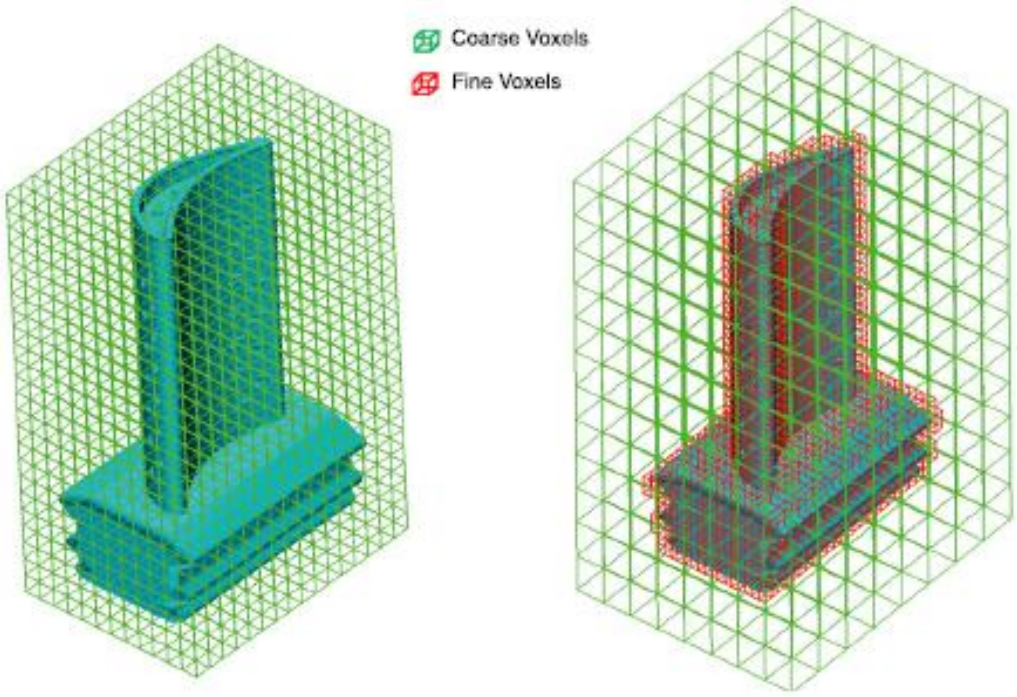

Figure 2-8 Voxelized AutoCAD software output as an Octree image [125]

Chapter 3

Methodology

Methodology and equipment

3.1 Synopsis

In this chapter, rock samples, equipment, scanned images and image processing methods are explained, and then the multi-scale image and pore network reconstruction methodologies with different assmptions and the calculation of different properties using DNS and PNM will be explained.

3.2 Rock sample

In this research, in order to reconstruct the multi-scale image and pore network, three heterogeneous rock samples have been used, which include Berea sandstone (BS), Edward Brown carbonate rock (EBC) and Indiana limestone (ILS). These rocks have been imaged in different resolutions with different imaging devices to be able to examine multi-scale rocks for multi-scale modeling. The Berea sandstone, a Mississippian terrestrial rock, is a typical oil and gas source rock [127]. It consists of both heterogeneous and homogeneous structures and is commonly used for benchmarking [128-131]. The Edward Brown carbonate is sourced from a quarry located in Texas, USA, which is part of the Edwards limestone series within the Edwards Plateau. This formation includes the Edwards White and Yellow Carbonates and exhibits reservoir rock properties. These carbonates were formed mainly in shallow marine waters and tidal settings during the early Cretaceous period [132, 133]. The Indiana limestone or formerly called Salem limestone is part of the Salem formation, which is associated with the middle Mississippian. The ILS is located in the U.S. states Illinois, Indiana, Kentucky, and Missouri and is primarily quarried near Bedford (Indiana). Ji et al. (2012) have classified this limestone as a calcite-cemented grainstone with fossil fragments. The main fossils are bryozoans, echinoderms, and endothyra (Carr et al., 1966). Besides fossils, other allochems are ooids and peloids, which are all frequently coated with concentric layers of calcite (Ji et al., 2012). Figure 3-1 shows a gray-scale image of three rocks. Moreover, the characteristics of these three rocks are given in Table 3-1.

Table 3-1 The characteristics of all three rock samples

Rock	Diameter (cm)	Length (cm)

BS	**0.35**	**1**
EBC	**3.5**	**5**
ILS	**3.5**	**5**

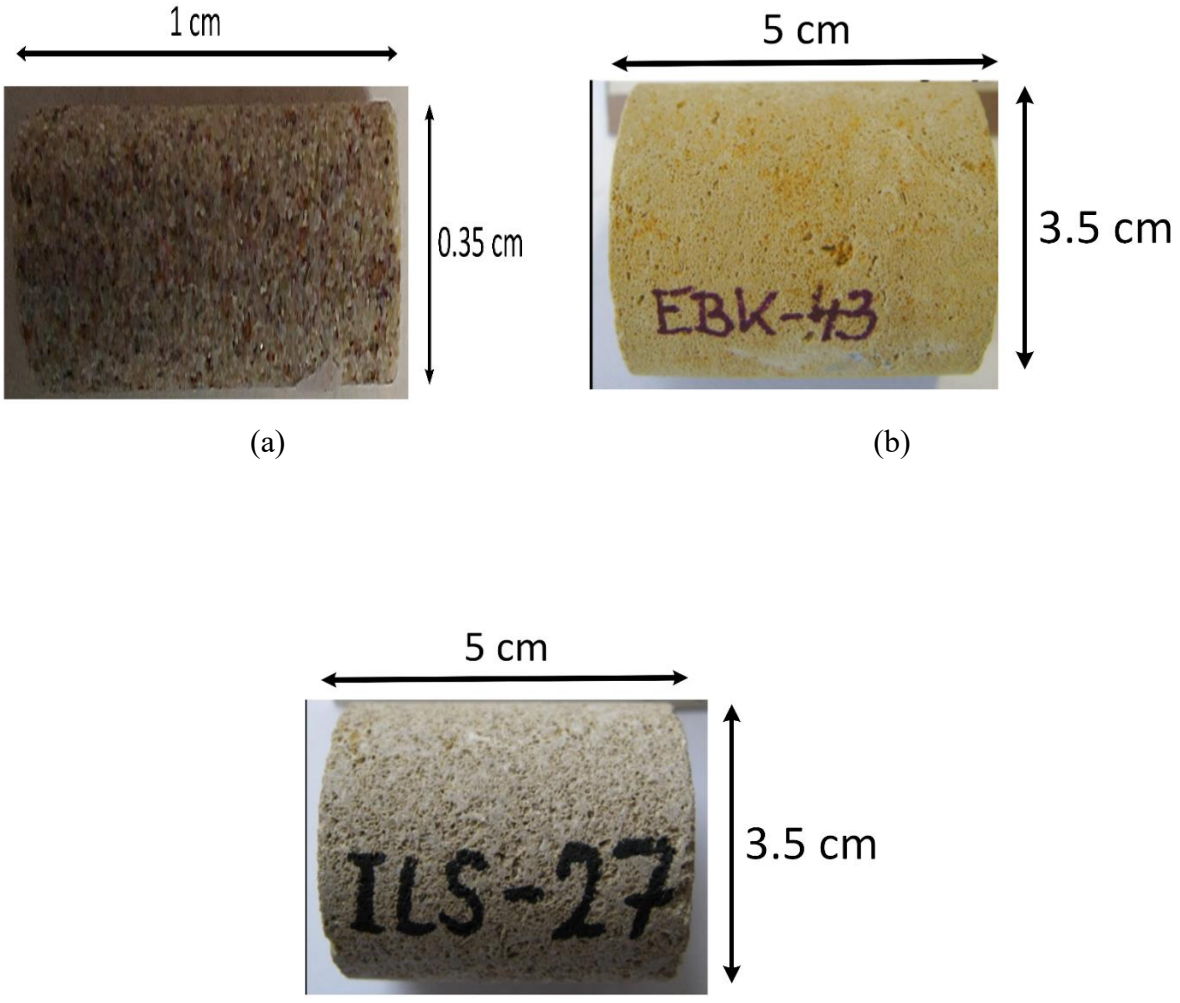

Figure 3-1 Plugs of (a) BS (b) EBC and (c) ILS rock samples used for this study

3.3 Imaging

3.3.1 Imaging devices

In our research, we scanned each rock in two different resolutions: low-resolution (LR) and high-resolution (HR) images. Our goal is to integrate these images for each rock to reconstruct multi-scale images and multi-scale pore networks. We first scanned both the LR and HR images of the EBC rock sample and the LR image of the BS rock sample, using a laboratory X-ray microtomography (XCT) scanner [134]. The reconstruction, beam hardening, and ring artefact correction were performed with the X-AID software (MITOS GmbH, Germany).

Additionally, an HR image of the BS rock sample was scanned at the beamline HEREON IBL P05 of the X-ray synchrotron light source PETRA III at DESY Hamburg. An advanced reconstruction script implemented in the MATLAB® 2022 software code was applied to carry out the reconstruction and ring artefact correction of these SXCT images [135]. The following parameters were used at the beamline P05: monochromatic beam energy of 30 keV, an XIMEA camera with 5,001 projections, and a binning factor of 1. Moreover, for both LR and HR images of ILS rock sample, micro-CT scanning was performed using a high-resolution micro-computed tomography system (ZEISS Xradia 620 Versa X-ray microscope). These images were captured from the same location of the sample. The scanning was performed at an energy setting of 160 kV for 10 µm scan and 140 kV for another scan, which were optimized for the specific density and composition of the sample. The reconstruction of the 3D dataset was carried out using a filtered back-projection algorithm (Scout and Scan^{TM}, Zeiss company, version 16.1), which facilitated accurate volumetric reconstructions with minimal noise and artifacts. This approach enabled detailed visualization and analysis of the internal structure of the sample at a high spatial resolution. The BS rock sample was scanned at 1.28 and 2.4 µm resolutions. The size of LR image for this rock was 1,944 × 1,944 × 1,536 voxels and the size of HR image was 4,922 × 4,922 × 2,401 voxels. Moreover, the EBC rock sample was scanned at 1.49 and 10.88 µm resolutions. The size of LR image for this rock was 3,024 × 3,064 × 1,932 voxels and the size of HR image was 1,992 × 2,036 × 2,002 voxels. Finallty, the ILS rock sample was scanned at 3.9 and 10 µm resolutions. The size of LR image was 1,013 × 1,013 × 1,024 voxels and the size of HR image was 992 × 998 × 1,014 voxels. The LR and HR images are shown in figure 3-2 and the LR and HR images characteristics are summarized in Table 3-2 and 3-3.

Table 3-2 LR images characteristics of all rock samples

Rock	Imaging device	Resolution (µm)	Size (voxels)
BS	Micro-CT	2.4	1,944×1,944×1,536
EBC	Micro-CT	10.88	3,024×3,064×1,932
ILS	Micro-CT	10	1,013×1,013×1,024

Table 3-3 HR image characteristics of all rock samples

Rock	Imaging device	Resolution (µm)	Size (voxels)
BS	Micro-CT	1.28	4,922×4,922×2,401
EBC	Micro-CT	1.49	1,992×2,036×2,002
ILS	Micro-CT	3.9	992×998×1,014

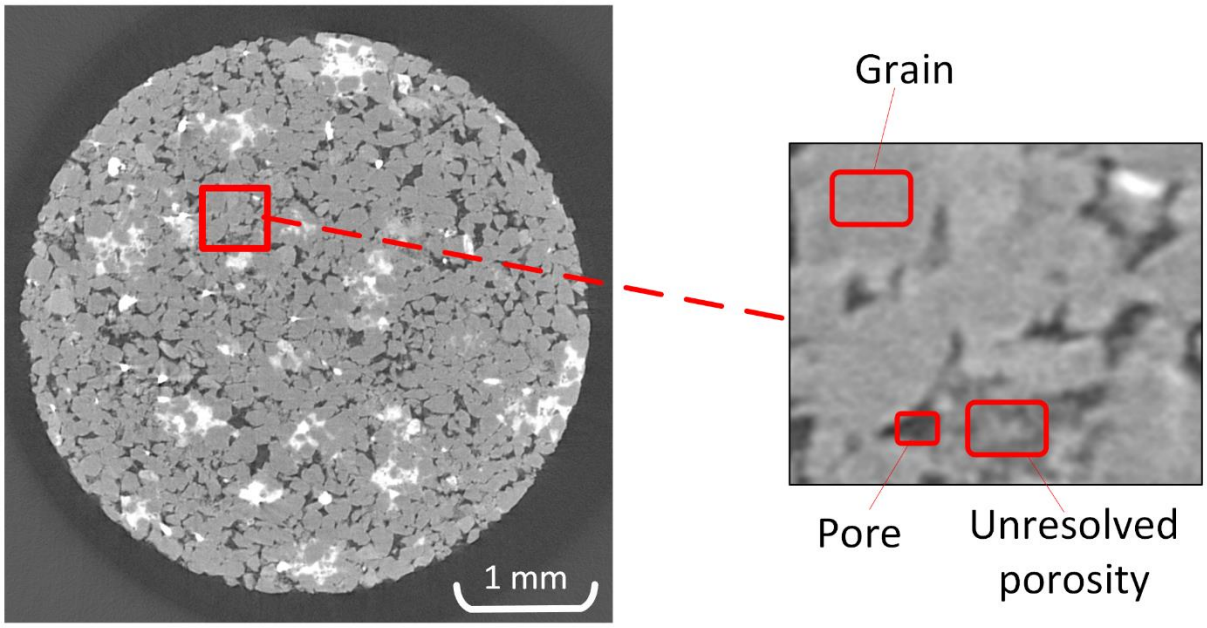

(a)

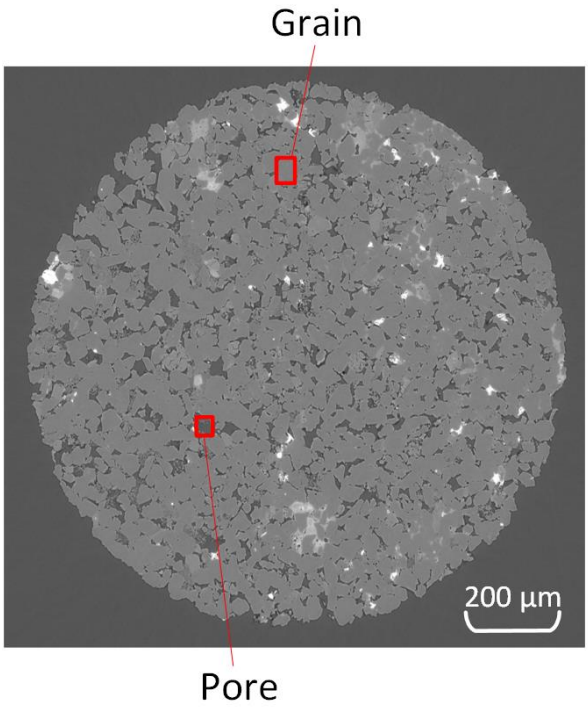

(b)

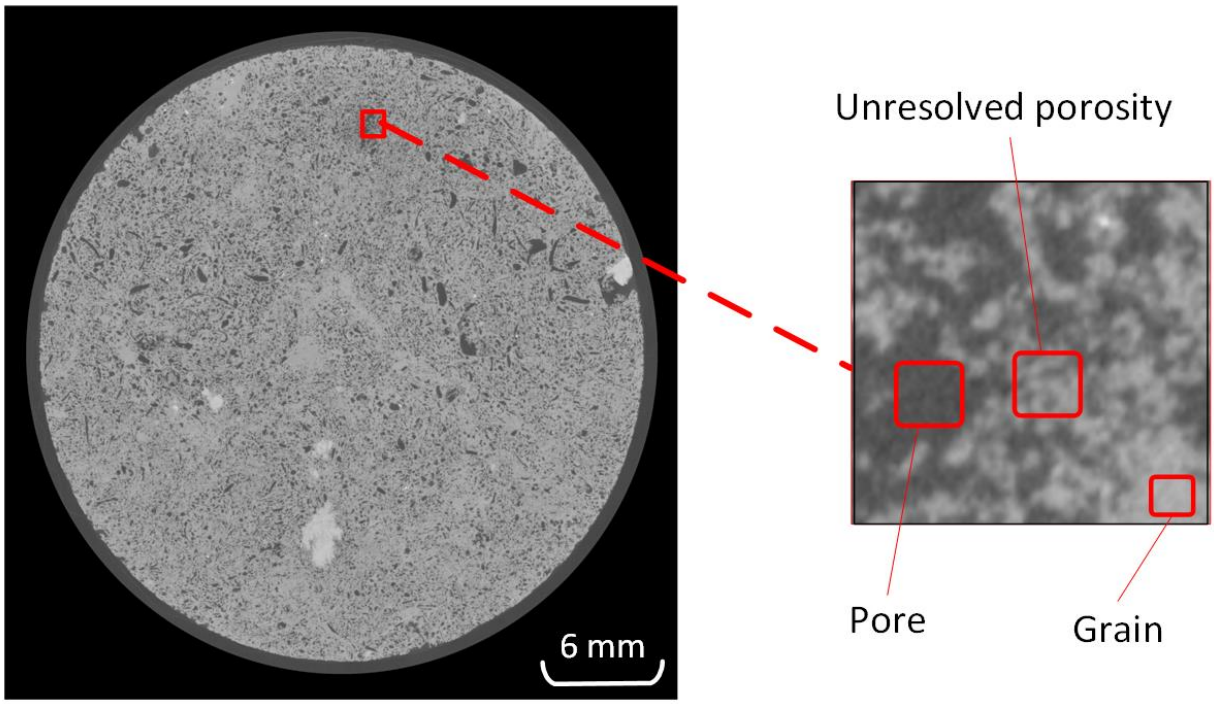

(c)

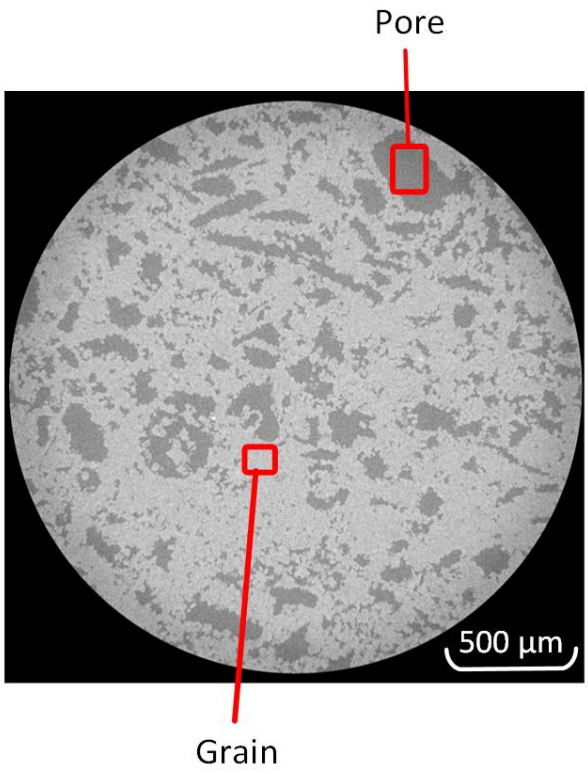

(d)

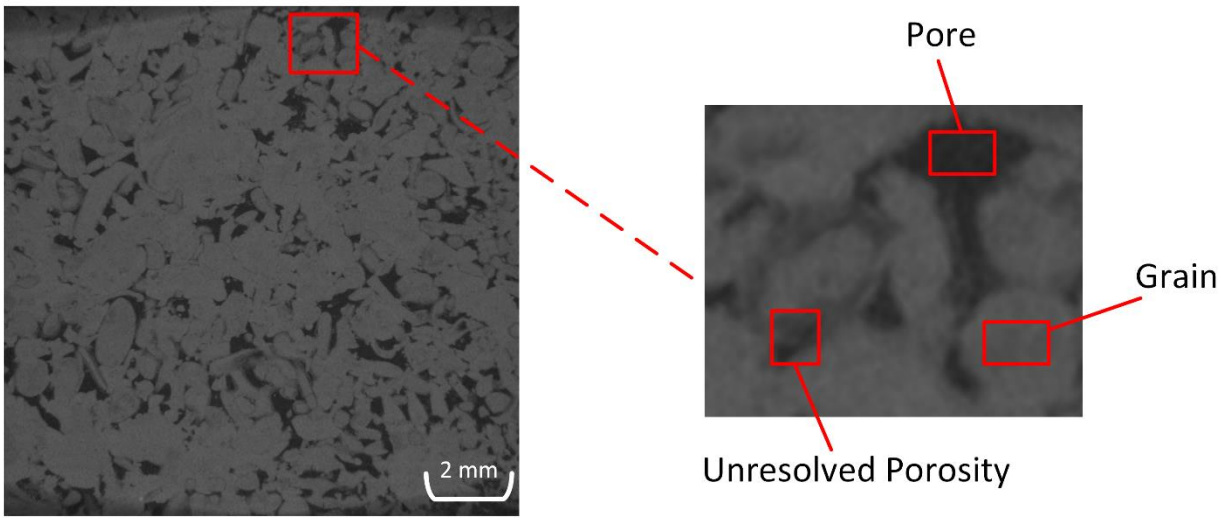

(e)

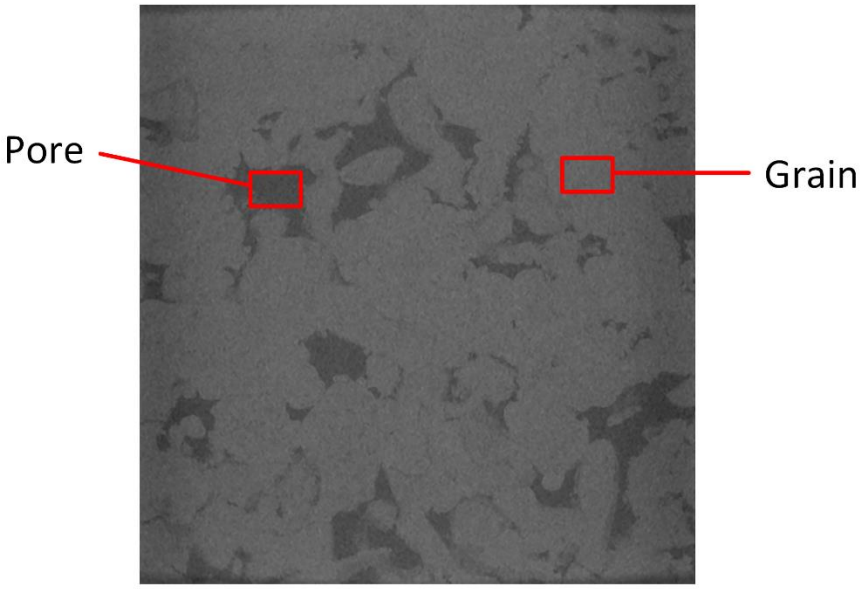

(f)

Figure 3-2 A 2D scan from 3D grayscale (a) LR and (b) HR micro-CT scans of the BS rock sample, along with a 2D (c) LR and (d) HR micro-CT scans of the EBC rock sample and (e) LR and (f) HR micro-CT scans of the ILS rock sample

3.4 Image Processing

3.4.1 Image cropping

For multi-scale modeling and reconstruction, we need suitable sizes of images for all three rocks that are neither too small nor too large. For this purpose, first, we separate a crop from each image,

both LR and HR, in order to reconstruct the images and the PNM on them. Therefore, for the BS rock sample, the sizes of the cropped scans were 1,000 × 1,000 × 1,000 voxels in the HR image and 400 × 400 × 400 voxels in the LR image. In addition, for the EBC rock sample, the respective sizes of the cropped scans were 1,000 × 1,000 × 1,000 voxels in the HR image and 187 × 187 × 187 voxels in the LR image. Finally, for the ILS rock sample, the respective sizes of the cropped scans were 668 × 961 × 700 voxels in the HR image and 400 × 400 × 400 voxels in the HR image. Figure 3-3 shows both LR and HR images of the cropped scans of the BS, EBC and ILS rock samples, respectively.

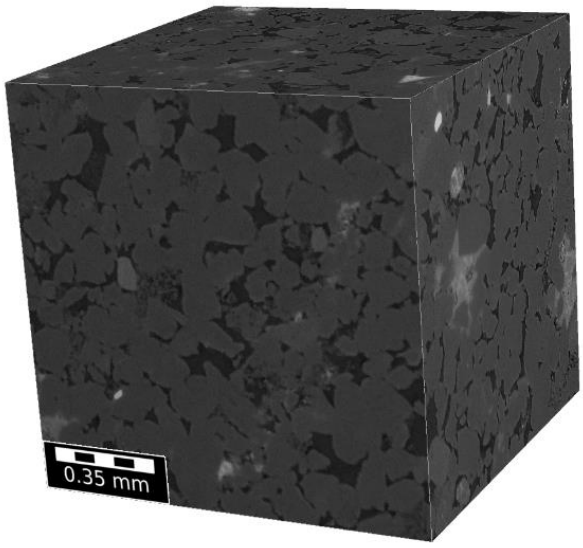

(a)

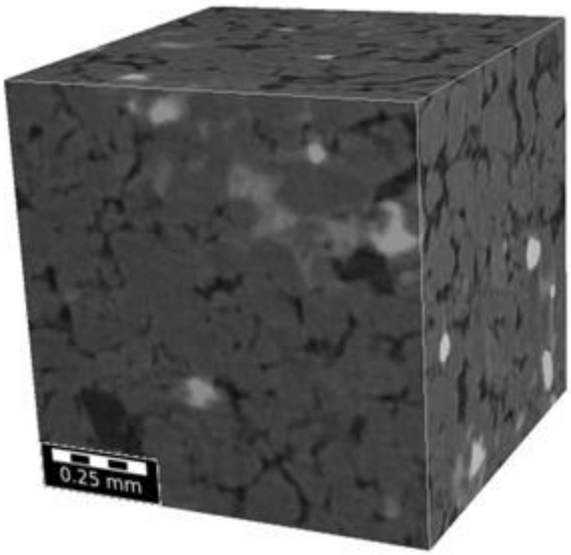

(b)

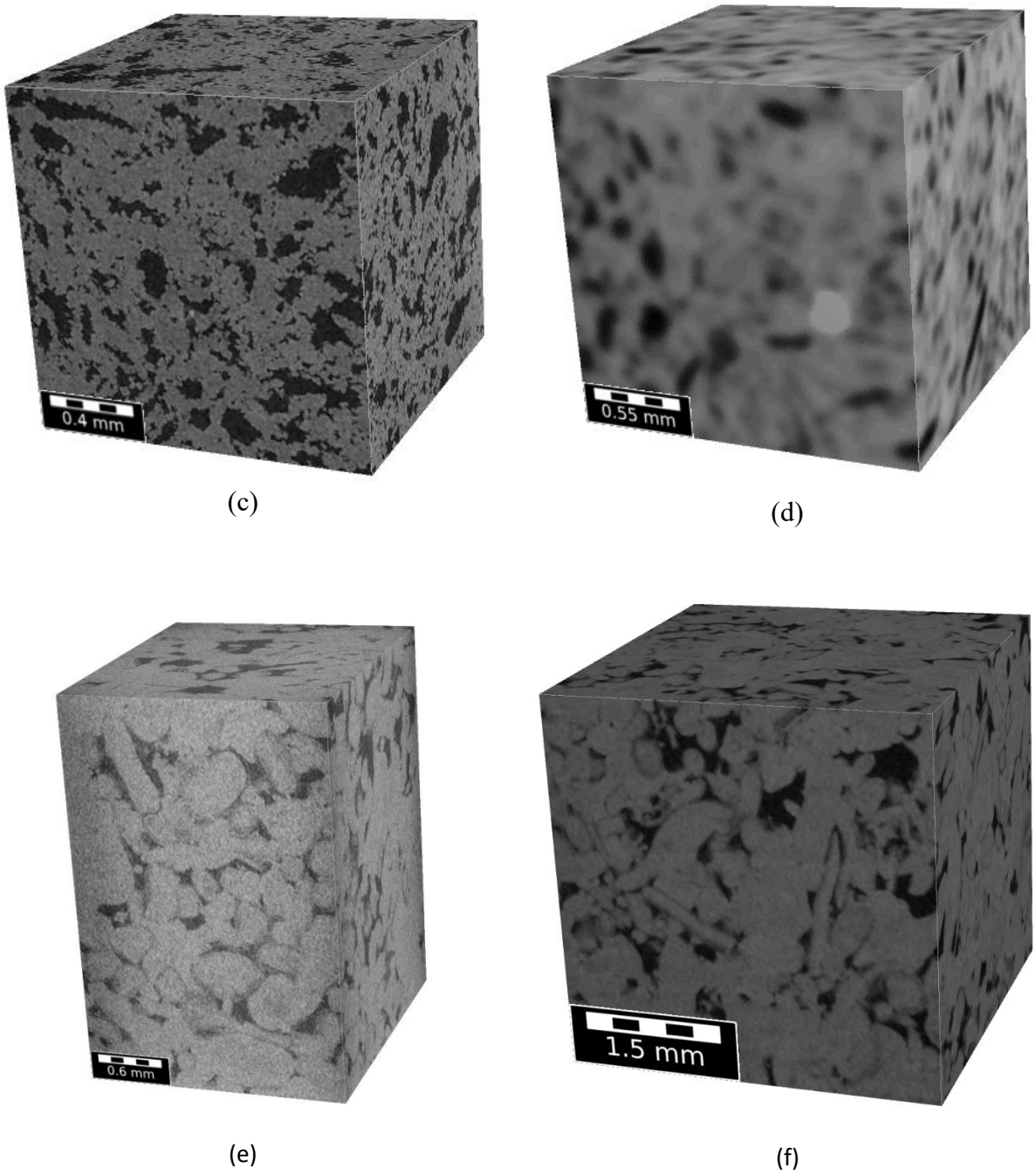

Figure 3-3 (a) HR and (b) LR micro-CT scans of the BS rock sample, along with (c) HR and (d) LR micro-CT scans of the EBC rock sample and (e) HR and (f) LR micro-CT scans of the ILS rock sample

3.4.2 De-noising

After cropping, all scans were de-noised using the non-local means method using the ImageJ version 1.52 software package [136]. In order to process the images at different resolutions, first

the noise in the images is removed by de-noising methods using GeoDict 2023 software. In order to select the proper de-noising method in micro-CT scan images, three methods are applied on the image, which are: Median filter, non-local means filter and Gaussian filter. Then we chose the method that had the best performance in removing noises for images and applied the desired filter on images of different rocks to remove noise and prepare the image for resampling and segmentation. Below is a brief description of each of these de-noisning filters.

3.4.2.1 Median filter

Median filter is a non-linear noise removal method used to smooth the image. This filter is useful for removing impulses caused by signals. The median filter collects $N = 2k + 1$ samples of the signal and calculates the averaging operation with these samples using equation 3-1.

$$y(n) = med\left[x(n-k), x(n-k+1,\ldots, x(n),\ldots, x(n+k-1), x(n+k)\right] \qquad (3\text{-}1)$$

In the equation 3-1, $y(n)$ is the output value of the pixel and $x(n)$ is the input of the signal [137].

3.4.2.2 Non-local means filter

By entring a pixel image $v = \{v(i) \mid i \epsilon I\}$ as input, the calculated value of $NL[v](i)$ for a pixel is considered as the weighted average value of all pixels in the image.

$$NL[v](i) = \sum_{j \in I} w(i,j)v(j) \qquad (3\text{-}2)$$

where the family of weights $\{w(i.j)\}_j$ depends on the similarity of pixels i and j [138].

3.4.2.3 Gaussian filter

Gaussian blur is one of the blurring filters that uses a Gaussian function to transform each pixel (this function is also known as normal distribution in statistics). The normal function is introduced as follows.

$$G(x) = \frac{1}{\sqrt{2\pi\sigma^2}} e^{-\frac{x^2}{2\sigma^2}} \tag{3-3}$$

In the equation 3-3, x is equal to the distance of the pixel to the origin in the horizontal direction and σ represents the standard deviation of the dispersion. For three-dimensional images, the Gaussian function is used in three dimensions, and its formula is as follows.

$$G(x) = \frac{1}{\sqrt{2\pi\sigma^2}} e^{-\frac{x^2+y^2+z^2}{2\sigma^2}} \tag{3-4}$$

In the equation 3-4, y represents the distance from the pixel to the origin in the vertical direction.

3.4.3 Image resampling

In the next step, due to the fact that we need to fuse HR and LR images to reconstruct a multi-scale image, at first, we need to change the pixel size of the images according to the type of method used. In the following, it is explained that each method uses which image for the multi-scale image reconstruction.

Therefore, first, the pixel size of the LR scans was resized to have a ratio of 2^n of the pixel size of the HR scans. In other words, the pixel size of the HR scans should become 2^n times (n is an integer number) finer than that of the LR scan. This procedure is important for merging the LR and HR scans with the least changes in the digital rock properties. This process is called resampling.

For this purpose, the LR scan pixel size of BS, EBC and ILS were resampled from 2.4, 10.88 and 10 µm to 2.56, 11.92, 7.8 µm, respectively. The pixel size of HR scans becomes 2 ($2.56\mu m = 2\times 1.28\mu m$), 8 ($11.92\mu m = 2^3 \times 1.49\mu m$) and 2 ($7.8\mu m = 2\times 3.9\mu m$) times finer than the pixel size of the LR scans, respectively. Therefore, the LR scan of the BS rock sample was converted from the size of 400 × 400 × 400 voxels to the size of 375 × 375 × 375 voxels. Moreover, the LR scan of the EBC rock sample was converted from the size of 187 × 187 × 187 voxels to the size of 170 × 170 × 170 voxels. Finally, the LR scan of the ILS rock sample was converted from the size of 400 × 400 × 400 voxels to the size of 513 × 513 × 513 voxels.

To fuse the scans, the pixel size of the LR scan had to be resampled 2^n smaller. This resampling process was applied by the nearest neighbour interpolation method. This method has a minimal effect on scan properties since each voxel is divided into eight equal sub grids at each step, where n represents the number of division stages. Consequently, this approach made the pixel sizes of the LR and HR scans equal. The LR scan of the BS rock sample was converted from the size of 375 × 375 × 375 voxels and a resolution of 2.56 µm to the size of 750 × 750 × 750 voxels and a resolution of 1.28 µm ($2.56 = 1.28\times 2^1 \Rightarrow n = 1$). Moreover, the LR scan of the EBC rock sample was converted from the size of 170 × 170 × 170 voxels and a resolution of 11.92 µm to the size of 1,360 × 1,360 × 1,360 voxels and a resolution of 1.49 µm ($11.92 = 1.49\times 2^3 \Rightarrow n = 3$). Finally, the LR scan of the ILS rock sample was converted from the size of 513 × 513 × 513 voxels and a resolution of 7.8 µm to the size of 1,026 × 1,026 × 1,026 voxels and a resolution of 3.9 µm ($7.8 = 3.9\times 2^1 \Rightarrow n = 1$).

We considered three methods of Bicubic, Bilinear and Lanczos for resampling and applied them to the images. Then we chose the method that has the least impact on the image properties in each step. Because resampling should not change the characteristics of the images, otherwise it will lower the accuracy of the reconstructed images. Therefore, we calculated the porosity and permeability of the images before and after resampling and chose the method that has the least impact on the properties. We used the Avizo version 2019 software package to apply these methods on the images, and the explanation of each of the resampling methods is given below.

3.4.3.1 Nearest neighbour

Nearest neighbor interpolation is a very basic resampling technique for estimating the intensity values of unknown points in a dataset. It is straightforward and less computationally intensive;

therefore, it is well-suited for applications in which processing time is critical or computational resources are limited [139, 140]. With respect to 3D images, nearest neighbor interpolation may take a value from its nearest neighbor to estimate the value of a voxel. The principle of this Nearest Neighbor method is to give the intensity value of the nearest voxel to the target voxel. Other interpolation methods compute a weighted average of surrounding voxels, while nearest neighbor interpolation just picks up the value from the closest voxel, making it very fast but less smooth. In mathematical terms, for a target point (x,y,z), the interpolated value $I(x, y, z)$ is given by:

$$I(x, y, z) = I(x_{nearest}, y_{nearest}, z_{nearest}) \tag{3-5}$$

where $I(x_{nearest}, y_{nearest}, z_{nearest})$ is the coordinate of the nearest voxel to the target point.

Though simple, Nearest Neighbor interpolation serves several useful purposes. Real-Time Rendering: It is fast, so it becomes very suitable for applications where the required speed in rendering is high, like in interactive visualizations and gaming. Initial Data Exploration: Volumetric data gives an excellent, fast, and easy preview, removing the need to use more computationally intensive methods. Binary or Categorical Data: This happens to be the case with binary or categorical data, where intermediate values are meaningless, as in some cases in segmented medical images where each voxel is categorized into various distinct categories.

3.4.3.2 Lanczos

It is a rather sophisticated resampling method that assures better image quality with fewer artifacts and sharp details. Lanczos interpolation uses an ideal sinc function with a windowing function that limits the infinity of the sinc function for band-limited signals [139, 140]. Thus, its extension to 3D images makes this method a very powerful tool in volumetric data processing and consequently in applications related to medical imaging, computer graphics, and scientific visualization. Lanczos interpolation is a windowed form of theoretically optimal sinc interpolation for reconstructing bandlimited signals. The sinc function is defined as:

$$\sin c(x) = \frac{\sin(\pi x)}{\pi x} \tag{3-6}$$

However, sinc functions extend to infinity, which is quite impractical for real-world computations. Lanczos interpolation does so by multiplying the sinc function with a Lanczos window function which itself is a sinc function, truncated to a finite number of samples. The Lanczos kernel L(x) or a given parameter α (the window size) is defined using equation 3-7:

$$L(x) = \sin c(x).\sin c\left(\frac{\pi}{\alpha}\right) \tag{3-7}$$

where α is typically an integer. For a point (x,y,z) in 3D inside a voxel grid, an interpolation function will weigh the contributions from surrounding voxels based on the 3D Lanczos kernel. The interpolation itself is done by summing up the products of voxel values and Lanczos kernel values.

Lanczos interpolation finds great utility in medical imaging, wherein clarity and accuracy of volumetric data are paramount. It is used in reconstructing high-resolution 3D images from lower-resolution scans, thus improving diagnosis. In computer graphics, Lanczos interpolation can be very helpful in enhancing the visual quality of 3D models and textures for more realistic renderings. Finally, it finds a place within scientific visualization to render accurate and clear depictions of complex datasets.

3.4.3.3 Bi-linear

Bilinear interpolation is one of the easiest resampling methods interpolating data points in a grid. While this concept is quite elementary, it can be easily used to generalize into 3D images. It becomes very useful in applications that need computational simplicity and efficiency, such as in real-time rendering, medical imaging, and volume visualization. In 2D bilinear interpolation, the intensity value for a target pixel is inferred from the intensity values of its four nearest neighboring pixels. The process involves two linear interpolations in one direction, followed by another linear interpolation in an orthogonal direction [139, 140]. Applied to 3D images, it will then approximate the intensity value at a point on a 3D grid from its eight nearest neighboring voxels. This bi-linear interpolation function of a point, (x,y,z) can be expressed as a weighted average of the intensities

of the eight voxels surrounding it. The weights are decided based on the relative distances of the point from the neighbor voxels. Therefore, the intensity value $I(x,y,z)$ at the point (x,y,z) is calculated using equation 3-8:

$$I(x,y,z) = \sum_{i,j,k=0}^{1} w_{i,j,k} I(x_i, y_j, z_k) \tag{3-8}$$

where $I(x_i, y_j, z_k)$ are the intensity values at the eight neighboring voxels, and $w_{i,j,k}$ are the weights calculated based on the relative distances.

Bilinear interpolation is applied in medical imaging techniques such as MRI and CT to reconstruct intermediate slices so that volumetric data can be visualized better. This will provide fast, reasonably accurate ways of estimating voxel intensities, which helps in diagnosis and treatment planning. In computer graphics, bilinear interpolation is applied not only in texture mapping but also in volume rendering, which ensures that 3D models or scenes are continuous and look realistic when zoomed in on or viewed from different angles.

3.4.3.4 Bi-cubic

Among the advanced resampling techniques that provide better results than some of the simpler methods, such as nearest neighbor and bilinear interpolation, is bicubic interpolation. In this technique, the intensities for unknown points of 3D images are estimated by using the values of surrounding points. This method has become very popular since it generates smoother and more pleasing images. These qualities are very important in medical imaging, computer graphics, and scientific visualization. In 2D, bicubic interpolation fits a smooth curve through the 16 neighboring points (a 4×4 grid) around the target pixel. The interpolation function is cubic polynomial in each dimension; therefore, image continuity and smoothness are guaranteed [139, 140]. In 3D, interpolation uses a 4×4×4 cube of neighboring points, involving 64 points to estimate the intensity at a given voxel. Therefore, the new pixel of the resampled image $p(x,y,z)$ is calculated by:

$$p(x,y,z) = \sum_{i,j,k=0}^{3} \alpha_{i,j,k} x^i y^j z^k \tag{3-9}$$

where $p(x, y, z)$ is the interpolated value at the point (x, y, z). The 64 coefficients $a_{i,j,k}$ should be determined first for solving the equation 3-9 [141, 142].

In medical imaging techniques such as MRI and CT scanning, bicubic interpolation reconstructs high-resolution volumetric images from lower-resolution data. This refines the diagnostic capability of these techniques. In the field of computer graphics, it will generate smooth 3D models from sampled data; hence, it will increase the realism of rendered scenes. In scientific visualization, this also reaps the same benefits by producing clearer and more accurate renderings of complex 3D datasets.

3.4.4 Image segmentation

In the last stage of image processing, it is necessary to convert the images into binary format, which in this case are divided into two and three phases for HR and LR images, respectively. The segmentation of μCT scan images is a crucial step in the digital rock physics workflow [143], which involves partitioning a scanned image into multiple segments or regions based on image characteristics. A two-phase segmentation was applied to the HR scans by segmenting them into pore and solid grain phases, while a three-phase segmentation was implemented for LR images. For the latter, the unresolved porosity with intermediate gray-value voxels was chosen as the third phase in LR images.

Unresolved porosity refers to phases that contain pores, which are too small to be resolved/captured by the imaging technique chosen. The pore geometry details in these phases are not clear, and higher resolution images are needed to capture their details. These unresolved porosity sections can be clarified by applying specific segmentation methods to the gray values of image voxels. Therefore, a three-phase segmentation was applied to the LR scans by segmenting them into voxels with low, intermediate, and high gray values.

The segmentation of the HR and LR scans was performed using a supervised artificial intelligence method as implemented in the GeoDict 2023 software package (Math2Market GmbH, Kaiserslautern, Germany). The goal was to segment the complete gray value image based on user-defined labels. The architecture schematic of the segmentation network is depicted in Figure 3-4. This technique involves manually labeling the original image based on the user's judgment of segmented phases. Subsequently, a machine learning model called UNet is trained to accurately

segment the input original and labeled images (i.e., training data) [144]. This network consists of a constricting branch (encoder) on the left and an expanding branch (decoder) on the right. Moreover, the number of layers in each branch defines the depth of the UNet model. We selected a UNet with two convolutional layers, which learns from each slice of image. The window size for training was 52 × 52 × 52 voxels with a stride of 6 in each direction. Moreover, the number of epochs was 10 and the number of features in the first and second layers was 16 and 32, respectively. The network output consists of two-phase segmented images for the HR images and three-phase segmented images for the LR images. Correctly specifying labels at the boundary voxels between phases is crucial. Accurate segmentation at these boundaries significantly impacts the results of the multi-scale image reconstruction.

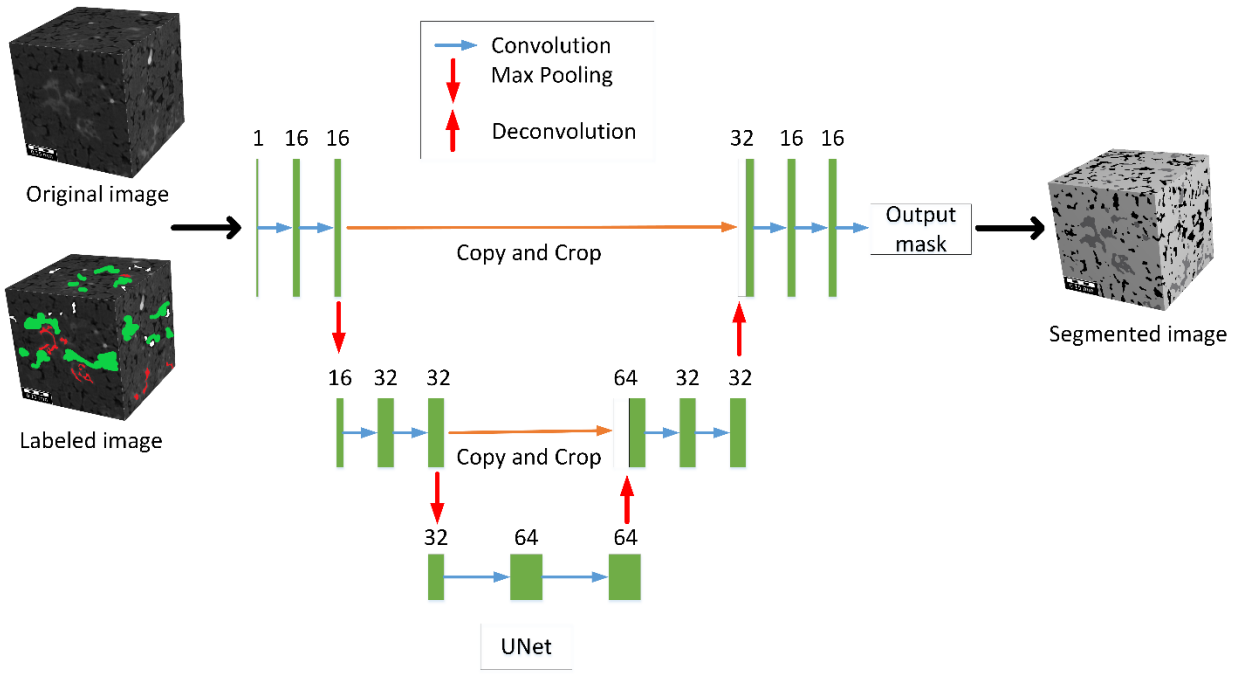

Figure 3-4 Segmentation process using the UNet architecture.

3.5 Watershed segmentation

To reconstruct a multi-scale image, the unresolved porosity phase should be replaced by the best match template extracted from the HR images. In this study, to reduce the computational cost and save memory consumption, the Watershed algorithm was used to decompose the unresolved sections of the LR images into smaller parts and subsequently replace each of them with a best

match from the HR templates. The traditional watershed algorithm is a region-based method that is widely used for image segmentation in various fields such as medical imaging, remote sensing, and computer visualization [145, 146]. However, this algorithm is very sensitive to imaging noise and can cause over-segmentation. Therefore, we applied the marker-based Watershed algorithm which resolves the issue by considering markers in the image. In this study, the marker-based Watershed algorithm of the "porespy" module [147] in Python programming language was used. Therefore, we applied this algorithm to unresolved sections of the LR images (as shown in Figure 3-5) to divide each unresolved volume into smaller regions (called 'unresolved masks' in Figure 3-5b). This can significantly reduce memory consumption and make the computations more effective during the replacement process.

The marker-based watershed algorithm can identify boundaries more effectively and is easily applied to 3D images. Therefore, we used this algorithm for our heterogeneous and 3D images to achieve our goals. First, the Euclidean distance map was calculated on the image. The binary image creates some artifacts in the distance map due to the voxelated nature. Therefore, a Gaussian filter with a sigma value of 0.4 was used on the distance map to smooth the image. Then, a maximum filter was applied to the image. By comparing the values obtained from the distance transform and the maximum filter, the peaks (markers) were then determined. To find peaks, a radius of 4 (r_max) for the spherical structuring element was used in the maximum filter stage. Moreover, some of the thus identified peaks were modified by removing the saddle peaks and merging the nearby peaks. In this research, a sigma of 0.4 for the Gaussian filter and a r_max value of 4 for the maximum filter was used.

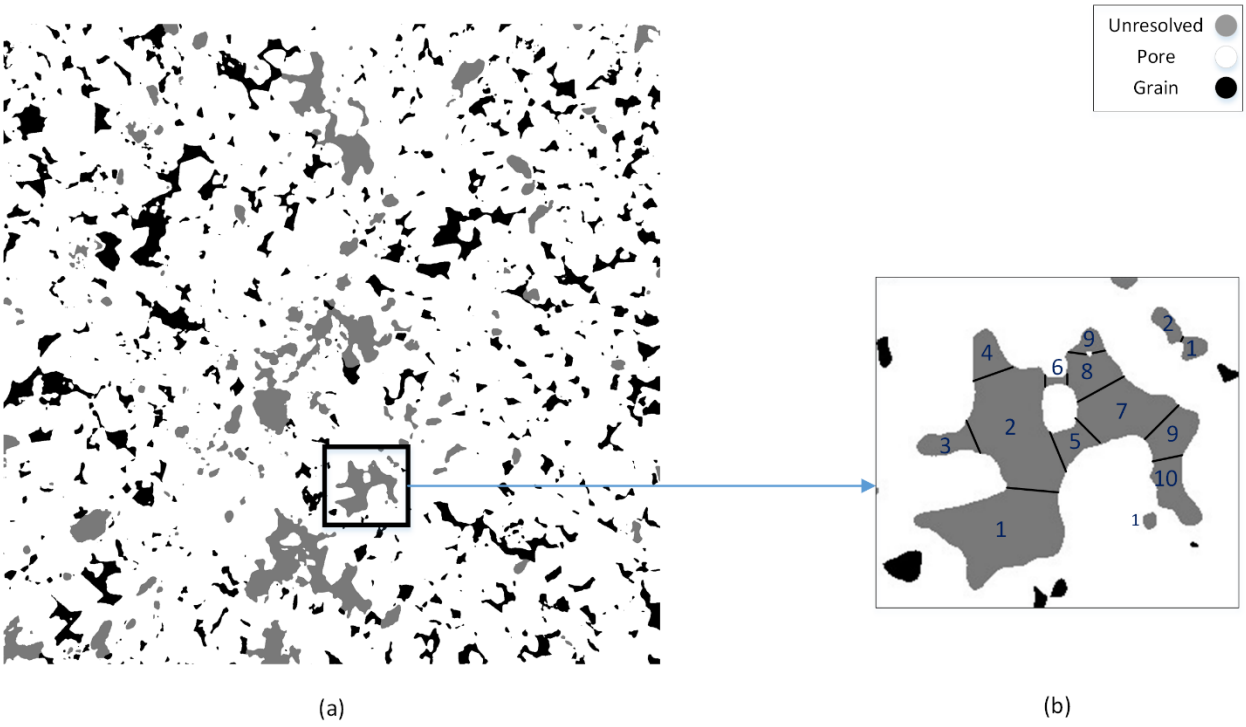

Figure 3-5 (a) A LR image segmented into the three phases pore, grain, and unresolved porosity. (b) The small segmented regions of the unresolved section in the LR image using the watershed segmentation algorithm.

The four terms that will be used extensively in the rest of this study are (i) unresolved cluster, (ii) unresolved region, (iii) unresolved mask, and (iv) unresolved template. As shown in Figure 3-6a, each distinct unresolved section (shown by a red colour line) of the image is called an unresolved cluster. An unresolved cluster could consist of one, or more than one, unresolved mask(s). The unresolved masks (shown by numbers) would be distinguished by applying the watershed segmentation on unresolved clusters. Each number in Figure 3-6a is an unresolved mask in its unresolved cluster. As shown in Figure 3-6b, the rectangle that encloses each unresolved cluster, is called an unresolved region. Moreover, the size of each of the rectangles, which enclose each unresolved mask, is computed. These rectangles are called unresolved templates (Figure 3-6b).

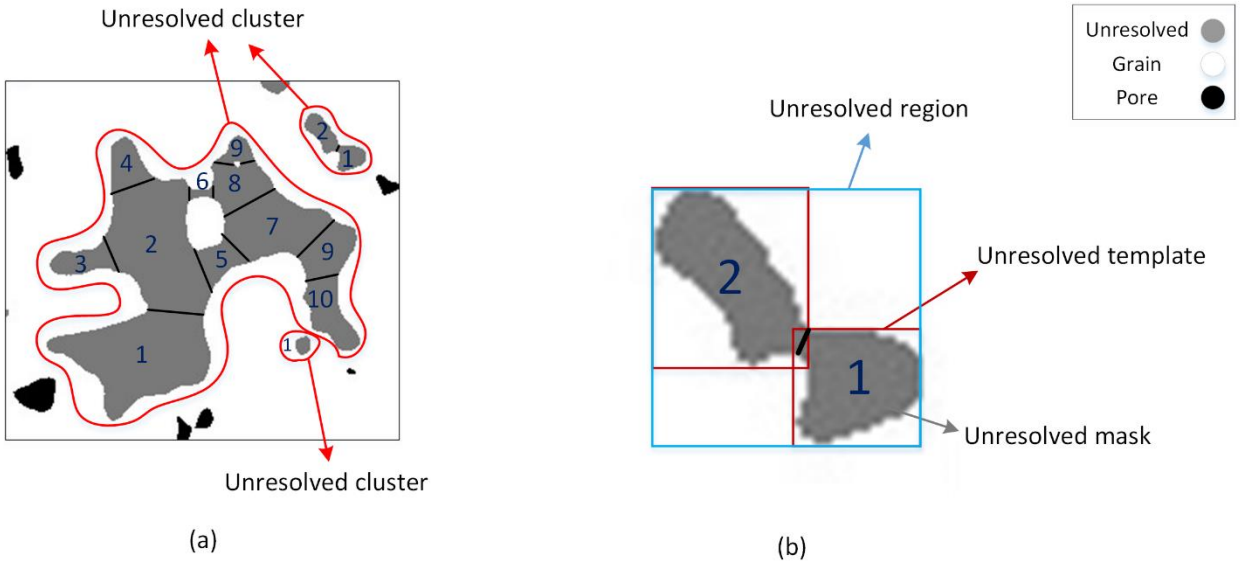

Figure 3-6 Unresolved mask and unresolved template of the unresolved section after watershed decomposition of unresolved regions. (a) A crop of the LR image is shown, which contains three unresolved clusters (shown by red colour lines). Moreover, numbers show the names of unresolved masks in each unresolved cluster. (b) One of the unresolved clusters that consists of two unresolved masks is shown. The blue line rectangle outside of the unresolved cluster is the unresolved region, and two red line rectangles outside of each unresolved mask are unresolved templates.

3.6 Cross-correlation Based Simulation (CCSIM)

The CCSIM is a pattern-based algorithm and is commonly used for geostatistical simulations but can be used also to reconstruct a new image based on the heterogeneity of an original image. This algorithm may be thought of as a Markov-chain model in which the probability of the next node is determined based on points simulated previously [8, 148]. The reconstruction process is started by selecting a random template from the training image (UT_1 in Figure 3-7a). This template is placed in the left bottom corner of the template region. Then, the next templates should be chosen by considering an OL along the raster path and solving the CCSIM similarity equation. The most similar pattern (with a higher CCSIM value) is selected as the next template at each stage. Three types of OL regions could be considered for solving the equation. These types of OLs are shown in Figure 3-7a and Figure 3-7d in red colour rectangles. The reconstruction process continues until whole templates are filled. The CCSIM method quantifies the similarity between the nodes based on the cross-correlation equation (equation 3-10) as follows:

$$C(i,j;x,y)=\sum_{x=0}^{l_x-1}\sum_{y=0}^{l_y-1}DI(x+i,y+j)D_T(x,y) \tag{3-10}$$

where $0\le i<L_x+l_x-1$ and $0\le j<L_y+l_y-1$. $DI(x, y)$ represents the location at point (x, y) of DI of size $L_x\times L_y$, with $x\in\{0,...,L_x-1\}$ and $y\in\{0,...,L_y-1\}$. An OL region of size $l_x\times l_y$ and a data event D_T with size $l_x\times l_y$ are used to match the pattern in the DI.

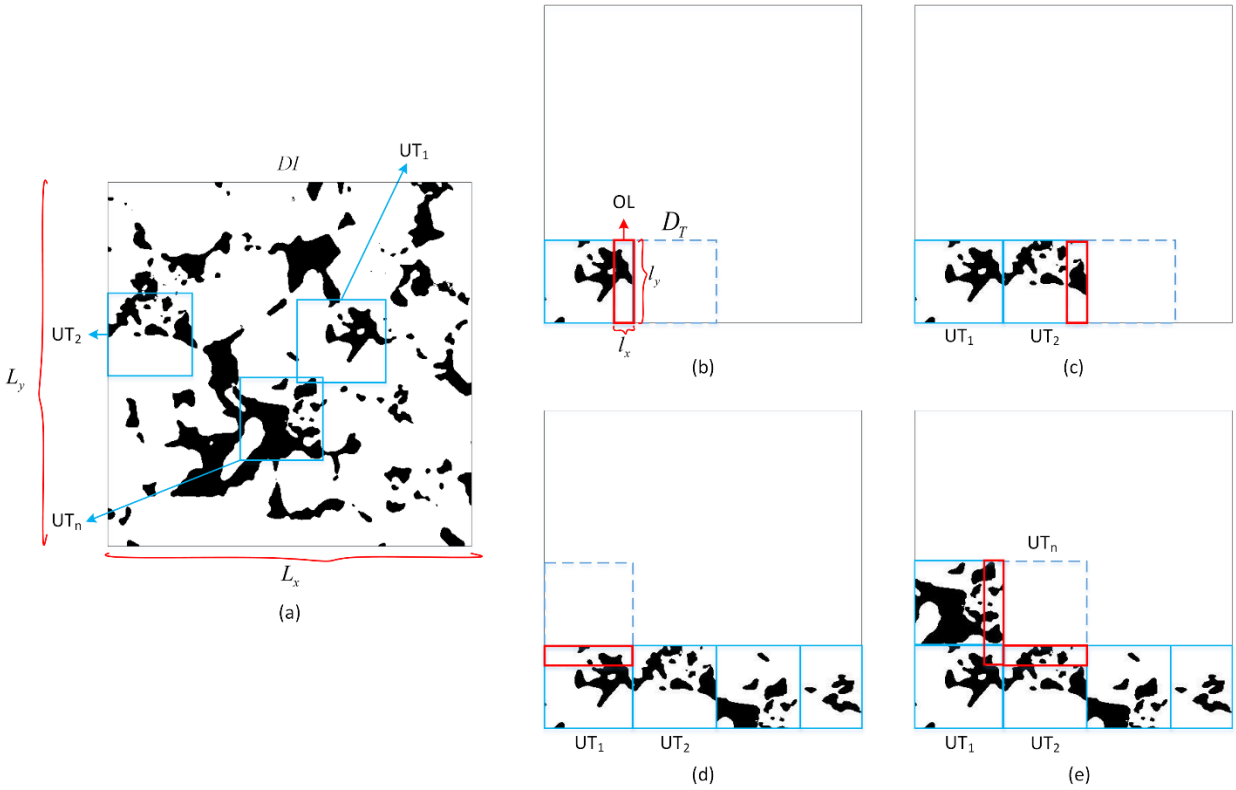

Figure 3-7 Workflow of the CCSIM approach, where (a) serves as the primary source image utilized to select the most suitable match templates. Image (b) shows how the initial template was chosen and positioned in the left-bottom corner of the image (indicated by the blue line rectangle). Additionally, the OL region marked by the red line rectangle, is utilized to select the subsequent template in the horizontal direction (as represented by the blue dotted line rectangle). Image (c) depicts the first type of OL region and the next template selection in the horizontal direction, while (d) depicts the second type of OL region and the next template selection in the vertical direction, and (e) illustrates the third type of OL region for templates within the image that are in contact with the selected previous templates from two directions.

3.7 Multi-scale Image Reconstruction

We used BS and EBC rock samples for multi-scale image reconstruction using three different approaches in this study. As mentioned, we implemented three approaches for the multi-scale reconstruction of images after clarifying the unresolved porosity and unresolved masks. In the first approach, a modification was applied to the Wu, Tahmasebi [9] model for reconstructing multi-scale images, which we refer to as the "Modified Wu et al. method". In the second model, a novel CCSIM watershed-based Multi-scale Reconstruction is introduced, referred to as CWMR. Moreover, In the third approach, we modified the CWMR approach and presented a new model for multi-scale image reconstruction using the Octree structure, which reduces memory consumption and computational cost. This approach is called Octree CCSIM-based Watershed Multi-scale Reconstruction (OCWMR). In the following, we have explained each of these approaches in detail along with the corresponding figures. Moreover, in these explanations, it is specified which image (original or resampled) each method uses to determine the phases and reconstruct the multi-scale images.

3.7.1 Modified Wu et al. Method

In the Wu, Tahmasebi [9] study, the reconstruction process was carried out on grayscale images, and the best match templates were chosen using the CCF equation (Equation 3-10). However, the region selection process on the LR images was not quite well explained in that study. Therefore, in an attempt to clarify the unresolved sections (Figure 3-6) for the Wu et al. study, a novel approach is introduced and named the 'Modified Wu et al. method'. This modified Wu et al. method is started by clarifying the unresolved regions and clusters on the image based on the concept described in Figure 3-6. The workflow is then continued by reconstruction of the unresolved regions by considering the best match from HR templates as shown schematically in Figure 3-8. Figure 3-8a depicts an HR image, from which the best match templates are to be selected. Figure 3-8b illustrates an unresolved region of the LR image. Figure 3-8c shows an OL (shown in red) of the unresolved region. In Figure 3-8d, the CCF equation is computed on the HR image and the best match template is selected and inserted in the unresolved template (shown by a blue square in Figure 3-8a). The unresolved cluster remains unchanged, while the outside voxels are removed and replaced by the LR image (Figure 3-8e). This process is to be carried out in all unresolved regions and can be applied to both 2D and 3D images. In this study, it was applied in

3D to replace the whole unresolved porosity in the LR image and to construct the final multi-scale image.

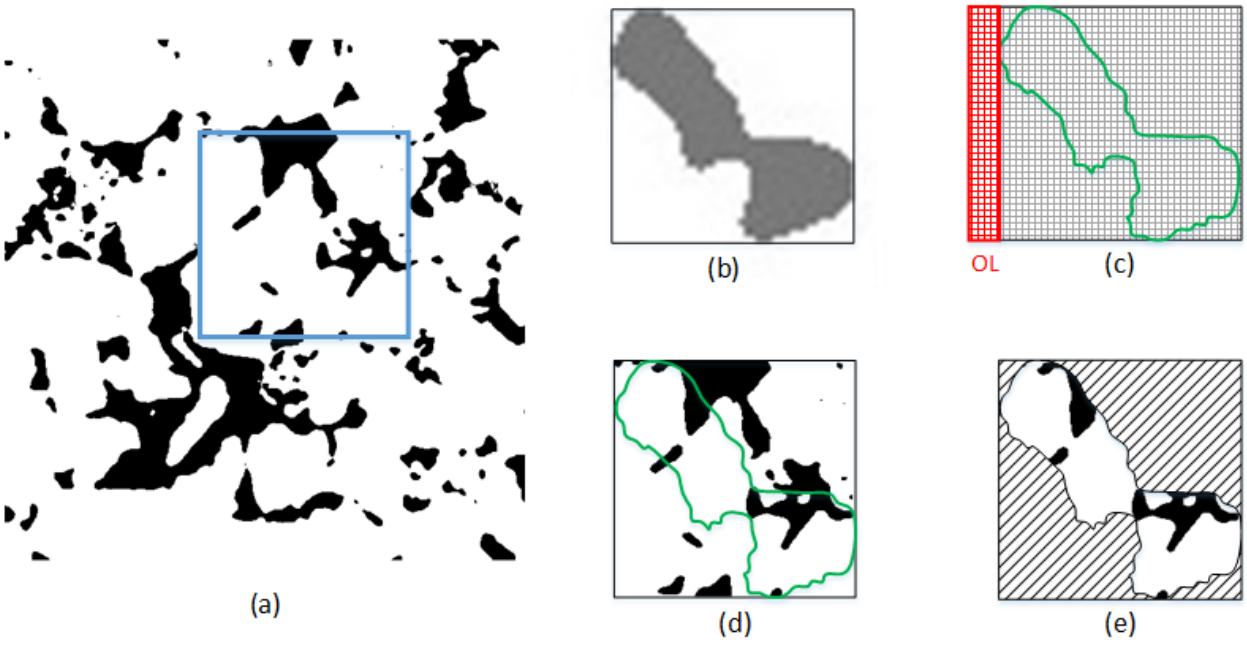

Figure 3-8 Workflow of the modified Wu et al. method, with (a) the original HR image, utilized to select the best match templates, (b) one of the unresolved regions in the LR image, (c) the pixel size of the unresolved region of (a) and the OL area for solving the CCF equation, (d) the selected best-match template from the HR image, which is placed within this unresolved region, and I the pixels preserved inside the unresolved cluster, while the remaining pixels outside of the cluster are removed and the corresponding pixels from the LR image are placed inside them.

3.7.2 CCSIM Watershed Multi-scale Reconstruction (CWMR)

The novelty of the CWMR in this research is based on considering smaller unresolved cubes and incorporating a novel OL selection procedure. It focuses on unresolved templates with significant numbers of micro-pores. Unlike the modified Wu et al. method, this approach reconstructs the unresolved templates only rather than the entire unresolved region (Figure 3-6b). This reduces computational memory costs and better preserves connections across different scales. To decrease simulation run time, suitable templates were selected from the cropped size of HR images. The HR image was cropped to twice the dimensions of the template and the best template was then selected from this crop. Therefore, this assumption decreases the run time as well. Moreover, instead of selecting the pattern with the highest CCSIM value, the template with an average

CCSIM value was selected. This ensures that the chosen template has a significant number of micro-pores while maintaining suitable connections across scales.

For a better visualization, Figure 3-9 depicts the workflow of this approach in 2D; however, the actual process was coded and applied in 3D. Figure 3-9a illustrates an HR image, from which the best match templates were to be selected. Figure 3-9b depicts an unresolved region of the LR image and highlights two unresolved templates using numbers. Figure 3-9c shows the procedure of the OL selection for the first unresolved template. The right and bottom sides of the unresolved template are considered as Ols. Then, the CCF equation (Equation 3-10) is computed on the cropped HR image and the first best-match template (UT_1) is selected as shown in Figure 3-9a. The selected template is in the first unresolved template of the unresolved cluster as shown in Figure 3-9d. In Figure 3-9e, the procedure of OL selection for the next unresolved template is illustrated. Same as the first one, the right and bottom sides of the second unresolved template are considered as Ols. Then, the CCF equation is computed on the cropped HR image and the second-best match template (UT_2) is selected and replaced in the LR image as shown in Figure 3-9a. The selected template is located in the second unresolved template of the unresolved cluster as shown in Figure 3-9f. Once an HR template is selected for each unresolved template (Figure 3-9d and Figure 3-9f), the unresolved mask is preserved, meaning that the pixels outside the mask in the unresolved template are replaced with the original pixels in the LR image (shown with hatch lines in Figure 3-9g). Furthermore, pixels corresponding to just one of the unresolved templates are placed in the area where two unresolved masks overlap. In other words, the pixels of the second image in that region are ignored.

This process is repeated for all unresolved templates until all clusters in the LR image are filled with their corresponding HR templates. The result is a multi-scale image that combines information from both the HR and LR images, allowing for a more detailed and accurate representation of the underlying feature or object.

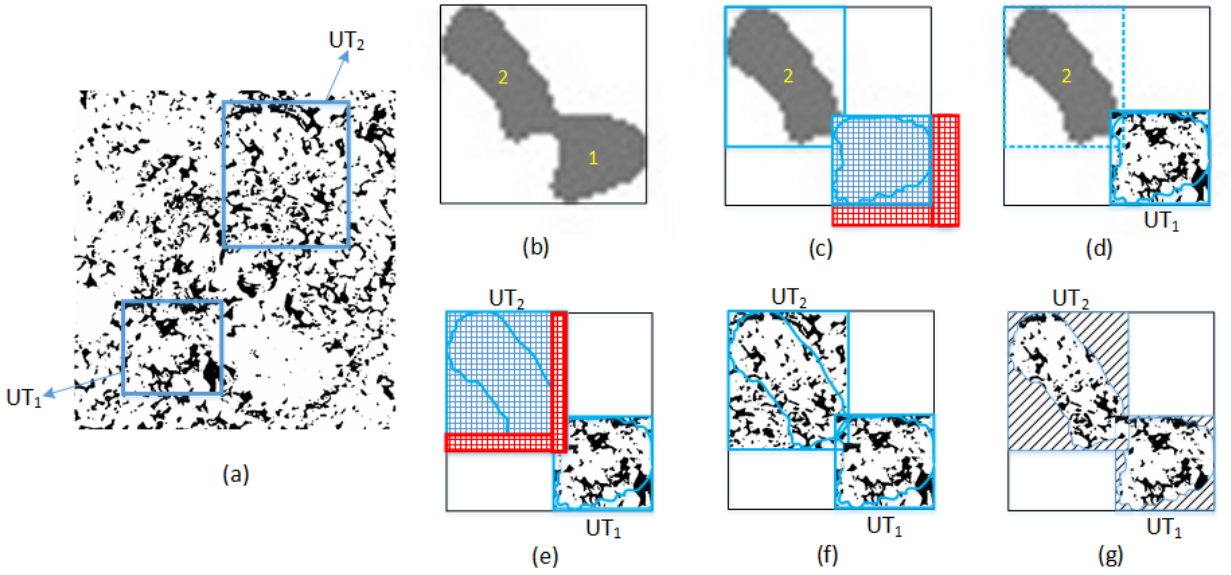

Figure 3-9 Workflow of the CWMR, where (a) represents the HR image, (b) one of the unresolved regions from the LR image with two unresolved masks inside of it, (c) the pixel size of the first unresolved template and the corresponding OL area for solving the CCF equation, (d) the selected best-match template from the cropped HR image, placed within the first unresolved template, I the pixel size of the second unresolved template and the corresponding OL area for solving the CCF equation, (f) the selected best-match template from the cropped HR image as placed within the second unresolved template, and (g) the pixels preserved inside the unresolved templates, while the remaining pixels outside are removed, and the corresponding pixels from the LR image are placed inside (not shown here).

Figure 3-10 illustrates the process of OL selection for each unresolved template. In both Figure 3-10a and b, the dimensions of the first and second unresolved templates are denoted $w_1 \times h_1$ and $w_2 \times h_2$, respectively. For the first unresolved template, the OL is considered as two adjacent regions located outside of it (shown in green), with dimensions equal to one-fifth of the first unresolved template ($\frac{w_1}{5} \times \frac{h_1}{5}$), extending beyond its boundaries. To determine the two desired directions for the OL, the arrangement of the first and second unresolved templates must be considered. If the second unresolved template is positioned in any direction relative to the first unresolved template, the OL regions are taken on the opposite side. For example, In Figure 3-10a, the second unresolved template is situated on the upper-left side of the first template and, therefore, the outer right-bottom regions (green rectangles) of the first template are selected as the OL. Moreover, in Figure 3-10b, the second unresolved template is situated on the upper-right side of the first template and, therefore, the outer left-bottom regions (green rectangles) of the first

template are selected as the OL. In the context of a 3D image, an additional dimension has to be added to the Ols and an extra OL to be incorporated into the third dimension. The procedure for defining this new OL and its size must follow the same approach as for the previously mentioned Ols employed in the 2D images.

For the next unresolved templates (2^{nd}, 3^{rd}, …, n^{th}), two types of Ols named main and secondary Ols are defined. Two cases can happen for specifying these Ols. In Figure 3-10a (the first case), two unresolved templates have an overlapping region. The main OL is determined in the direction where the two unresolved templates are in most contact, which in this case happens to be in the vertical direction. The main OL is represented by a yellow color and its width is equal to the width of the overlapping region (w'), while its height is equal to the height of the second unresolved template (h_2). Therefore, the horizontal OL shown in red is considered a secondary OL and its height is taken as one-fifth of the height of the second unresolved template, $\frac{h_2}{5}$. Both the main and econddary OLs are located inside the second unresolved template.

In Figure 3-10b (the second case), the two unresolved templates do not overlap with each other. In this situation, the main OL is determined in the direction where the two unresolved templates are in most contact, which in this case is along the horizontal direction. The main OL is represented by the yellow color and its width is equal to the width of the overlapping region, w_2, but it is located outside the second unresolved template. As there is no overlapping region in this case, its height is considered one-fifth of the height of the second unresolved template, $\frac{h_2}{5}$. The vertical OL indicated in red colour is taken as the secondary OL, and its width is one-fifth of the width of the second unresolved template. In the context of a 3D image, an additional dimension must be added to the main and secondary Ols and an extra OL must be incorporated into the third dimension. One main OL and two secondary Ols should be specified. The procedure for defining these Ols and their sizes follows the same approach as employed for the previously mentioned Ols in 2D images.

The CCSIM method typically considers the OL size to be one-sixth or one-fifth of the template size. We chose one-fifth for a better overlap with the template. Using a fixed size for Ols is impractical due to varying template sizes. A fixed size might be too large for one template and too small for another, or even larger than the template itself, causing bias in the reconstruction process. We also modified the CCSIM method to maintain accuracy in anisotropic structures. For this Ols

were selected in three directions separately, allowing the CCF to choose the best match template according to the previous template.

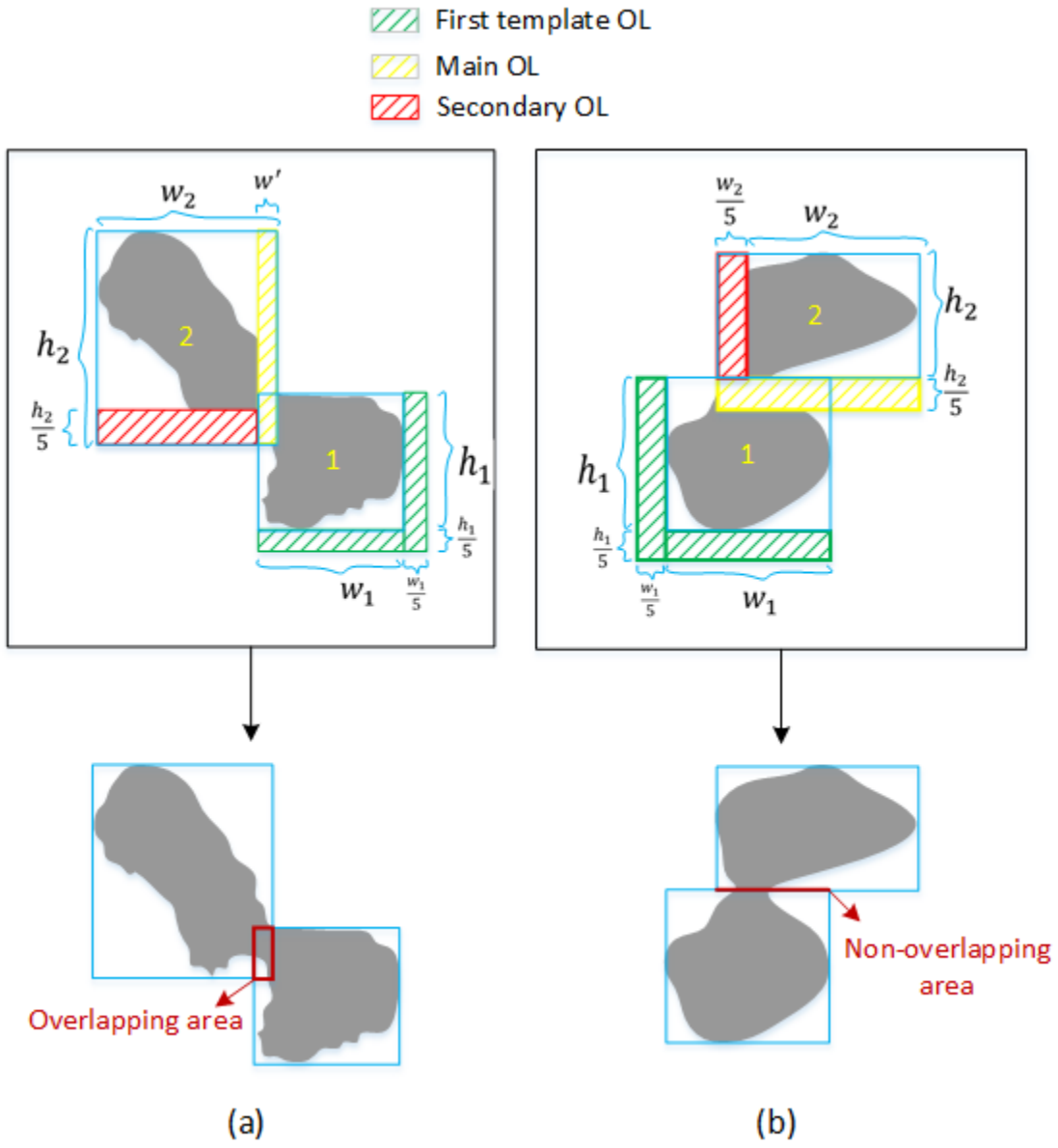

Figure 3-10 Selection of OL for unresolved templates in the CWMR involves green rectangles for the first pattern. Subsequent patterns have main (yellow) and secondary (red) rectangles. For the main OL, two cases are considered: one for overlapping templates and one for non-overlapping templates. In the overlapping case (a), the main OL aligns with the greatest contact's direction and its width equals the overlapping region's width. Secondary OL is in a different direction, inside the second template and its height equals one-fifth of the second template's height. In the non-overlapping case (b), the main OL aligns with the greatest contact's direction outside the second template,

whereby its height is one-fifth of the second template's height, while the secondary OL in a different direction is one-fifth of the second template's width.

3.7.3 Octree CCSIM-based Watershed Multi-scale Reconstruction (OCWMR)

In the CWMR, the amount of memory consumption during computations remained significantly high. To address this issue, we have introduced the OCWMR approach in this research, aimed at further reducing the computational cost. Like the CWMR, the OCWMR approach incorporates watershed segmentation and employs the CCF equation for multi-scale image reconstruction. Moreover, to achieve the highest accuracy for the multi-scale reconstructed images, we performed a sensitivity analysis on the sigma and r_{max} parameters in the watershed algorithm to choose the best values for reconstruction. For this purpose, porosity and permeability values were calculated for reconstructed images with different sigma and r_{max} values. However, the main difference between OCWMR and CWMR was the utilization of an Octree structure. An Octree is a data tree structure in which each internal node has exactly eight children. Octrees are often used to represent a three-dimensional space by recursively dividing that space into eight equal parts (Figure 3-11a). Octrees are actually equivalent to four trees in three dimensions [112]. 3D space modeling is a very important operation that takes up a lot of memory capacity in computers. The Octree is a method that can display the 3D space in a lighter way by occupying less memory space [123, 124, 149].

In applying this methodology, we started with watershed segmentation on the LR image, subsequently identifying unresolved templates within the image. Note that unlike the CWMR approach, the OCWMR involves solely resampling the unresolved templates to ensure that their voxel dimensions are equal to those of the HR image. This implementation essentially transforms the LR image into an Octree structure (as depicted in Figure 3-11b). Within this structure, the unresolved porosity along with some adjacent voxels (resulting from the resampling of unresolved templates, which incorporates some voxels outside the unresolved porosity) exhibits the fine voxel size. Conversely, the remaining areas (pores and grains) are characterized by a coarser voxel size [123, 124, 149].

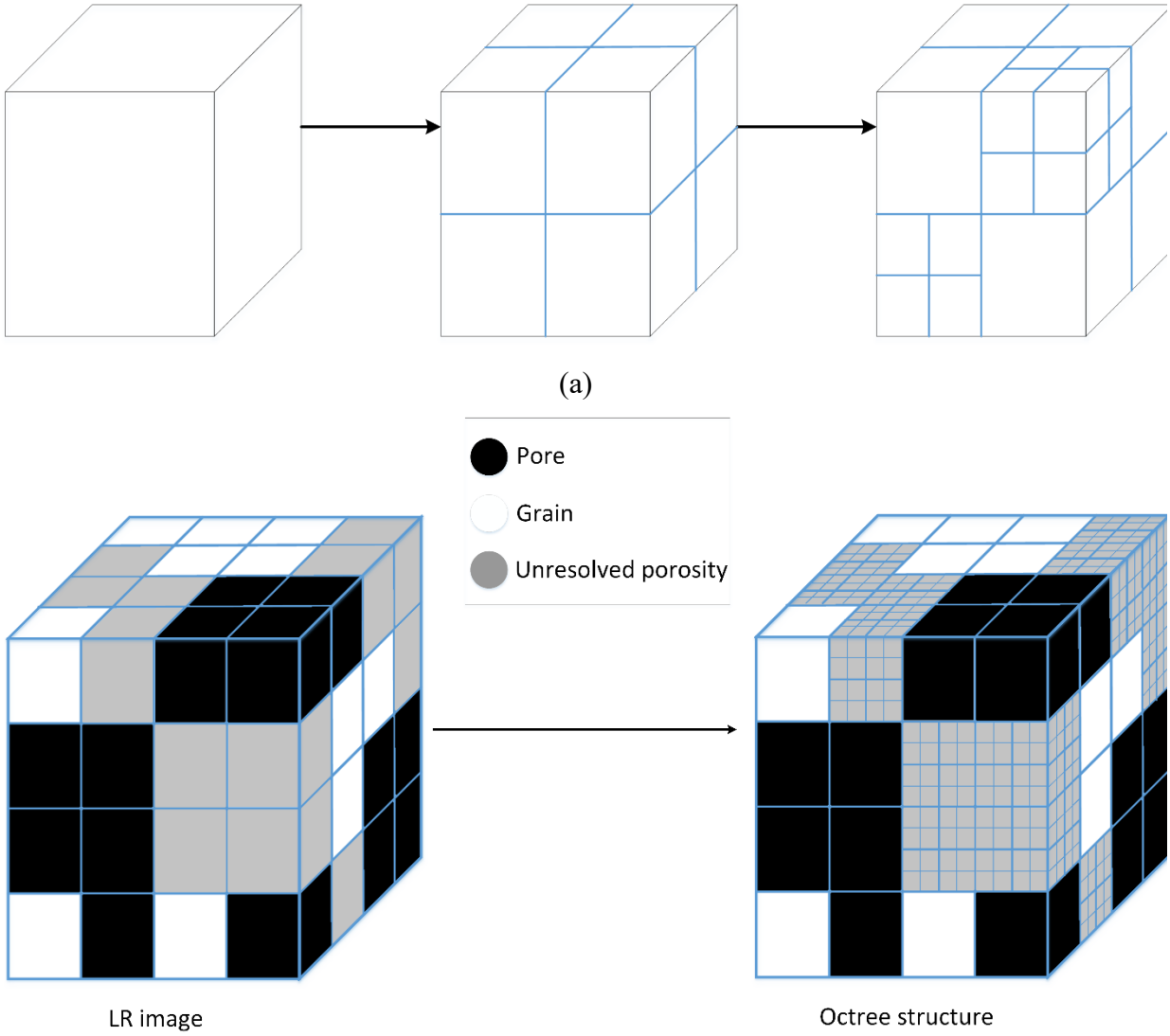

Figure 3-11 (a) Octree structure and how it divides the space into smaller parts. (b) LR image to Octree structure conversion. In this structure, the voxel size is reduced in the areas of the unresolved porosity (the parts shown with gray color) and remains constant in the rest of the areas (black and white areas that show the pore and grain phases, respectively). Therefore, calculations are performed only on unresolved areas with small voxel sizes.

Next, using the CCF equation, we proceeded to select the best-match template for each unresolved template. The schematic for selecting the templates from the HR image is shown in Figure 3-12, where the HR image serves as the source for template selection. In Figure 3-12a, an unresolved cluster is depicted which, after watershed segmentation, is transformed into two unresolved masks or templates. Consequently, for each of these unresolved templates, an appropriate template must be chosen from the HR image. Figure 3-12b highlights the unresolved template area, characterized

by small-sized voxels, and the OL area, characterized by larger-sized voxels owing to the inherent nature of the Octree structure. In Figure 3-12b, the OL area exhibits a larger voxel size since it lies outside the unresolved template area. Therefore, in the beginning (Figure 3-12c) the voxel size of the OL region is resampled to match that of the HR image. Now, with the unresolved template area and OL specified, the best template can be found using the CCF equation from the HR image, and this selected template can be placed into the first unresolved template area of the LR image (Figure 3-12d). Subsequently, the same approach is applied to select the best-match template for the next unresolved templates. Figure 3-12e shows the areas of unresolved templates with small voxel sizes and OL regions with both small and large voxel sizes. In this figure, the main and secondary OL areas lie outside the unresolved template area and feature large voxel size. Therefore, initially, we resample the voxel size of both OL areas to match that of the HR image (Figure 3-12f). Now, with the unresolved template area and OL defined, the best template can be selected using the CCF equation from the HR image, and this chosen template can be placed into the second unresolved template of the LR image (Figure 3-12g). Finally, as depicted in Figure 3-12h, we retained the voxels within the unresolved mask. Additionally, in the overlapping regions between the two unresolved templates, we incorporated the voxels from the selected template for the first unresolved template into the final image. This entire process was repeated for all unresolved templates within the LR image structured with an Octree structure, ultimately resulting in the construction of a multi-scale image. This innovative method introduced an efficient detour that significantly reduces computational costs through the utilization of the Octree structure.

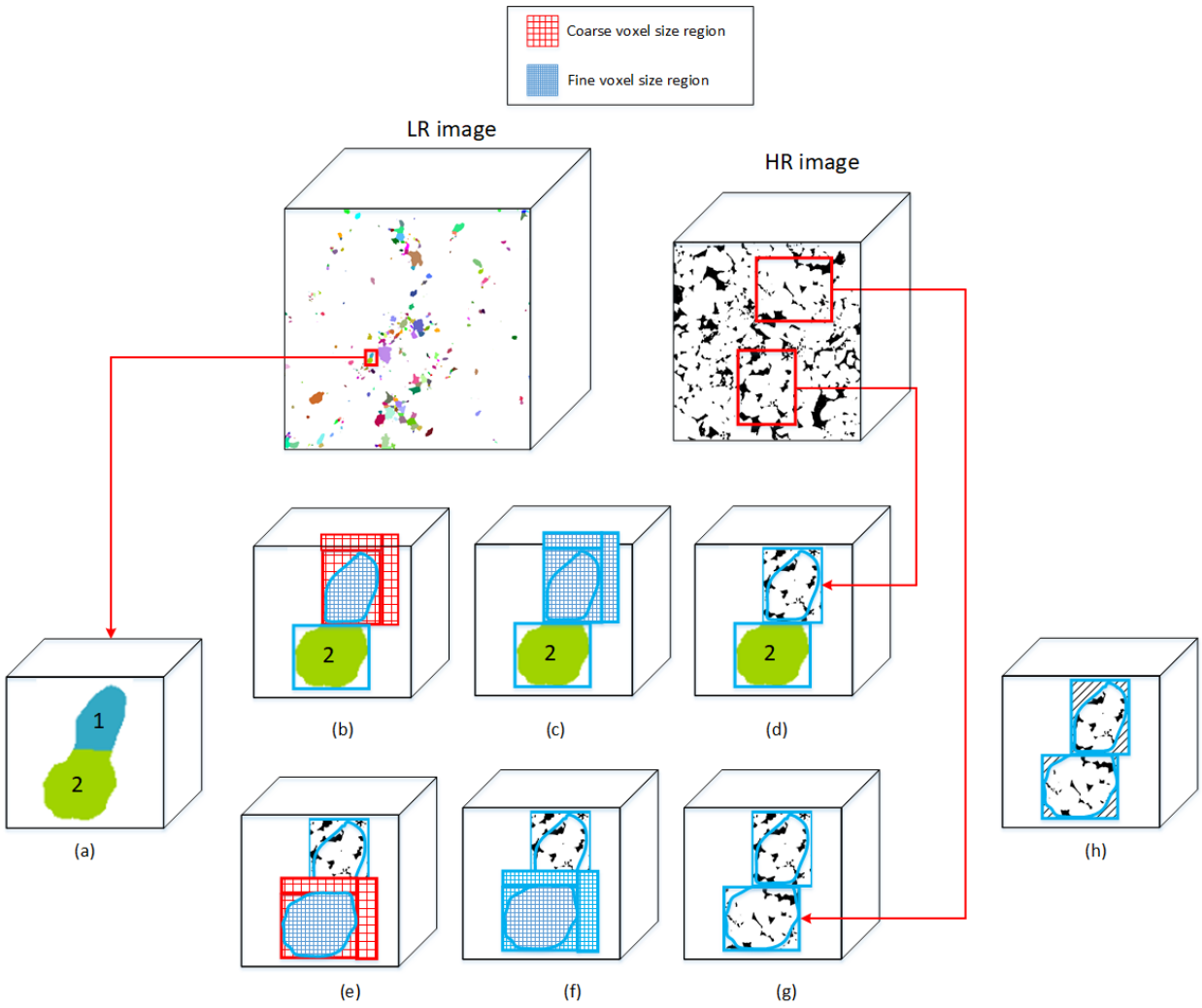

Figure 3-12 Workflow of the OCWMR, (a) one of the unresolved clusters from the LR image with two unresolved masks inside it, (b) the pixel size of the first unresolved template and the corresponding OL area with large pixel size for solving the CCF equation, (c) the OL is resampled to the small size so that it can be used in the CCF equation, (d) the selected best-match template from the HR image, placed within the first unresolved template, (e) the pixel size of the second unresolved template and the corresponding OL area with large pixel size for solving the CCF equation, (f) this OL is also resampled to the small size so that it can be used in the CCF equation, (g) the selected best-match template from the HR image as placed within the second unresolved template, and (h) the pixels preserved inside the unresolved templates, while the remaining pixels outside are removed, and the corresponding pixels from the LR image are placed inside (not shown here).

3.8 Network extraction

After reconstructing multi-scale images, it is time to reconstruct multi-scale PNM. PNM consists of pores and throats that are extracted from the binary image. There are two hmain algorithms used by researchers in various studies to extract the PNM from images. The first method is the Sub-Network of an Over-segmented Watershed (SNOW) algorithm, which extracts the pore network based on the peaks determined on the basis of the Euclidean distance and watershed segmentation on the images. The second method is the maximum ball method, which extracts the network of pore and throats based on the maximum ball that can be placed in the empty space of the images. In the following, each of these methods is explained in more detail.

3.8.1 SNOW

The SNOW algorithm obtains a distance transformation or distance map for pore space. The voxel-like nature of binary images may introduce some artifacts in the distance map, including spurious and misidentified peaks. To remove these artifacts, the algorithm applies a Gaussian blur filter on the distance map to smooth the image and reduce the occurrence of these plateaus. Next, the algorithm continues by identifying peaks in the smoothed distance map using a maximum filter with a spherical structural element of radius R. The maximum filter replaces each voxel in the image with the maximum value in its neighborhood. Local peaks retain their value, while other voxels are overwritten with a larger value. Then, peaks are identified by locating voxels in the filtered image that are equal to the distance map, resulting in a Boolean mask with actual values in the peaks. After finding a set of peaks, the next step is to remove spurious peaks that lie on saddles and plateaus. In high-porosity materials, pores are usually large compared to solid features and may produce closely spaced peaks. The spheres centered on these adjacent peaks overlap significantly, so usually only one of these peaks needs to be retained. Finally, these steps generate a set of markers that are passed to the marker-based watershed algorithm to obtain a segmented image [150]. Finally, the pore network is extracted from the image, which is shown in Figure 3-13.

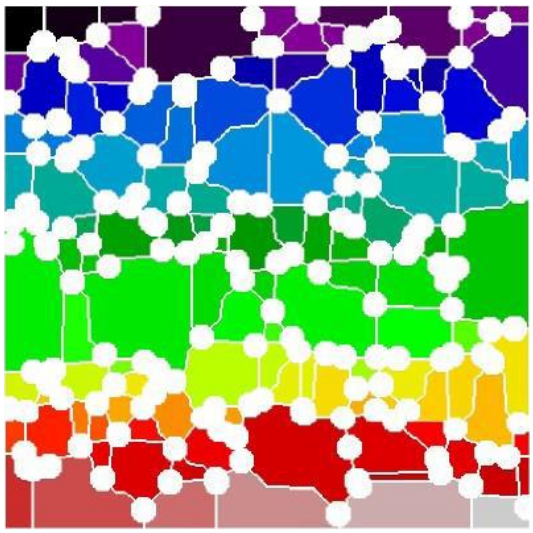

Figure 3-13 The final tomography image after applying the SNOW method [150]

3.8.2 Maximal Ball (MB)

This algorithm differentiates between pores and throats and develops volume and continuity based on that and finally builds a ball and rod model based on the space of pores. The use of this method provides the possibility of simulating mercury injection and calculating capillary pressure. The skeleton of points is conceptually close to the medial axis, but in general, the medial axis is always a subset of the skeleton. Each point in the three-dimensional space is characterized by three Cartesian coordinates (x.y.z). The Euclidean distance between two points is calculated by equation 3-11.

$$dist(r, r_0) = \sqrt{\left(x_1 - x_2\right)^2 + \left(y_1 - y_2\right)^2 + \left(z_1 - z_2\right)^2} \tag{3-11}$$

A sphere with radius R centered at r_0 represents a set of points with radius r. If $dist\ (r, r_0) \leq R$, this sphere is defined as B_R. Suppose M is a group in R^3, in this model M represents the space of rock pores. The complement of this set is defined as M^c. If the ball $B_R(r_0)$ is a subset of M and is not a subset of any other ball that is a subset of M, then the ball is called a maximal ball centered at r_0. In general, a ball can be maximum if it touches M^c at one point. The algorithm starts with the maximum ball with zero radius and at each step the radius increases by one unit (each unit is a voxel) until it reaches the solid phase. The search for the maximum radius can be increased by the

ball construction algorithm and reduced by using the information about the radii previously calculated for the neighboring voxels [151].

In the MB method, the largest possible sphere is included in the space of the pores in the image, and then throats between the spheres are added. The spheres should be the largest possible pores that contact the surface of the grain on the image. In the place where one sphere is placed, no other sphere is placed. Therefore, with a general view, we must first place the largest sphere on the pore space of the images, and as it is clear in Figure 3-14, after that, remove the spheres that are placed on top of each other and consider a final sphere in their place. (the largest sphere is kept and the others are removed) [39].

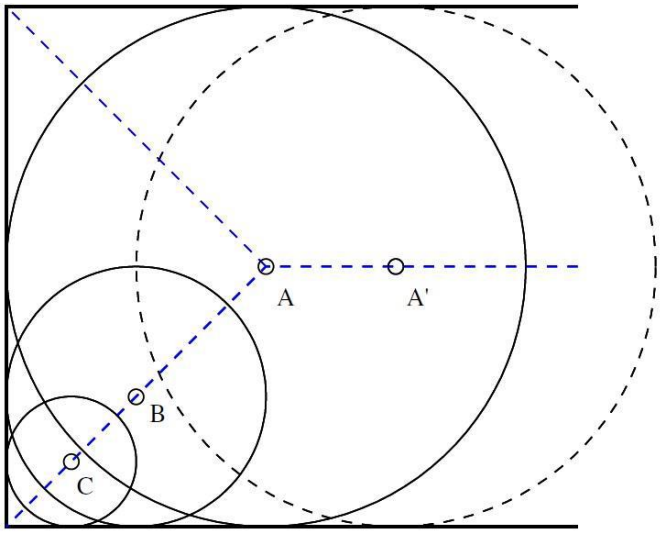

Figure 3-14 Shpere B is inferior to A and superior to C, and after applying the hierarchy, spheres B and C are both inferior to sphere A [39].

But in Dong's method, instead of increasing the spheres one by one to reach the solid surface, it first finds the closest solid and then defines the empty space based on it, which makes the radius obtained for the throats more realistic. Moreover, in Al-Kharousi's method, in addition to the dominant and inferior spheres, another sphere is also considered under the name of lattice pore, which are spheres with the same diameter that overlap or touch each other. In this method, the spheres of the network are considered as throats, which can be seen in Figure 3-15 [152, 153].

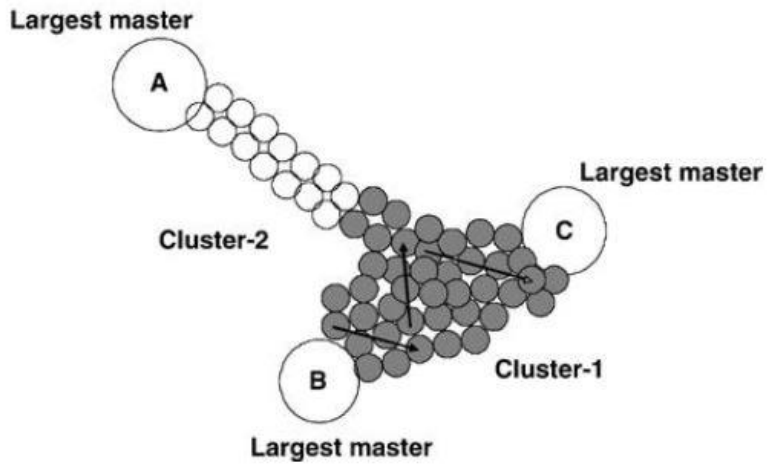

Figure 3-15 Pore network spheres in the MB method and considering the proper pores as throats [152]

3.9 Multi-scale PNM

This research introduces a new method for multi-scale PNM reconstruction to improve the accuracy of reconstructed networks. We use ILS rock for this purpose. Various methods have been proposed for multi-scale PNM reconstruction, using information from different scales. However, a common challenge in these approaches is the correct connection between scales and the proper assignment of features to the added throats. In this study, we compare our method with the approach of Moslemipour and Sadeghnejad (2021) [20] and demonstrate the importance of scale connectivity for accurate multi-scale PNM reconstruction. To address this, we developed a method that reconstructs PNM from two scales separately, ensuring higher accuracy. Our novel fusion method for multi-scale PNM modeling resolves the key issue of connecting scales while maintaining accuracy.

In this research, the multi-scale PNM is reconstructed from the LR image. This means that the LR image is segmented into 3 phases of pores, grain and unresolved porosity, and the PNMs in the unresolved porosity sections are reconstructed using the statistical information of PNM extracted from the HR image.

The PNM extracted from the resolved porosity contains large pores, while the PNMs in the unresolved porosity sections consist of small pores. We then use an ANN trained on the pores and throats from the PNM extracted from the HR image. This ANN connects the PNMs extracted from both the resolved and unresolved porosities. It can also link unresolved PNMs to one another if

necessary. Ultimately, this process reconstructs the multi-scale PNM. Using the ANN trained on the HR image improves the accuracy of the connections between pores at different scales. This improvement enhances the accuracy of the properties calculated from the reconstructed PNM.

The workflow for multi-scale PNM reconstruction in this study is shown in Figure 3-16. We introduced a new approach for multi-scale PNM reconstruction based on ANN, called ANN Multi-scale PNM Reconstruction (ANN-MPR). First, we extract PNM from both LR and HR images. Next, we generate different stochastic PNMs from the HR image, matching the size each unresolved cluster. By integrating these networks, the multi-scale PNM is reconstructed in different realizations using ANN-MPR. We then compare the reconstructed PNMs with the method proposed by Moslemipour and Sadeghnejad (2021). In this research, we refer to their method as Statistical Multi-scale PNM Reconstruction (Statistical-MPR), as it relies on statistical data for reconstruction. To validate the results, we compare the permeability of the multi-scale PNMs with the laboratory-measured permeability of the rock. This comparison highlights the importance of connectivity between scales. To further reduce memory consumption, we introduce an alternative to generating a stochastic network for unresolved porosity. This method, based on the octree structure, is called the ANN Octree Multi-scale PNM Reconstruction (ANN-Octree-MPR) method. Instead of generating a stochastic network for each unresolved cluster, we extract the pore network separately for each unresolved cluster from the selected template. To reduce computational costs when modeling and calculating properties of the reconstructed network, we also propose a new multi-scale upscaling method, which can be reconstructed on the multi-scale PNMs based on the effective hydraulic conductance values in each unresolved cluaster.

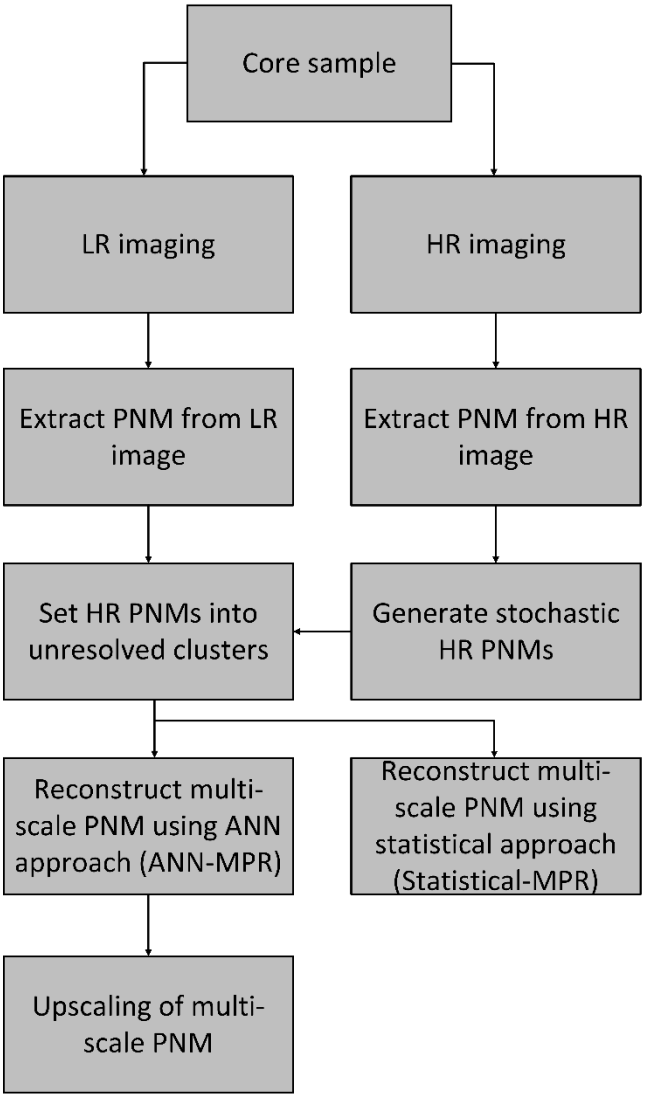

Figure 3-16 The workflow of stochastic-MPR and ANN-MPR methods

3.9.1 Network extraction

Before starting the multi-scale PNM reconstruction, it is necessary to extract the PNM from the HR and LR images. For PNM extraction from binary images, we use the SNOW algorithm from the PoreSpy module in Python [147]. The SNOW algorithm obtains a distance transformation or distance map for pore space. The voxel-like nature of binary images may introduce some artifacts in the distance map, including spurious and misidentified peaks. To remove these artifacts, the algorithm applies a Gaussian blur filter on the distance map to smooth the image and reduce the occurrence of these plateaus. Next, the algorithm continues by identifying peaks in the smoothed distance map using a maximum filter with a spherical structural element of radius R. The maximum filter replaces each voxel in the image with the maximum value in its neighborhood.

Local peaks retain their value, while other voxels are overwritten with a larger value. Then, peaks are identified by locating voxels in the filtered image that are equal to the distance map, resulting in a Boolean mask with actual values in the peaks. After finding a set of peaks, the next step is to remove spurious peaks that lie on saddles and plateaus. In high-porosity materials, pores are usually large compared to solid features and may produce closely spaced peaks. The spheres centered on these adjacent peaks overlap significantly, so usually only one of these peaks needs to be retained. Finally, these steps generate a set of markers that are passed to the marker-based watershed algorithm to obtain a segmented image [150].

3.9.2 Stochastic Network Generation

In this research, we employ three multi-scale PNM reconstruction methods. In two of them, networks for unresolved prosity are generated stochastically and share the same characteristics as the PNM extracted from the HR image. The method presented in Moslemipour and Sadeghnejad's 2021 paper is followed. Figure 3-17 shows the schematic of stochastic PNM generation. First, the pore and throat radii are calculated as well as the coordination number from the extracted PNM of the HR image. Using this statistical information, an equivalent stochastic PNM is then generated. Pores are distributed within the specified space according to their density. Pore radii are assigned based on the computed pore size distribution. Next, the pores are connected based on the coordination number, assigning throat radii according to the throat size distribution. Additionally, a series of optimizations are performed on the generated network. For example, overlapping throats are removed, as well as throats that are shorter or longer than the minimum and maximum lengths found in the HR image PNM.

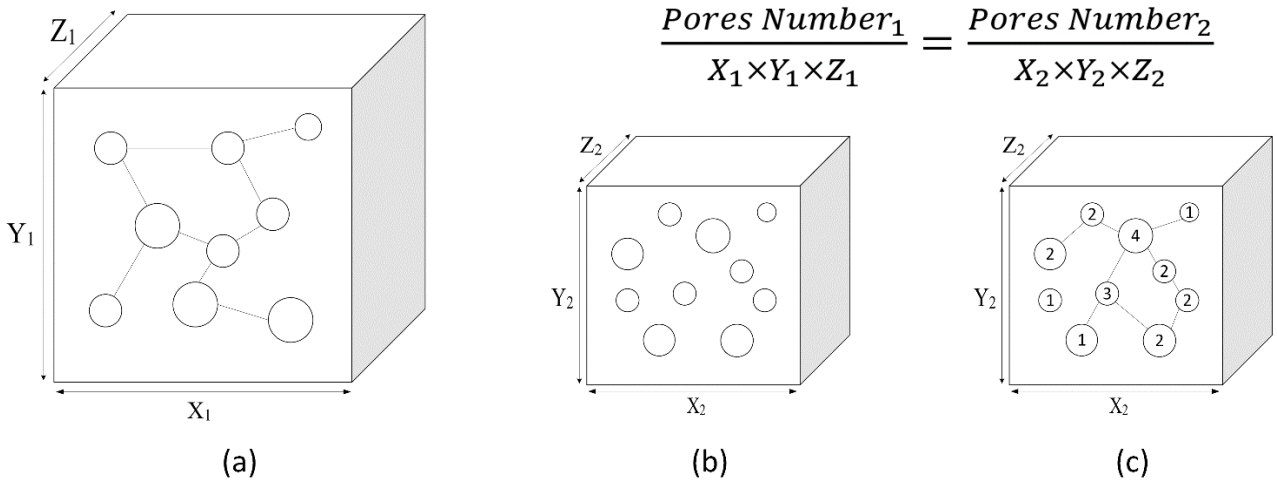

Figure 3-17 Stochastic PNM generation. (a) shows the extracted PNM from the HR image. (b) shows the first step for generating the stochastic PNM. Pore centers are distributed randomly in the PNM domain and each pore is assigned a diameter selected from the pore size distribution of the extracted network. Moreover, the density of pores in the stochastic PNM should be equal to the density of pores in the extracted network. (c) Each pore is assigned a coordination number selected from the coordination distribution of the extracted network. Then Each pore is connected to its nearby pores based on its assigned coordination number. Throat diameters are also assigned based on the throat size distribution of the extracted network.

3.9.3 Artificial Neural Network (ANN)

In this study, an ANN is used to add connections (throats) between the extracted PNMs, as shown in Figure 3-18. The ANN was trained using the PNM extracted from the HR image. This ANN determines whether to add a throat between the pores of each PNM. The trained ANN includes all pairs of pores in the PNM extracted from the HR image, along with the throats between them. This means every training data point for this ANN includes a pair of pores, represented by their diameters and coordinates, and a throat, defined by its length and diameter, if present, between them. The inputs to the ANN include the diameters of both pores and their coordinates. The output of the ANN indicates whether a throat is present between two pores and provides the throat's diameter and length. The ANN has eight input features: six represent pore coordinates, and two represent pore diameters. It produces three outputs. One output is for classification, where False indicates no throat, and True means a throat should be added. The other two outputs predict continuous values for the throat's length and diameter. The ANN consists of two hidden layers. Each layer uses the ReLU activation function. The first hidden layer contains 128 neurons, while the second has 64 neurons. Adam's optimizer is employed to update the network's weights.

Classification accuracy is used as the evaluation metric for the classification task. For regression tasks, mean square error (MSE) is the chosen evaluation criterion.

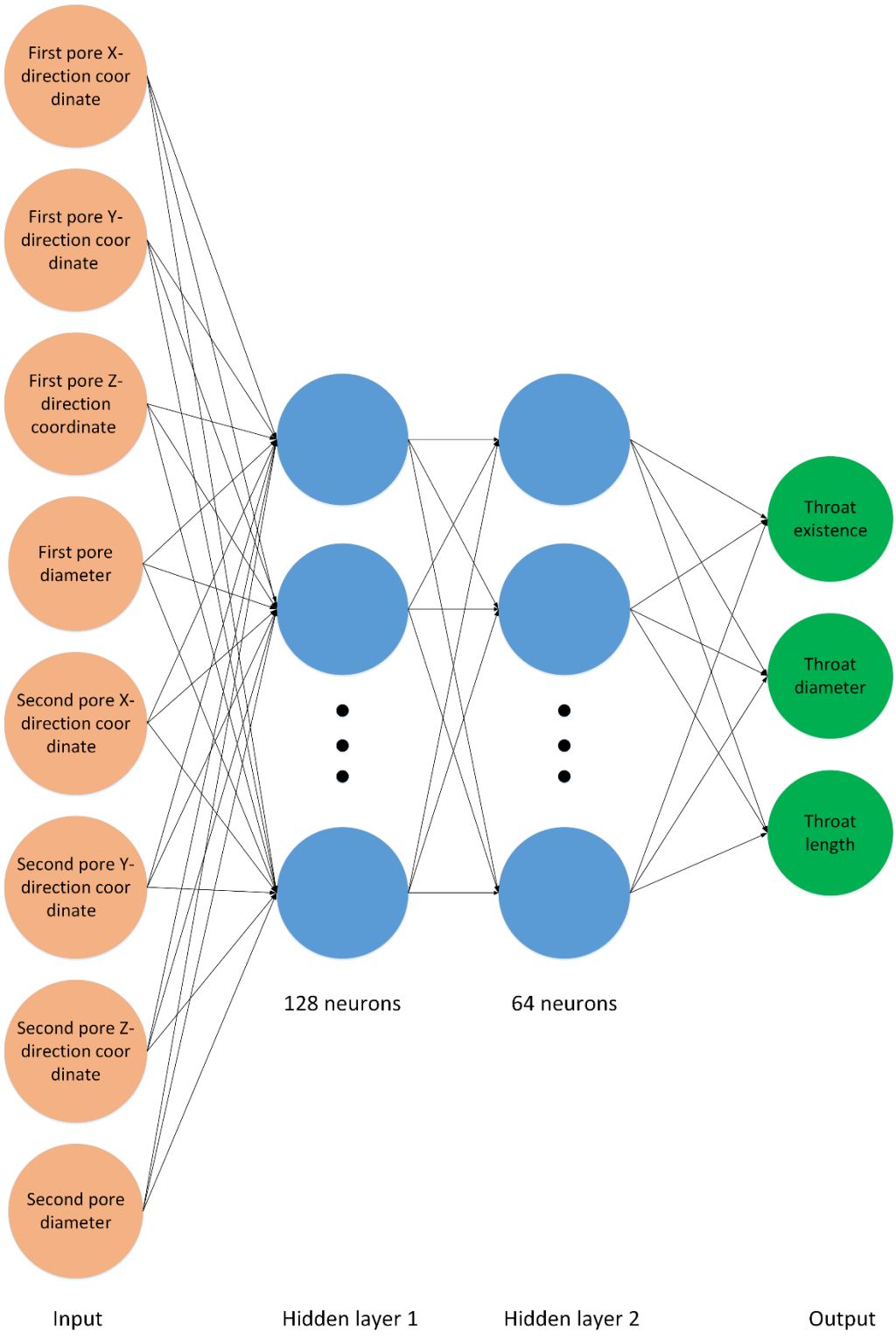

Figure 3-18 The ANN utilizes for connecting the PNMs of resolved and unresolved porosities. This network is trained between each pair of pores with the characteristics of both pores (pores coordination and pores diameter) to check if a throat should be added between them or not.

3.10 Multi-scale PNM Reconstruction

3.10.1 Statistical-MPR

Moslemipour and Sadeghnejad (2021) presented the statistical-MPR method for multi-scale PNM reconstruction. We use this method in our research to compare it with the ANN-MPR method. The workflow for this approach is shown in Figure 3-19. Figure 3-19a and c show the LR and HR images, respectively. First, the PNM is extracted from both LR (Figure 3-19b) and HR (Figure 3-19d) images. Then, as shown in Figure 3-19e, an equivalent stochastic PNM is generated from the HR image's PNM. In the unresolved porosity sections of the LR image, pores and throats remain on the stochastically generated PNM, while they are removed from the remaining parts (Figure 3-19f). However, the throats connecting removed pores to non-removed pores are retained to connect the PNMs. Next, the remaining pores in this stochastic PNM are merged with the PNM extracted from the LR image, which contains the coarse scale. To merge the networks, we use the throats that were retained to connect the small pores to the large pores surrounding them. The coordination number is ensured not to exceed the maximum value for the pores in the HR image PNM (Figure 3-19g). In this research, we use this method to reconstruct the multi-scale PNM in several different realizations to compare its accuracy with the ANN-MPR method. In these realizations, the PNM in the resolved porosity remains fixed, while a new PNM is generated for each realization in the unresolved porosity. We use the OpenPNM module in Python for PNM modeling [37].

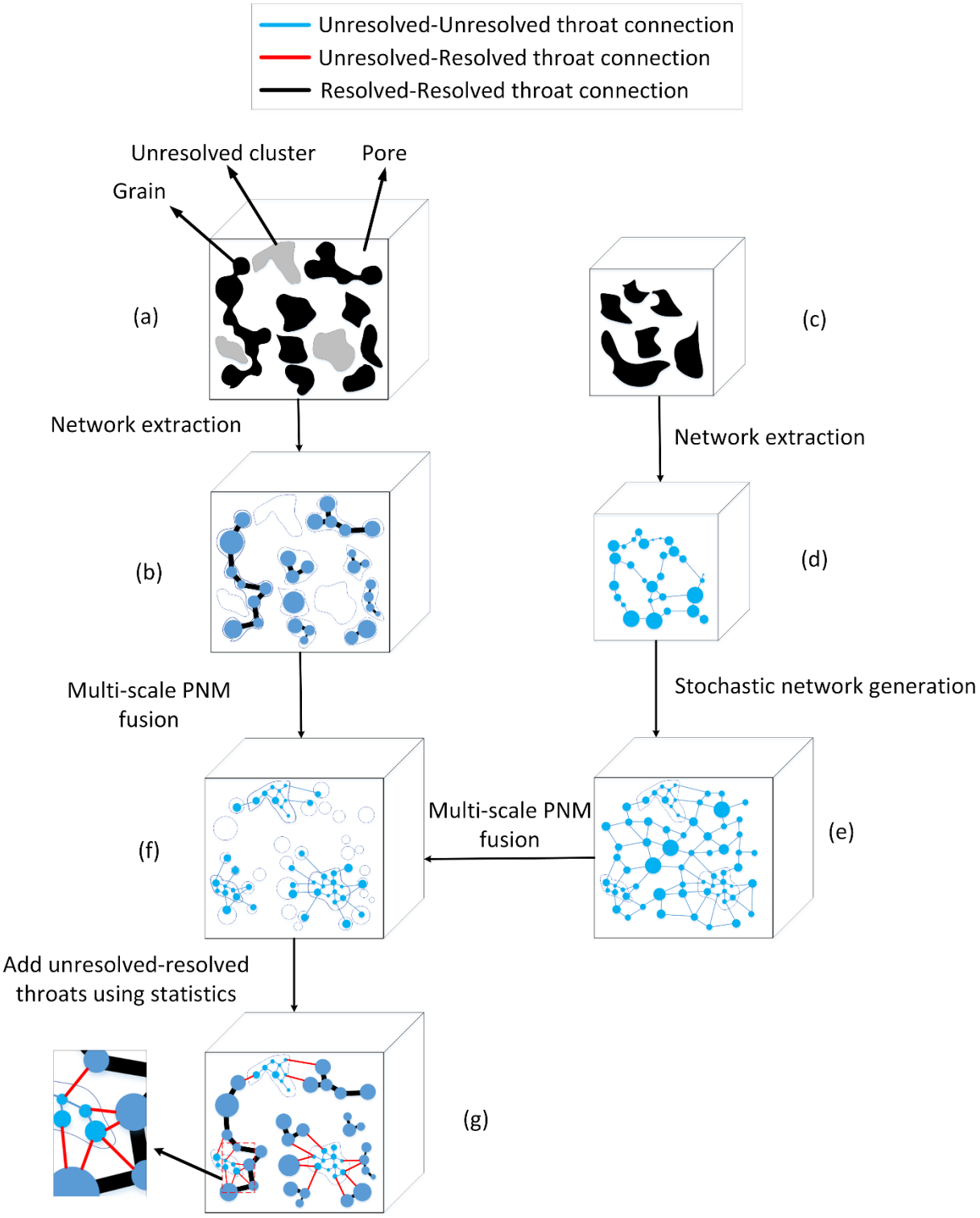

Figure 3-19 The schematic of statistical-MPR method for multi-scale PNM reconstruction. (a) Shows the LR image. (b) First, the PNM is extracted from the resolved area of the LR image. (c) Shows the HR image. (d) Another PNM is extracted from the HR image. (e) An equivalent stochastic PNM with the same size as the LR image is generated.

(f) The network extracted from the LR image and the stochastic network generated from the HR image are combined with each other. (g) The multi-scale PNM is reconstructed.

3.10.2 ANN-MPR

Figure 3-20a and c show the LR and HR images, respectively. Then, the PNMs are first extracted from the LR (Figure 3-20b) and HR (Figure 3-20d) images separately. To reconstruct multi-scale PNM using the ANN-MPR method, as shown in Figure 3-20e, we first generate different stochastic PNMs for each unresolved cluster based on the statistical properties of the PNM from the HR image. Therefore, these stochastic PNMs are replaced with unresolved clusters (Figure 3-20f). The main difference between the ANN-MPR and statistical-MPR methods lies in how they connect small and large pores, which are located in unresolved and resolved porosity, respectively. For this, an artificial neural network (ANN), trained on the PNM extracted from the HR image, is used. The ANN determines whether to add a connection (throat) between macro and micro pores and estimates the diameter and length of the added throats. As shown in Figure 3-20g, this connection links the micro-scale PNMs to the macro-scale PNM (unresolved-resolved) using the ANN. After the network is connected using the trained ANN model, the multi-scale PNM is reconstructed. To better assess the accuracy of our method, we generate several realizations of the multi-scale PNM. In these realizations, the resolved porosities are fixed, but new stochastic PNMs are generated for unresolved clusters in each realization. For each realization of the reconstructed multi-scale PNM, the properties are calculated separately. The accuracy of the reconstructed networks is then compared with those generated using the statistical-MPR method.

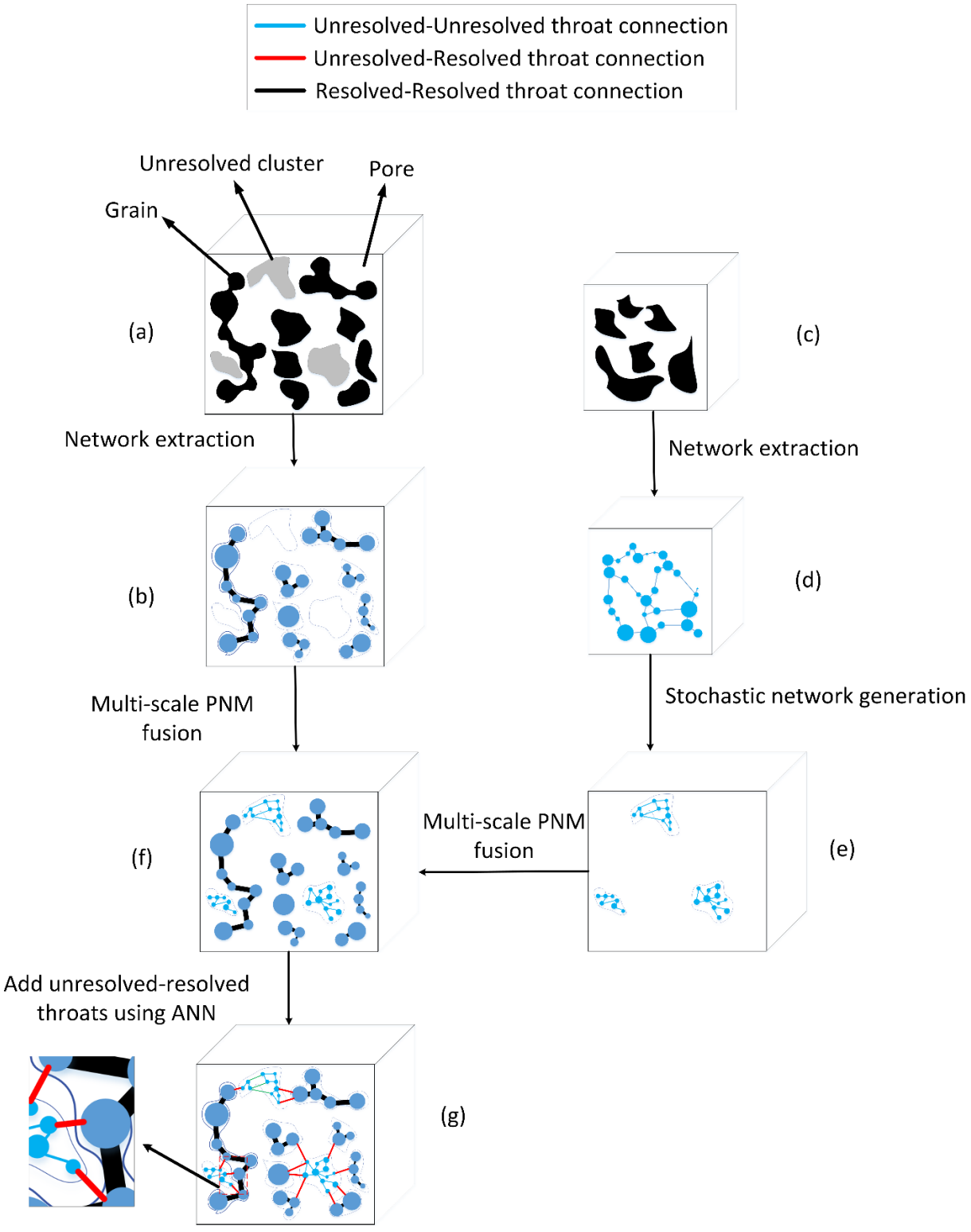

Figure 3-20 The schematic of ANN-MPR method for multi-scale PNM reconstruction. (a) Shows the LR image. (b) First, the PNM is extracted from the resolved area of the LR image. (c) Shows the HR image. (d) Another PNM is extracted from the HR image. (e) An equivalent stochastic PNM with the same size as the LR image is generated.

(f) The network extracted from the LR image and the stochastic network generated from the HR image are combined with each other. (g) The multi-scale PNM is reconstructed.

3.10.3 ANN-Octree-MPR

This method of multi-scale PNM reconstruction is introduced to further reduce memory consumption in the ANN-MPR method. To reconstruct the multi-scale PNM using this approach, the multi-scale image is first reconstructed using the OCWMR method. As described in the OCWMR method, templates are selected from the HR image for unresolved templates and clusters. In the next step, the PNM is extracted from each of these unresolved clusters, whose templates have been specified, using the SNOW method. Additionally, similar to the ANN-MPR method, the PNM of the resolved porosity is extracted separately from the LR image. In the following step, as in the ANN-MPR method, the PNM extracted from the unresolved clusters is connected to the PNM of the resolved porosity using an ANN. The only difference between the ANN-Octree-MPR and ANN-MPR methods is the different implementation of the PNM for the unresolved clusters. This reduces memory consumption because, in the ANN-MPR method, a stochastic equivalent PNM with a size equal to that of the LR image is required and placed in the unresolved porosity. Generating this equivalent stochastic network consumes more memory due to its large size. The schematic of the ANN-Octree-MPR method is shown in Figure 3-21.

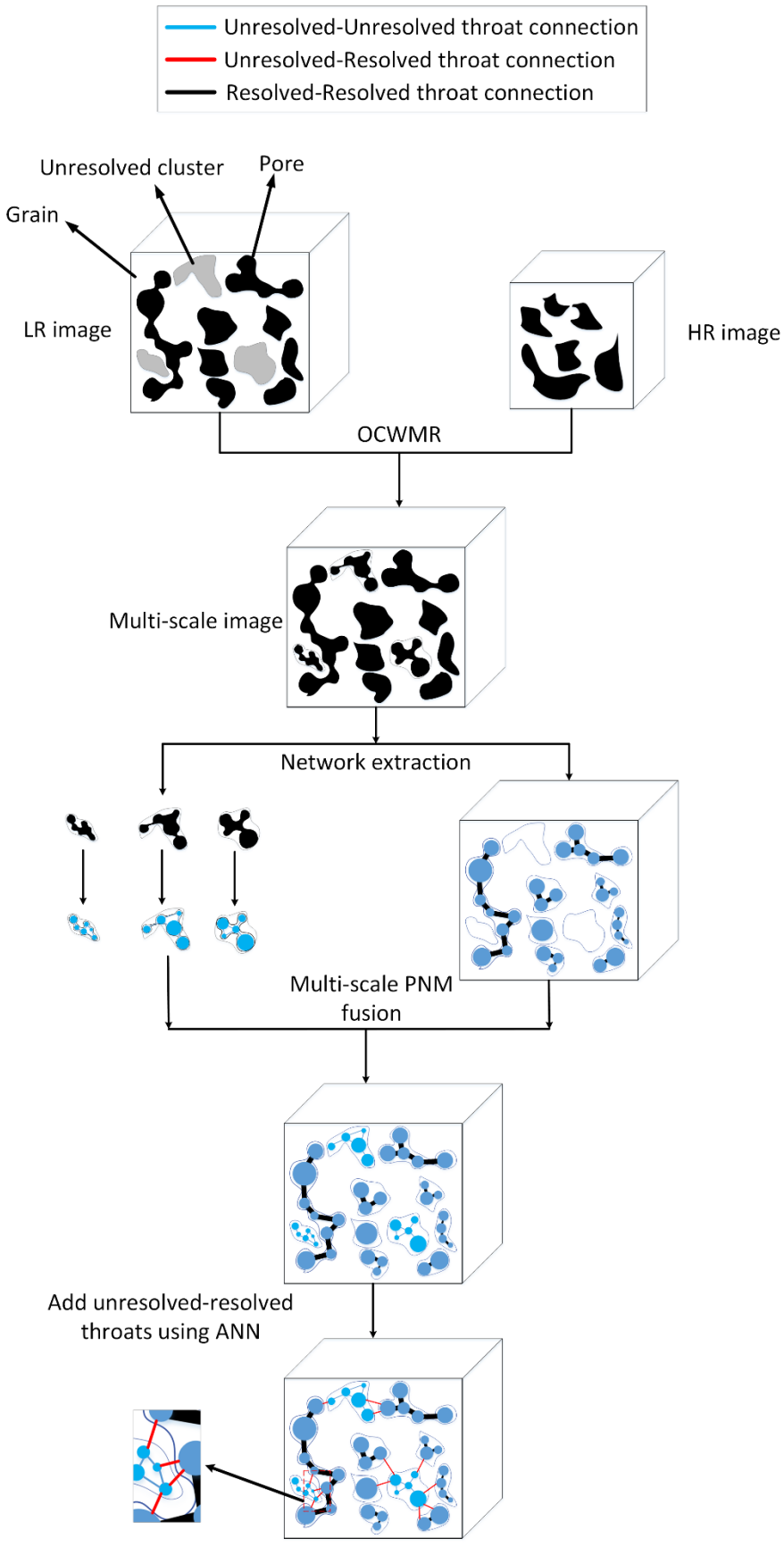
Unresolved-Unresolved throat connection
Unresolved-Resolved throat connection
Resolved-Resolved throat connection
Unresolved cluster
Pore
Grain
LR image
HR image
OCWMR
Multi-scale image
Network extraction
Multi-scale PNM fusion
Add unresolved-resolved throats using ANN

Figure 3-21 The schematic of ANN-Octree-MPR method for multi-scale PNM reconstruction. At first, using the OCWMR approach and using the Octree structure, a multi-scale image is created. This multi-scale image is reconstructed based on selected templates from the HR image and placing them in the unresolved porosity of the LR image. Next, the PNM is extracted from each of the unresolved clusters separately. The PNM is also extracted from the resolved porosity of the LR image. Next, the PNMs of resolved and unresolved porosity are connected to each other by adding throats. An ANN trained on the PNM extracted from the HR image is used to connect the pores in resolved and unresolved porosity. This network connects the pores to each other based on the diameter and coordinates, and finally the multi-scale PNM is reconstructed.

3.11 Multi-scale Modeling

After reconstructing multi-scale images and PNMs, it is necessary to model them to calculate various properties. Different methods can be employed for this purpose. For instance, properties can be calculated directly on the images by solving flow equations. However, due to the large size of multi-scale images, this approach often comes with a high computational cost. To address this issue, we present a new method for multi-scale modeling on images. A similar challenge exists in multi-scale PNM, where the large number of pores and throats complicates modeling and property calculations. This complexity requires powerful systems and results in long runtimes. To mitigate this, we introduce a new multi-scale PNM modeling approach that reduces the total number of pores and throats in the unresolved porosity sections, thereby lowering the computational cost of calculating properties on the multi-scale PNMs. In this method, a base pore is selected for each unresolved cluster based on the hydraulic conductance values of conduits in the PNM. New throats then connect this pore to the macro pores in the resolved porosity of the image, following the Hagen-Poiseuille equations.

3.11.1 Multi-scale DNS modeling

The reconstructed multi-scale images are often large, demanding substantial memory and runtime for permeability calculations. In this study, we propose a solution to this challenge by modeling on the octree structure. Instead of calculating permeability on a multi-scale image with small size voxels (MDNS-1), we perform calculations on an image structured with an octree structure. We tested our method on the BS rock sample. We named this method MDNS-2 method. We calculated the permeability of individual unresolved clusters with small voxel sizes. Then, to calculate the permeability of the whole image, we first set the permeability of the unresolved clusters separately

and computed the permeability of the entire image with the large voxel size using the GeoDict 2023 software package (Math2Market GmbH, Kaiserslautern, Germany).

In GeoDict 2023, the permeabilities of the unresolved porosity domains are calculated using the Brinkman term. Based on flow simulations on 3D HR images of the BS rock, isotropic permeabilities for each unresolved cluster were assigned to the microporous domains. Therefore, at first, we calculate the permeability value of each of the unresolved clusters in the LR image separately using the Navier-Stokes-Brinkman equation. Permeability calculation is performed on the templates selected from the HR image for each of the unresolved clusters. Finally, we place their permeability values separately in Geodict software and calculate the total permeability value on the image.

The schematic of permeability calculation using the mentioned method is shown in Figure 3-22. As shown in the image, at first, the LR image is segmented into three parts: pore, grain and unresolved porosity. In the next step (Figure 3-22b), the unresolved porosity is separateed in the image and identify the unresolved clusters according to Figure 3-22c using Watershed segmentation algorithm. Then, using the Geodict software and the Navier-Stokes-Brinkman equation, the permeability value is calculated for each of the unresolved clusters separately according to Figure 3-22d. Then the values of the calculated permeabilities are assigned in the LR image on the unresolved clusters separately. Finally, on the obtained structure, different properties can be directly calculated, including absolute permeabilities and relative permeabilities.

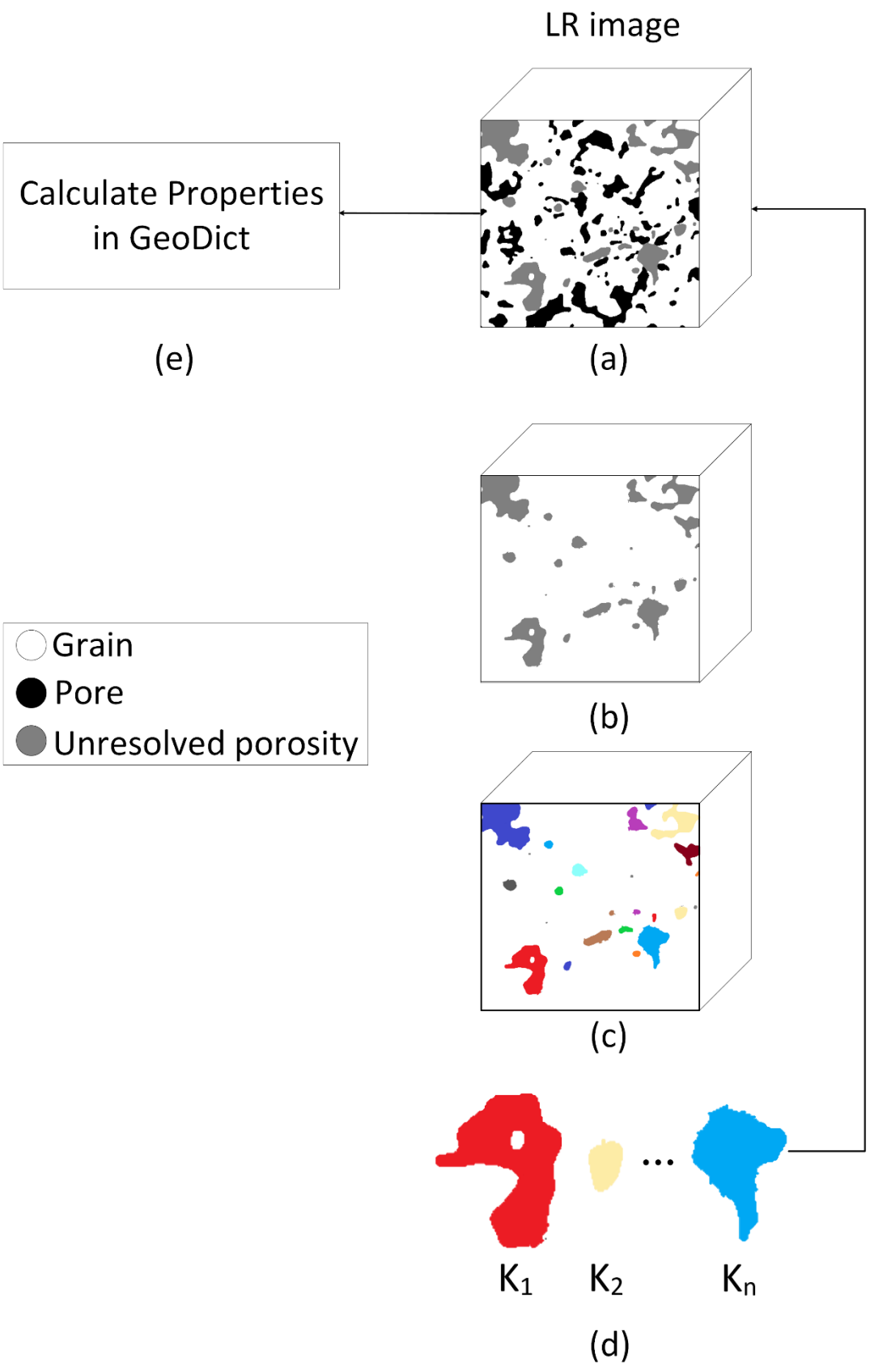
LR image
Calculate Properties in GeoDict
(e)
(a)
(b)
(c)
(d)
Grain
Pore
Unresolved porosity
Assing Permeability values
K1
K2
Kn

Figure 3-22 Multi-scale DNS modeling schematic. (a) The LR image is segmented into pore, grain, and unresolved porosity phases. (b) Unresolved porosity is separated in the image. (c) On isolated unresolved porosity, unresolved clusters are identified using watershed segmentation. (d) Permeability values in unresolved clusters are calculated separately using the Navier-Stokes-Brinkman equation. (e) Permeability values calculated on unresolved clusters are assigned on the LR image and the required properties are calculated using Geodict software.

The key point in these calculations is that the permeability of unresolved clusters is determined using selected templates from the HR image. These templates have a small voxel size, so permeability is calculated only on these templates with the smaller voxel size. However, the final properties, such as absolute and relative permeability and capillary pressure, are calculated on the LR image, which has a larger voxel size. As a result, the MDNS-2 method reduces both memory consumption and runtime. In this research, 10 different realizations of the multi-scale image were reconstructed for the BS rock sample using the OCWMR approach. Permeability was calculated directly on the small-size multi-scale image using the MDNS-1 method. We also calculated the permeability of these 10 realizations using the MDNS-2 method and compared the results with the permeability calculated on the small-size multi-scale image using MDNS-1. Furthermore, we selected the realization that showed the closest permeability values to the HR image and compared the relative permeability curve and capillary pressure of the MDNS-1 and MDNS-2 methods.

3.11.2 Multi-scale PNM modeling

After reconstructing the multi-scale PNM, it can be modeled directly using the openpnm module, allowing various properties to be calculated. This method is highly accurate, and we use it in this project to validate our own method, which is explained below. Calculating these properties on a large size PNM often has a high computational cost. The reason for this is that multi-scale PNM has large dimensions and contains a significant number of pores and throats. Modeling these many pores and throats requires substantial memory space and results in a high runtime. To address this issue, we developed a method that allows the reconstructed multi-scale PNM to be modeled with lower computational cost while maintaining sufficient accuracy. This method also enables the calculation of various properties on the network.

The schematic for the multi-scale PNM upscaling method is presented in Figure 3-23. This approach involves four key steps: selecting the base pore, identifying the shortest paths from the base pore to the resolved pores, calculating the equivalent hydraulic conductance along these paths,

and replacing the paths with new throats. This process is repeated for all unresolved clusters. Figure 3-24 provides a more detailed view of the upscaling stages. Each of these steps is explained in the following sections.

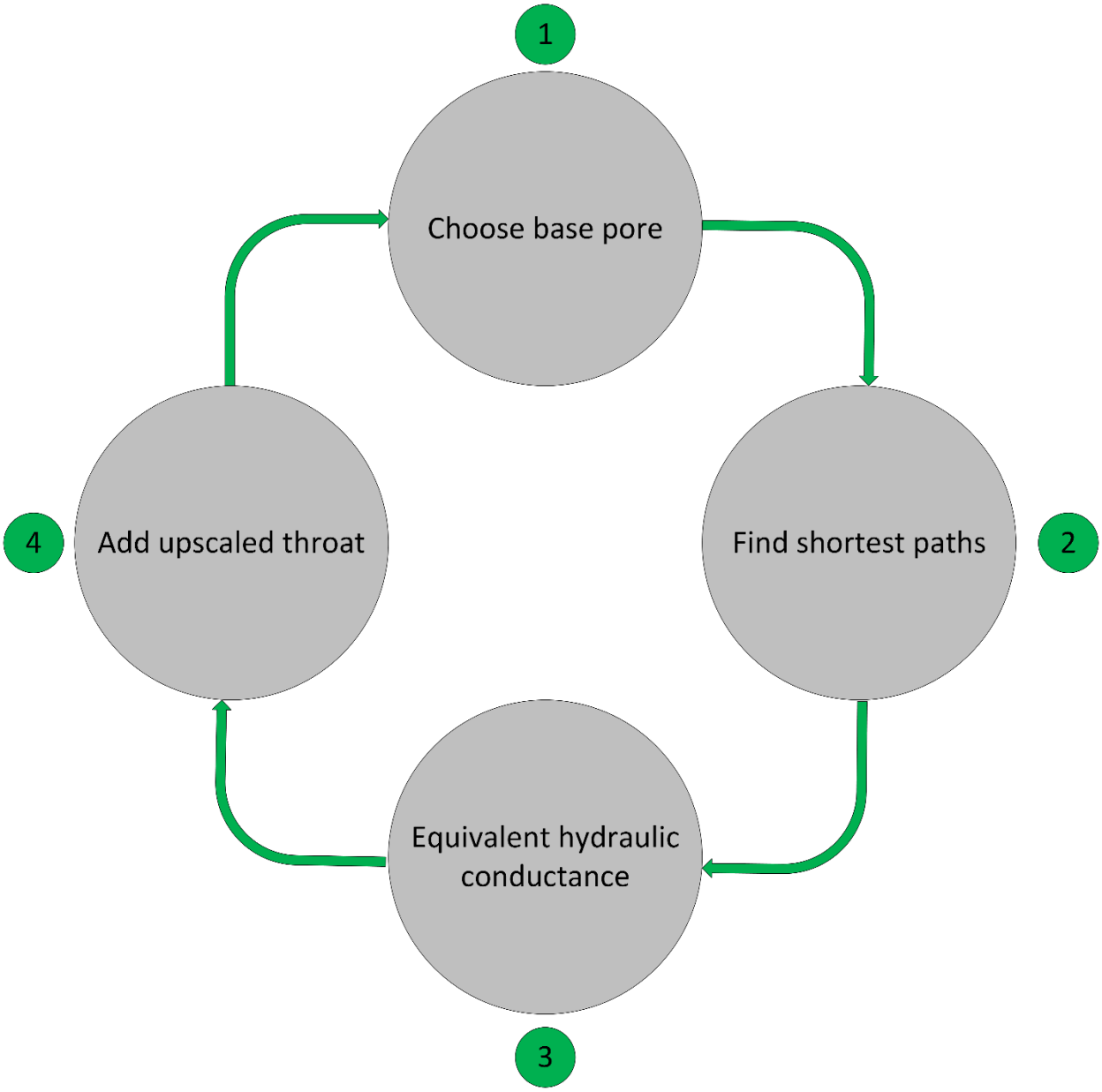

Figure 3-23 The schematic for the multi-scale PNM upscaling method. This approach involves four key steps for each unresolved cluster: (1) selecting the base pore. (2) identifying the shortest paths from the base pore to the adjacent resolved pores. (3) calculating the equivalent hydraulic conductance along these paths. (4) replacing the paths with new throats. This process is repeated for all unresolved clusters.

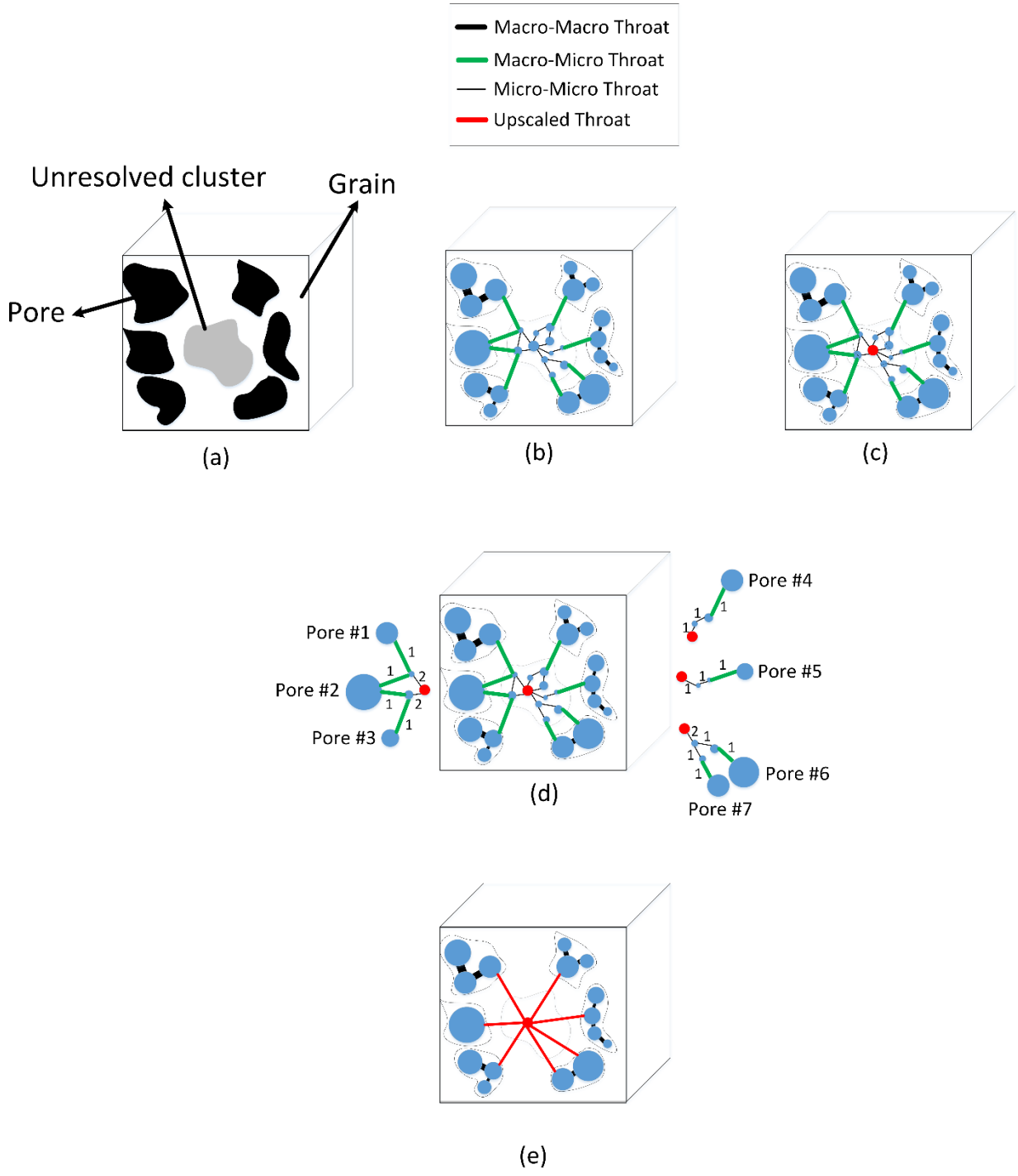

Figure 3-24 The workflow of multi-scale PNM upscaling method. (a) A section of LR image, which contains pore, grain and unresolved cluster. (b) PNMs are extracted from the pore phase and stochastically generated for the unresolved area. These PNMs are then connected to each other using the ANN. (c) The red pore with the highest hydraulic conductance of its neighbor conduits is selected as the base pore for this unresolved cluster. (d) Find the shortest paths between adjacent macropores and the base micro pore inside the unresolved cluster. This cluster is connected to seven macro pores. Pore #1 is connected to the unresolved cluster by one throat and therefore it has one

path to the base pore. Pores #3, #4, #5, #6 and #7 also are connected with one throat and therefore they have one path to the base pore. However, pore #2 is connected by two parallel throats to the unresolved cluster and therefore it has two paths to the base pore. Moreover, each throat in the paths has a weight, which specifies the number of times that throat is common in all paths. After finding the shortest paths, their equivalent hydraulic conductances are calculated. (e) This shows the upscaled network. The base pore just remained and other pore and throats inside the unresolved cluster are replaced by throats between the macro pores and the base pore.

As explained in Section 3.9, the PNM is first extracted from the unresolved clusters, and then an ANN is used to connect these regions to the PNM of the resolved part. For multi-scale PNM modeling, a base pore is considered for each unresolved cluster. All pores that were previously connected from the resolved part to the unresolved part are directly connected to the selected base pore using the ANN. In the next step, the equivalent hydraulic conductance for the new throats added between the pores in the resolved area and the selected base pore is calculated, based on the flow paths that existed between the resolved and unresolved porosity pores. The equivalent diameter for each of these throats is then determined by applying existing equations and solving them using the Newton-Raphson method. Finally, all pores in each unresolved cluster, except for the selected base pores, are deleted. Modeling is then performed on the obtained equivalent PNM. Due to the reduced number of pores and throats, this approach lowers the computational cost. In the following section, all these steps will be explained in more detail, along with the equations used in each step.

3.11.2.1 Base pore

As mentioned, it is necessary to consider a base pore for each unresolved cluster at the beginning. This base pore is selected based on the hydraulic conductance values of each pore. The hydraulic conductance in all conduits is calculated, and the pore with the highest hydraulic conductance in the conduits leading to it is chosen as the base pore. In the PNM, pores are modeled as spheres and throats as cylinders, with each conduit represented as ½ pore - total throat - ½ pore. Figure 3-25 illustrates a conduit in PNM. The length and diameter of the conduits are used to calculate hydraulic conductance in the PNMs. Therefore, in the first step, the length and diameter of each part of the conduit must be calculated. As shown in Figure 3-25(a), the throat length in the conduit is represented by L_t, while the lengths of the ½ pores are indicated as L_1 and L_2. Additionally, the distance between the centers of pore 1 and pore 2 is represented by the Euclidean distance (L_{clc}), as shown in equation 3-15. According to Figure 3-25(b), the diameters of the throat, first pore, and

second pore are denoted as D_t, D_1, and D_2, respectively. The formulas for calculating the lengths of the pores and the throat in each conduit are provided in equations 3-12 to 3-15.

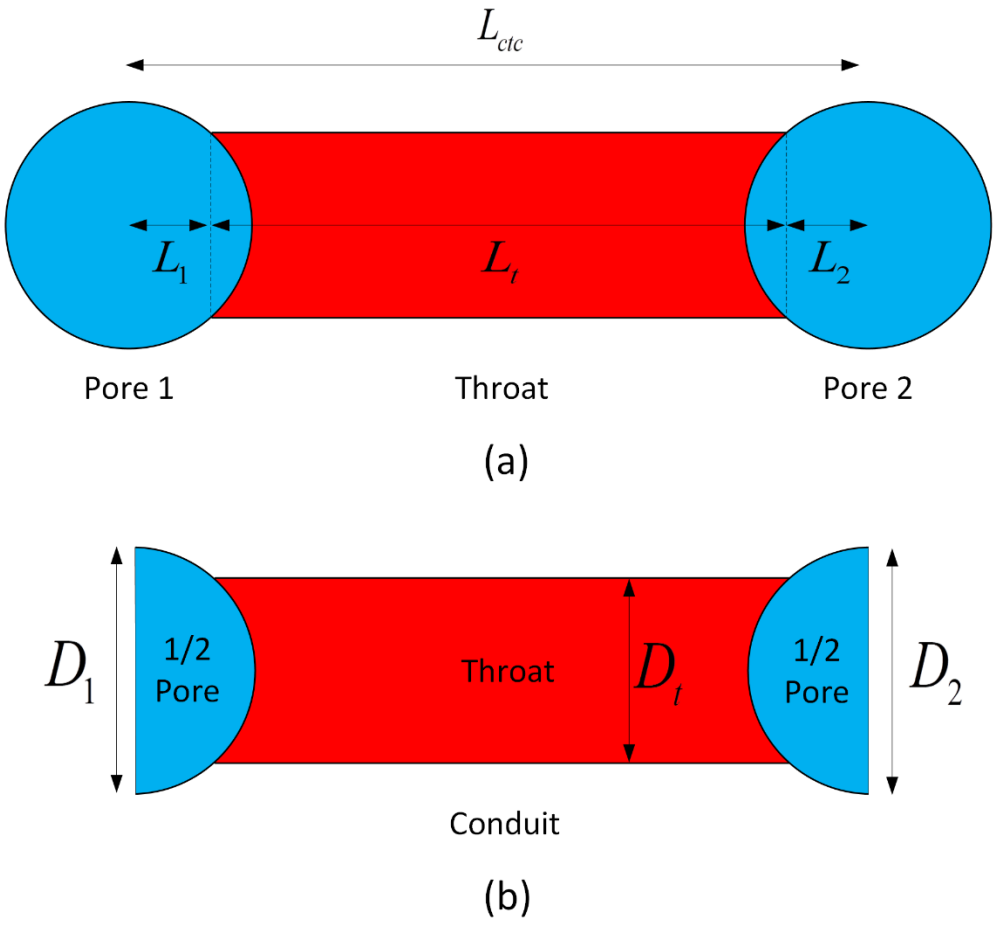

Figure 3-25 (a) A pair of pores and throats in an extracted PNM (b) A conduit consisting of 1/2 pore - full throat - 1/2 pore.

$$\left(\frac{D_1}{2}\right)^2 = L_1^2 + \left(\frac{D_t}{2}\right)^2 \Rightarrow L_1 = \frac{\sqrt{D_1^2 - D_t^2}}{2} \tag{3-12}$$

$$\left(\frac{D_2}{2}\right)^2 = L_2^2 + \left(\frac{D_t}{2}\right)^2 \Rightarrow L_2 = \frac{\sqrt{D_2^2 - D_t^2}}{2} \tag{3-13}$$

$$L_t = L_{ctc} - \left(L_1 + L_2\right) \tag{3-14}$$

$$L_{ctc} = \sqrt{\left(x_2 - x_1\right)^2 + \left(y_2 - y_1\right)^2 + \left(z_2 - z_1\right)^2} \tag{3-15}$$

After calculating the values of the length and diameter of the throats and pores in each conduit, the hydraulic conductance value in each conduit can be calculated separately using equation 3-16.

$$g = \frac{1}{\frac{1}{g_1} + \frac{1}{g_t} + \frac{1}{g_2}} \tag{3-16}$$

In this equation, g is the amount of hydraulic conductance in each conduit. Moreover, g_i is the amount of hydraulic conductance in each part of a conduit (½ pore - full throat - ½ pore). The g_i value is also calculated using equation 3-17 for each part of the conduit.

$$g_i = \frac{S_i}{\mu_i} \tag{3-17}$$

In this equation, μ_i is the viscosity of the fluid in each section of the conduit and S_i is the value of the size factor, which is also calculated for each section of the conduit separately using the equation 3-18.

$$S_i = \frac{1}{16\pi^2 I_i F_i} \tag{3-18}$$

In the above equation, two F_i and I_i terms are used to calculate the size factor value in each part of the conduit. To calculate the F_i value, the $A(x)$ value is used, which is given in equation 3-19.

$$F_i = \int_0^{L_i} \frac{1}{A(x)^2} dx \tag{3-19}$$

To calculate the F_i value for each ½ pore, the $A(x)$ value is defined in the form of equation 3-20.

$$A(x) = \pi r^2 = \pi \left(\sqrt{\left(\frac{D}{2}\right)^2 - x^2} \right)^2 = \pi \left((\frac{D^2}{4}) - x^2 \right) \tag{3-20}$$

By placing equation 3-20 in equation 3-19, according to equation 3-21, the F_i value for each ½ pore is calculated.

$$F_i = \frac{1}{\pi^2} \int_0^{L_i} \frac{1}{\left(\frac{D_i^2}{4} - x^2\right)^2} dx \xrightarrow{du=\frac{2}{D_i}dx} F_i = \frac{1}{\pi^2} \int_0^{\frac{2L_i}{D_i}} \frac{1}{\left(\frac{D_i^2}{4} - \left(\frac{D_i}{2}u\right)^2\right)^2} . \frac{D_i}{2} du \tag{3-21}$$

Now we have to calculate the integral according to equation 3-22.

$$F_i = \frac{8}{D_i^3 \pi^2} \int_0^{\frac{2L_i}{D_i}} \frac{1}{\left(1-u^2\right)^2} du = \frac{8}{D_i^3 \pi^2} \left(\frac{1}{2} \frac{u}{1-u^2} + \frac{1}{2} \arctan h\left(u\right) \right) \tag{3-22}$$

Now, to reach the final equation, we calculate the integral value from 0 to $\frac{2L_i}{D}$ for equation 3-22, and therefore, according to equation 3-23, the final value for F_i is obtained.

$$F_i = \frac{4}{D_i^3 \pi^2}\left(\frac{2D_i L_i}{D_i^2 - 4L_i^2} + \arctan h\left(\frac{2L_i}{D_i}\right)\right) \tag{3-23}$$

In addition, to calculate the F_i value for each throat, the $A(x)$ value is defined in the form of equation 3-24.

$$A(x) = \pi r^2 = \pi(\frac{D^2}{4}) \tag{3-24}$$

By placing equation 3-24 in equation 3-19, the F_i value for each throat is calculated according to equation 3-25.

$$F_i = \int_0^{L_i} \frac{1}{\left(\frac{\pi D_t^2}{4}\right)^2} dx = \frac{1}{\left(\frac{\pi D_t^2}{4}\right)^2} \int_0^{L_i} dx = \frac{L_t}{\left(\frac{\pi D_t^2}{4}\right)^2} \tag{3-25}$$

In addition, Equation 3-26 is used to calculate the I_i value.

$$I = \frac{\int_A \left(y^2 + z^2\right) dA}{A^2} \tag{3-26}$$

For both ½ pore and throat, we have equal circular cross-section and therefore, all sections in a conduit have same I value ($I_1 = I_t = I_2 = I$).Therefore, we use polar coordinates (r, θ) where

$y = r\cos(\theta)$ and $z = r\sin(\theta)$. The differential area element in polar coordinates is $dA = rdrd\theta$ .Therefore, in equation 3-27, we set up the integral using the mentioned assumptions.

$$I = \frac{\int_0^{2\pi}\int_0^{r}\left(r^2\right)rdrd\theta}{A^2} = \frac{\int_0^{2\pi}\frac{r^4}{4}d\theta}{A^2} = \frac{\frac{\pi r^4}{2}}{A^2} = \frac{\frac{\pi D^4}{32}}{A^2} \tag{3-27}$$

The area of the circular area is $A = \pi r^2 = \pi\left(\frac{D^2}{4}\right)$. Therefore, by replacing A into the equation 3-27, we will have the equation 3-28.

$$I = \frac{\frac{\pi D^4}{32}}{\left(\pi\left(\frac{D^2}{4}\right)\right)^2} = \frac{1}{2\pi} \tag{3-28}$$

Using these equations, the method of multi-scale PNM modeling can now be explained more clearly. As shown in Figure 3-24a, the image consists of three phases: pore, grain, and unresolved porosity. According to Figure 3-24b, the PNM is extracted from the resolved phase and generated stochastically for the unresolved clusters, which is explained in section 3.11. In the next step, the two scales are integrated using the ANN described in Section 3.9. For multi-scale PNM modeling, the hydraulic conductance values in the small pores within each unresolved cluster are first calculated separately. The pore with the highest input hydraulic conductance in each unresolved cluster is selected as the base pore for that cluster.

3.11.2.2 Shortest paths

In the next step, the shortest path to the base pore is identified for all adjacent macro pores connected to the unresolved cluster in the previous step. If a pore is connected to the unresolved cluster by two throats, the shortest path is determined for each throat separately. In Figure 3-24c, seven macro pores are shown as being connected to the unresolved cluster. Pore #1 is connected

to the unresolved cluster by one throat, and the shortest path for this pore is determined, consisting of two series throats. Pore #2 is connected to the unresolved cluster by two parallel throats, so one path is determined for pore #1 and another for pore #2, with each path also consisting of two series throats. Pore #3 is connected by one throat, and its path, similar to the others, contains two throats. The point to note is that the second throat in the path of pore #1 and the second throat in the first path of pore #2 are the same. Therefore, a weight of two is assigned to this throat, while the other throats take a weight of one for these two pores. Additionally, the second throat in the second path of pore #2 and the second throat in the path of pore #3 are also shared. Thus, this throat is assigned to a weight of two, while a weight of one is given to the remaining throats for these pores. These assigned weights will later be used to calculate the average hydraulic conductance. For pores #4 and #5, each is connected to the unresolved cluster by one throat, and the shortest path to the base pore is selected for both. As shown, the path for these two pores consists of three series throats, each with a weight of one, as no throats are shared between the paths. For pores #6 and #7, each is connected by one throat, and the shortest path to the base pore is selected for both. Their paths also consist of three series throats, but the third throat is shared between these two paths. Therefore, a weight of two is assigned to the third throat, and a weight of one is assigned to the other throats.

3.11.2.3 Equivalent hydraulic conductance

Next, the equivalent hydraulic conductance values for each of the paths must be calculated. The specified paths and the weights assigned to the throats in each path are used for this purpose. Equivakent hydraulic conductance of each path (g_{equ_path}) is determined using equation 3-29, taking into account that the throats are arranged in series along each path. In this equation, the equivalent hydraulic conductance of each conduit ($g_{conduit\_1}$) is divided by its assigned weight (w). The weight reflects the number of shared conduits among different paths, ensuring that the hydraulic conductance is not overestimated. The equivalent hydraulic conductance value for the paths is then used to calculate the equivalent hydraulic conductance for the upscaled throats.

$$\frac{I}{g_{equ\_path}} = \frac{1}{\frac{g_{conduit\_1}}{w_1}} + \frac{1}{\frac{g_{conduit\_2}}{w_2}} + \ldots + \frac{1}{\frac{g_{conduit\_n}}{w_n}} \tag{3-29}$$

Figure 3-26 illustrates the process of calculating hydraulic conductance for each path. In Figure 3-26a, the specified paths for pores #1, #2, and #3 are shown. Both pores #1 and #3 have paths consisting of two throats arranged in series. Therefore, the equivalent hydraulic conductance is calculated for these paths using equation 3-29. The hydraulic conductance in the second throat is divided by 2 for each, as this throat is shared between two different paths. For pore #2, there are two distinct paths to the base pore. First, the hydraulic conductance for each path is calculated using equation 3-29, and then the hydraulic conductances of the two paths are summed to obtain the final equivalent hydraulic conductance for the new throat. In Figures 3-26b and 3-26c, a pore is connected to the base pore by a single path. Each path consists of three throats, all with a weight of 1. Therefore, the equivalent hydraulic conductance for these paths is also calculated using equation 3-29. In Figure 3-26d, pores #6 and #7 are connected to the base pore by a single path, each consisting of three throats. However, the last throat is common to both paths and is assigned a weight of 2. The hydraulic conductance for these paths is also calculated using equation 3-29, and the conductance of the final throat in each path is divided by its weight, which is 2.

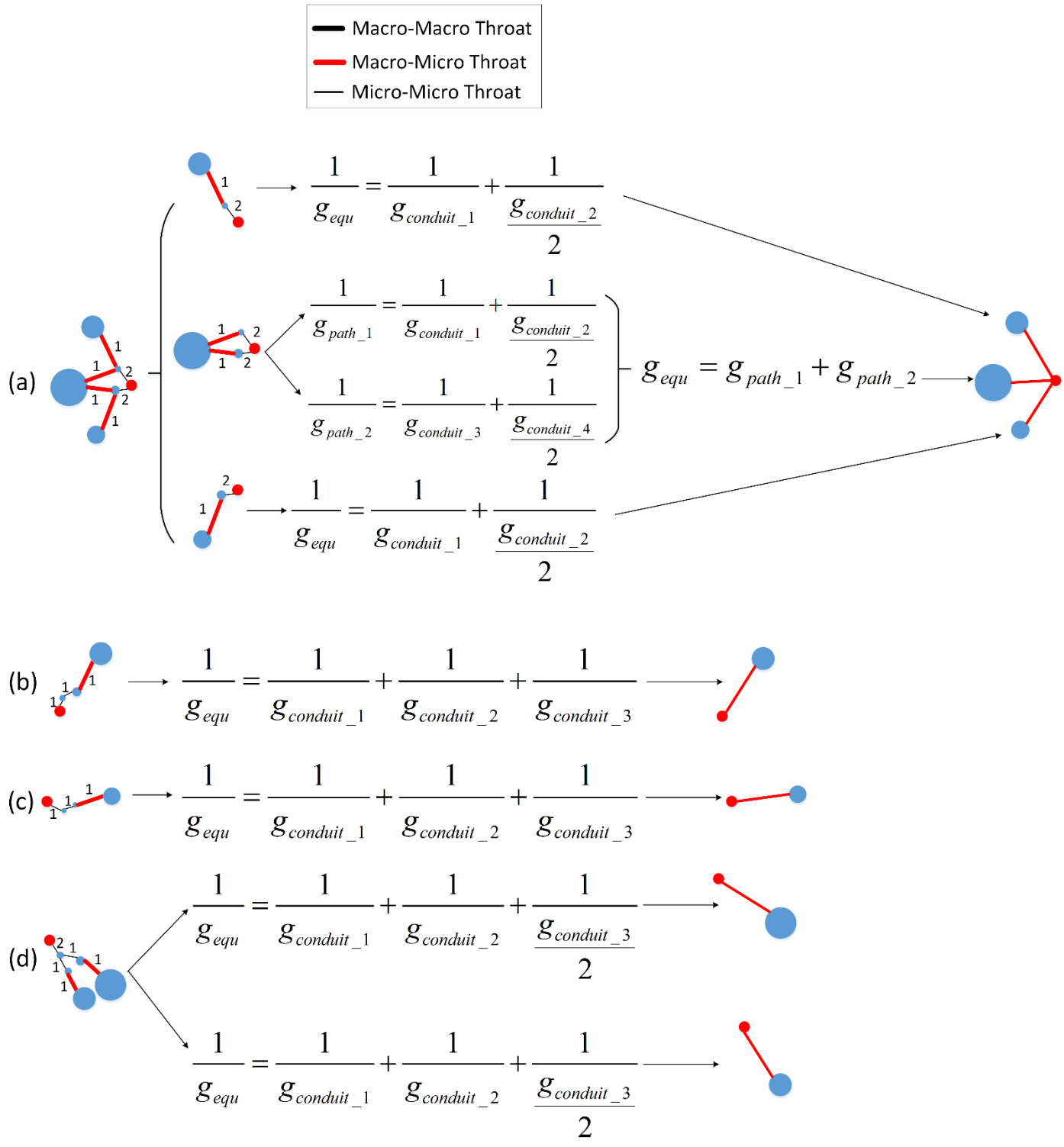

Figure 3-26 The procedure for computing the hydraulic conductance of each upscaled throat. (a) shows the specified paths for pores #1, #2, and #3 are shown. Both pores #1 and #3 have paths consisting of two throats arranged in series. Moreover, the hydraulic conductance in the second throat is divided by 2 for each, as this throat is shared between two different paths. For pore #2, there are two distinct paths to the base pore. First, the hydraulic

conductance for each path is calculated, and then the hydraulic conductance of the two paths is summed to obtain the final equivalent hydraulic conductance for the new throat. (b) and (c) show one pore which is connected to the base pore by a single path. Each path consists of three throats, all with a weight of 1. (d) shows pores #6 and #7 which are connected to the base pore by a single path, each consisting of three throats. However, the last throat is common to both paths and is assigned a weight of 2. The hydraulic conductance for these paths is also calculated, and the conductance of the final throat in each path is divided by its weight, which is 2.

3.11.2.4 Add upscaled throats

In Figure 3-24e, a single throat is added for each macropore, connecting the macro pore directly to the base pore. At this stage, all pores and throats within the PNM of the unresolved cluster are deleted, leaving only the base pore. For macro pores, like pore #2, which had more than one path to the base pore, only one throat should be added as well. Therefore, if a macropore has more than one path to the base pore, the equivalent hydraulic conductance (g_{equ}) is calculated by summing the equivalent conductance of each path, as outlined in Eq. 3. This approach accounts for multiple connections, ensuring accurate representation of hydraulic conductance.

$$g_{equ} = g_{equ\_path\_1} + g_{equ\_path\_2} + \ldots + g_{equ\_path\_n} \tag{3-30}$$

After the equivalent hydraulic conductance values for each of the upscaled throats have been calculated, the equivalent diameter and length for each throat must be determined. The equivalent length of each throat is equal to Euclidean distance between the macropore and base pore. Moreover, the equivalent diameter is based on the calculated equivalent hydraulic conductance values. Since the hydraulic conductance for each conduit is defined as ½ pore – full throat – ½ pore, equation 3-16 is used to compute the throat diameter. In this equation, all variables are known except for the upscaled throat diameter. The Newton-Raphson method is employed to find the throat equivalent diameter. Using equation 3-31, the root of the unknown variable is found according to the Newton-Raphson method.

$$D_{n+1} = D_n + \frac{f(D_n)}{f'(D_n)} \tag{3-31}$$

In the above equation, D_n is the value of the initial guess of diameter value and D_{n+1} is the diameter value of the new guess. Moreover, f is the $f = g_{equ} - \frac{1}{\frac{1}{g_1}+\frac{1}{g_t}+\frac{1}{g_2}}$ function, $f(D_n)$ is the value of the function in D_n and $f'(D_n)$ is the value of the derivative of the function in D_n. Therefore, after calculating the diameter of the upscaled throats, all the information of the upscaled multi-scale PNM is prepared and modeling can be done on it and various properties can be calculated on it.

3.12 PNM properties

To calculate the properties of the PNM, the openpnm module is used in Python programing language. This module has various equations to calculate the properties of the PNM. Moreover, after the multi-scale PNM reconstruction, it is necessary to calculate various properties on it. This section refers to the methods and equations used to calculate the properties of the reconstructed or extracted pore network, including porosity, absolute permeability, relative permeability, and capillary pressure.

3.12.1 Porosity

According to equation 3-32, in order to calculate the porosity of the PNM, dividing the total volume of all pores and throats to the total volume of the network.

$$\varphi = \frac{\sum V_p + \sum V_t}{L_x \times L_y \times L_z} \tag{3-32}$$

3.12.2 Permeability

To calculate the permeability of the network, it is used to establish the flow in three directions and calculate the flow rate by the Stokes flow equations. Stokes flow or creep flow is a flow model with a small Reynolds number (Re<<1) and viscous forces are the dominant forces in this type of flow. Therefore, in this type of flow, low velocity and high viscosity of the flow are observed due to the low Reynolds number. The Stokes flow equations, which are also known as the Stokes

equations, are obtained from the linearization of the Navier-Stokes equations. Internal forces are neglected in front of viscous forces, and therefore removing the internal parameters of the kinetic equilibrium in the Navier-Stokes equation causes the kinetic equilibrium to become the following form.

$$\nabla.P + f = 0 \tag{3-33}$$

In the above equation, P represents the pressures and f represents the forces on the surface.

Hydraulic conductance, which is also known as permeability coefficient, is defined as the flow volume efficiency in a material and is defined as the flow rate per unit of applied pressure. In addition, the length of the throat is equal to the distance between the centers of the two pores minus the sum of the radii of the two pores. The hydraulic conductance between two pores i and j is calculated by hagen Poiseuille equation (Equation 3-34) as follows.

$$g_{H,i-j} = g_{h,t} = \frac{\pi}{128}\left(\frac{D_t^4}{L_t}\right) \tag{3-34}$$

In the above equation, D_t and L_t indicate the volume and length of the throat, respectively. On the other hand, in order to calculate the flow rate between two pores, the following equation is used.

$$g_{i-j} = \frac{\pi}{128\mu}\left(\frac{D_t^4}{L_t}\right)\left(P_j - P_i\right) = g_{H,t}\Delta P_{i-j} \tag{3-35}$$

μ represents the viscosity of the fluid and P represents the pore pressure.

Then, the permeabilities in three directions are calculated using Darcy's equation and their average is reported as the final average. In the real geometry of rocks, pores and throats are not in the simple sphere and cylinder shape that we consider in our models. Therefore, in the built models, a

parameter should be considered that covers the sharpness and inhomogeneity in the pores and throats. The two image extraction methods used use two different methods to correct this issue.

The MB method takes into account the heterogeneity in pores and throats by considering the shape factor that depends on the schematic of the pore and throat (Figure 3-27) and is independent of the dimensions of the pore and throat. The shape factor has an effect on the hydraulic conductance of the pores and throats and changes the permeability value of the network, which is closer to the actual permeability value of the rock. The shape factor (G) is defined in the form of equation 3-36 and its related equations are also given below [153].

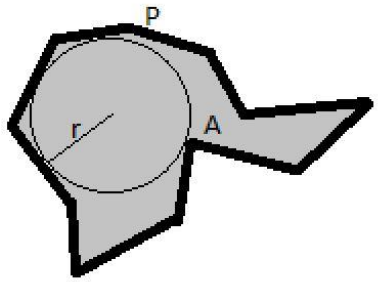

Figure 3-27 The form factor is defined as follows: G=A/P^2

$$G = \frac{A}{P^2} \tag{3-36}$$

$$q_{p,ij} = \frac{g_{p,ij}}{L_{ij}}\left(\phi_{p,i} - \phi_{p,j}\right) \tag{3-37}$$

$$\frac{L_{ij}}{g_{p,ij}} = \frac{L_i}{g_{p,i}} + \frac{L_t}{g_{p,t}} + \frac{L_j}{g_{p,j}} \tag{3-38}$$

$$g_p = k\frac{A^2G}{\mu_p} = \frac{1}{2}\frac{A^2G}{\mu_p} \tag{3-39}$$

L represents the length. i and j indicate the two pores connected to each other and t indicates the throat between these two pores. Moreover, "A" represents the cross-sectional area and μ_p represents the viscosity of fluid.

But the SNOW algorithm, unlike the MB method, uses equivalent diameters for pores and throats instead of the shape factor. The values of the equivalent diameter are greater than the surrounding diameter, and for this purpose, it is used to calculate the additional cross-sectional area for the flow. These values are used to calculate hydraulic conductiance so that the waste of pressure in the pores is ignored. This method uses the maximum distance map to calculate the surrounded diameter, but to calculate the equivalent diameter, it considers a circle whose area is the same as the cross-sectional area of the throat. Calculating the surface area of pores from images that include voxels is a difficult task. Calculating the number of voxels on the surface of a volume is an easy task, but how much of the surface it contains is not easy at all. Calculating the cross-sectional area of the throats is also a very difficult task, just like the cross-sectional area of the pores. But to calculate it, it is obtained by obtaining the number of voxels in a throat and multiplying it by the surface area of one voxel. The same equations (3-14) and (3-15) are used to calculate hydraulic conductance and permeability in this method [150].

3.12.3 Relative permeability

The process for calculating relative permeability on PNM involves some steps, starting from the initial pressure and continuing until the pressure corresponds to the irreducible saturation of the wetting phase. First, determine the boundary conditions, including flow direction and inlet and outlet pressures. Next, compute the hydraulic conductance of invaded throats. At each pressure step, update phase saturations using capillary pressure curve data. Execute the Stokes flow algorithm twice: once for the wetting phase and once for the non-wetting phase. Calculate relative permeability by dividing the effective permeability obtained from the Stokes flow by the absolute permeability. Increase the pressure and repeat the calculations starting from the phase saturation update step. As relative permeability is the ratio of effective over absolute permeability, given the

same boundary condition and viscosity, the geometrical parameters in K_r will cancel out. The remaining fraction includes flow rates as follows:

$$K_r = \frac{K_{eff}}{K_{abs}} = \frac{Q_{eff}}{Q_{abs}} \tag{3-40}$$

Where Q_{eff} is the inlet flow rate of the phase for a Stokes flow algorithm assigned as conduit hydraulic conductance model to account for the existence of the other phase. Whereas Q_{abs} is the inlet flow rate of the phase for a Stokes flow algorithm assigned as hydraulic conductance model for a single phase flow. Note that K_{abs} is a property of the porous material, not the fluid. However, here to cancel out viscosity in the K_r fraction, the same phase must be used to calculate Q_{abs}.

3.12.4 Capilary pressure

Ordinary percolation theory is used to model imbibition and drainage processes. This theory calculates the inlet pressure of pores and throats separately for each pore and throat using the wash-burn equation. Capillary pressure can be calculated by different methods. In this research, wash-burn equations are used to calculate the pressure entering the system from the bottlenecks. This method calculates the inlet pressure by considering the throats in the form of a cylinder. The wash-burn equation is defined as follows by considering the radius r for the throat, the surface tension σ and the contact angle between rock and fluid θ.

$$P_c = \frac{-2\sigma\cos\theta}{r} \tag{3-41}$$

3.13 DNS properties

It is also necessary to consider equations for calculating different properties directly on images so that different values such as porosity, absolute permeability, relative permeability and capillary pressure can be calculated on each image. For this purpose, we use GeoDict software, which

calculates various properties with high accuracy. In the following, the method and equations used in this software to calculate various properties are explained.

3.13.1 Porosity

Porosity is a measure to compute the total void space of a porous rock sample. The porosity of the multi-scale image is determined by dividing the number of pixels representing the pore phase by the total number of pixels (Equation 3-42).

$$\phi = \frac{N_p}{N_T} \tag{3-42}$$

In this equation, ϕ represents the porosity, N_p stands for the number of pixels in the pore phase, and N_T denotes the total number of pixels in the multi-scale image.

3.13.2 Absolute and relative permeability

Absolute and relative permeability are the fundamental properties of porous media that describe the capacity of a fluid to flow through a fully saturated medium. The medium's absolute permeability is determined by several rock and fluid properties, including the connected porosity, the size and connectivity of the pores and throats, the tortuosity (the degree of convolution of the flow path), and the fluid viscosity. These properties interact with each other in complex ways to determine the overall permeability of the medium. To describe the conservation of mass and momentum in such cases, the Navier-Stokes equations and the continuity equation were adopted. In this study, the software package GeoDict 2023 with adaptive meshing [154], was employed for solving these equations. The FlowDict module's Left-Identity-Right (LIR) solver was utilized [155]. The LIR solver employs LIR trees to optimize the efficiency of the flow solver and thus reduce computational costs. This technique involves coarsening pore spaces with minimal velocity variations while maintaining a fixed resolution for other pores. The simulations in this study maintained constant pressure differentials across the domains and imposed no-flow boundary conditions in the tangential directions. Moreover, on the surfaces of solids, the no-slip boundary condition is assumed ($\vec{u} = 0$). Equation 3-43 states that the divergence of the velocity field ($\vec{u}$) is

zero, implying that the fluid is incompressible meaning the volume of fluid elements does not change as they flow:

$$\nabla.\vec{u} = 0 \tag{3-43}$$

Equation 3-44 represents the conservation of momentum and describes how the velocity field changes over time. In this equation, $\vec{u}$ is the fluid flow velocity, p is the pressure, μ is the fluid viscosity , ρ is the fluid density, ∇ is the gradient operator, and $\vec{f}$ is the force density.

$$-\mu\Delta\vec{u} + \left(\rho\vec{u}.\nabla\right)\vec{u} + \nabla p = \vec{f} \tag{3-44}$$

Then, Darcy's law is used to compute the permeability of the images:

$$\vec{u} = -\frac{K}{\mu}\nabla p \tag{3-45}$$

As mentioned, relative permeability is another basic multiphase flow property used to describe the flow behavior of fluids in porous media. It is defined as the ratio of the effective permeability of each phase in the presence of multiple fluids to the absolute permeability of the medium. In a two-phase system, the relative permeability (kr_i) of phase *i* is given by:

$$Kr_i = \frac{K_{eff,i}}{K_{abs}} \tag{3-46}$$

where $K_{eff,i}$ is the effective permeability of phase *i* and K_{abs} is the absolute permeability of the medium. The relative permeability curve is typically plotted as a function of phase saturation, which is the ratio of the volume of a phase to the total pore volume of the porous medium.

The SatuDict module's LIR solver was utilized for relative permeability calculations. The same boundary conditions were used for the calculation of both absolute and relative permeability. Moreover, it is worth noting that we used water and air phases for computing the relative permeability values in each water saturation condition.

3.13.3 Capillary pressure

Capillary pressure is the pressure difference across the curved interface between two immiscible fluids in contact with each other in a small capillary tube or a porous material. The capillary pressure calculation is based on the Young-Laplace equation and is expressed in terms of wetting and non-wetting phase pressures as expressed by Equation 3-47 below:

$$\Delta P = P_{nw} - P_{w} = \frac{2\delta \operatorname{Cos}\theta}{r} \tag{3-47}$$

where ΔP_c is the capillary pressure (Pa), P_{nw} is the pressure in the non-wetting phase (Pa) and P_w is the pressure in the wetting phase (Pa). Moreover, δ is the interfacial tension between the two fluids (N/m), θ is the contact angle (degrees) between the fluid and the capillary wall, and r is the radius of the capillary (m).

As clarified by Equation 3-47, the capillary pressure in a reservoir is determined by various factors, including the interfacial tension (IFT) between two immiscible fluids, the contact angle between rock and fluid (θ), which is influenced by the wettability of the rock, and the pore radius (r), which is a microscopic property of the rock. Additionally, the water and air phases were considered for the computation of capillary pressure values at different water saturations. Furthermore, our simulation took into account the trapping of the wetting phase.

Chapter 4

Results and discussion

Results and discussion

4.1 Synopsis

In this chapter, HR and LR images are shown at the beginning after image processing in each step. Then, the results of multi-scale image reconstruction at each scale are checked with different methods and the accuracy of the reconstructed images is checked. Then, the reconstructed multi-scale PNM is examined, and the accuracy of the presented method is assessed. Finally, the accuracy of different methods for calculating properties on images and multi-scale PNM is analyzed. In each step, different data are used for validation, which will be explained below.

4.2 Image processing

In this section, the results of the image processing operations and the results of the methods described in chapter 3 are stated. At first, the cropped images of all three rocks are shown, and then the cropped images are shown after removing the noise. Then, due to the fact that multi-scale reconstruction methods require resampling in some cases, in the next step, the resampled images with different methods are displayed and also the results of sensitivity analysis are shown on them. In the last stage of image processing, segmented images are displayed for each rock separately.

4.2.1 Image cropping

The BS rock sample was scanned at 1.28 and 2.4 µm resolutions. These image scans were cropped to 1,000 × 1,000 × 1,000 and 400 × 400 × 400 voxels, respectively. In addition, the EBC rock sample was scanned at 1.49 and 10.88 µm resolutions. Then, the respective sizes of the cropped scans were 1,000 × 1,000 × 1,000 voxels and 187 × 187 × 187 voxels, respectively. Finally, the ILS rock sample was scanned at 3.9 and 10 µm resolutions and these scans were cropped to 1,000 × 1,000 × 1,000 voxels and 668 × 961 × 700 voxels, respectively.

4.2.2 De-noising

After cropping, all scans were de-noised using the non-local means method using the ImageJ version 1.52 software package [136]. Figure 4-1 shows both LR and HR images of the cropped de-noised scans of the BS and EBC rock samples, respectively.

As is clear from the figure, the non-local means filter performs better than the Gaussian and Median filters. The Gaussian filter causes image crystallization and Median filter reduces details in pores. Non-Local Means filter instead of using the information of nearby pixels (such as Gaussian and Median filters), uses pixels that are located throughout the image and are very similar to the desired pixel. This allows the non-local means filter to identify repetitive structures and similar patterns in the image and reduce noise based on the whole image information. Moreover, in the non-local means filter, each pixel receives a weight that is determined based on its similarity to the target pixel. Pixels that are more similar to the target pixel get more weight. This method causes the noise to be reduced more effectively, because only the pixels with true similarity will be effective in removing the noise.

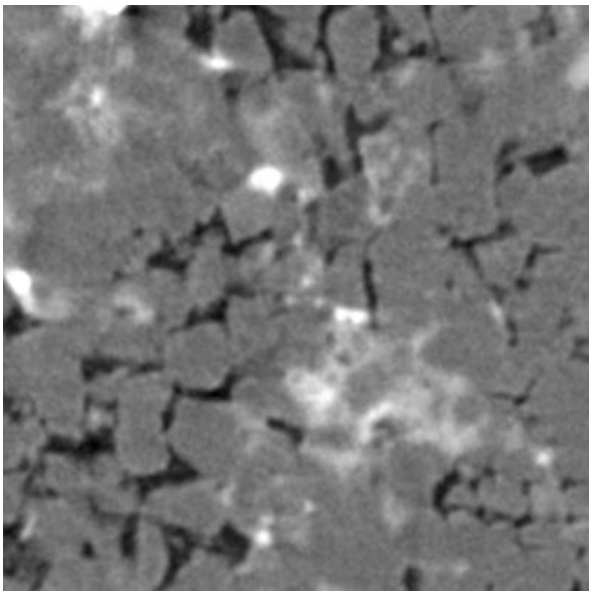

(a)

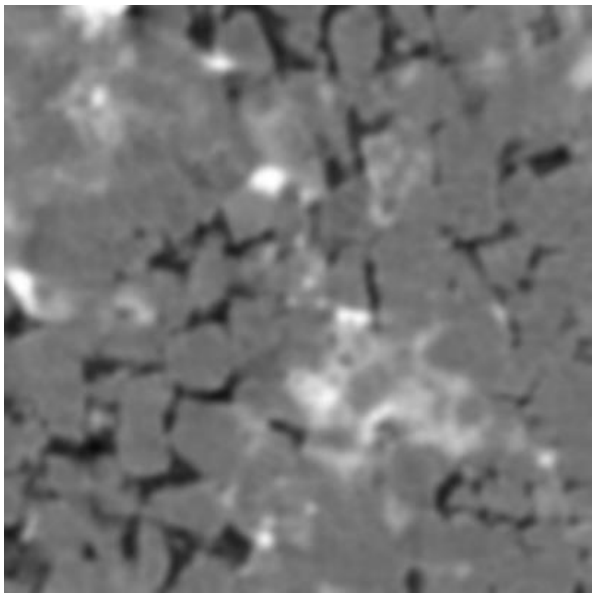

(b)

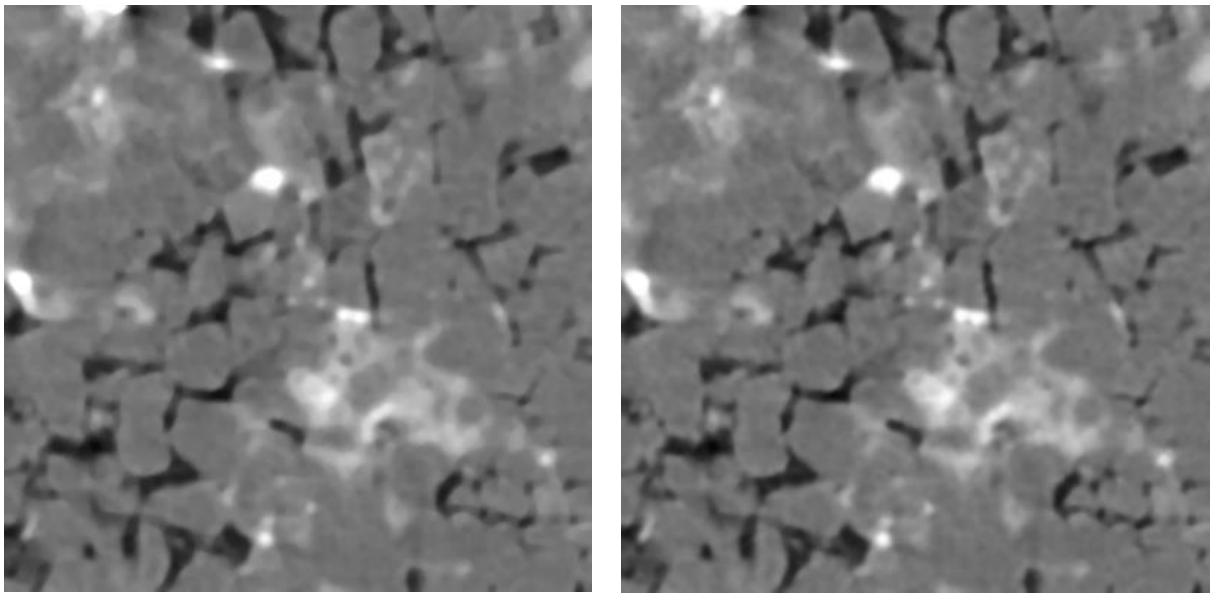

(c) (d)

Figure 4-1 (a) One 2D LR image of the BS rock sample after de-noising usimg (b) Gaussian filter (c) Median filter and (d) Non-local means filter.

4.2.3 Image resampling

First, the pixel size of the LR scans was resized to have a ratio of 2^n of the pixel size of the HR scans. In other words, the pixel size of the HR scan should become 2^n times (n is an integer number) finer than that of the LR scan.

For this purpose, the LR scan pixel size of BS, EBC and ILS were resampled from 2.4, 10.88 and 10 µm to 2.56, 11.92 and 7.8 µm, respectively. The pixel size of HR scans becomes 2 ($2.56\mu m = 2\times 1.28\mu m$), 8 ($11.92\mu m = 2^3 \times 1.49\mu m$) and 2 ($7.8\mu m = 2\times 3.9\mu m$) times finer than the pixel size of the LR scans, respectively. Therefore, the LR scan of the BS rock sample was converted from the size of 400 × 400 × 400 voxels to the size of 375 × 375 × 375 voxels. Moreover, the LR scan of the EBC rock sample was converted from the size of 187 × 187 × 187 voxels to the size of 170 × 170 × 170 voxels. Finally, the LR scan of the ILS rock sample was converted from the size of 400 × 400 × 400 voxels to the size of 513 × 513 × 513 voxels.

The Bi-cubic method for image resampling can preserve more details and produce smoother edges due to the use of a cubic function to combine adjacent pixel values. This method is more accurate

than Bi-linear, which only uses a linear function and four adjacent pixels and avoids artifacts such as blocking. Moreover, compared to Lanczos method, Bi-cubic is computationally simpler and less prone to ringing artifacts, which can be problematic at sharp edges or high-contrast regions in images. As a result, Bi-cubic offers an optimal balance between image quality and computational complexity, making it a superior choice for many image processing applications.

To fuse the scans, the pixel size of the LR scan had to be resampled 2^n smaller. This resampling process was applied by the nearest neighbour interpolation method. This method has a minimal effect on scan properties since each voxel is divided into eight equal sub grids at each step, where n represents the number of division stages. Consequently, this approach made the pixel sizes of the LR and HR scans equal. The LR scan of the BS rock sample was converted from the size of 375 × 375 × 375 voxels and a resolution of 2.56 μm to the size of 750 × 750 × 750 voxels and a resolution of 1.28 μm ($2.56 = 1.28 \times 2^1 \Rightarrow n = 1$). Moreover, the LR scan of the EBC rock sample was converted from the size of 170 × 170 × 170 voxels and a resolution of 11.92 μm to the size of 1,360 × 1,360 × 1,360 voxels and a resolution of 1.49 μm ($11.92 = 1.49 \times 2^3 \Rightarrow n = 3$). Finally, the LR scan of the ILS rock sample was converted from the size of 513 × 513 × 513 voxels and a resolution of 7.8 μm to the size of 1,026 × 1,026 × 1,026 voxels and a resolution of 3.9 μm ($7.8 = 3.9 \times 2^1 \Rightarrow n = 1$).

Table 4-1 BS rock sample

Property		Bi-cubic	Bi-Linear	Lanczos
Porosity (%)	Before	12.9	12.9	12.9
	After	12.9	12.8	12.9
Permeability (md)	Before	174	174	174
	After	171	166	170

Table 4-2 EBC rock sample

Property		Bi-cubic	Bi-Linear	Lanczos
Porosity (%)	Before	21.0	21.0	21.0
	After	21.0	20.8	20.9

Permeability (md)	Before	95	95	95
	After	94	79	89

Table 4-3 ILS rock sample

Property		Bi-cubic	Bi-Linear	Lanczos
Porosity (%)	Before	8.24	8.24	8.24
	After	8.25	8.28	8.26
Permeability (md)	Before	139	139	139
	After	143	148	145

The nearest neighbour interpolation method is particularly well-suited for this scenario because it effectively preserves the original characteristics of the LR scan while resampling to match the HR scan's pixel size. This method is computationally efficient, making it ideal for processing large 3D datasets without introducing significant distortions or artifacts. By simply mapping each voxel to its nearest neighbour, it ensures that the critical features and boundaries within the scan remain intact, which is crucial when dealing with complex structures like those found in rock samples. Moreover, since nearest neighbour does not smooth or alter the data like more complex interpolation methods, it maintains the integrity of the original scan's properties, ensuring that the fusion of LR and HR scans is accurate and reliable.

Table 4-4 Nearest neighbor resampling method

Property		BS	EBC	ILS
Porosity (%)	Before	12.9	21.0	8.25
	After	12.9	21.0	8.25
Permeability (md)	Before	171	94	143
	After	170	94	141

4.2.4 Image segmentation

In principle, the approach in this study involves two segmentation steps: HR image segmentation and LR image multi-phase segmentation. Table 4-5 summarizes the porosity and permeability values derived from these images. The first step is a two-phase segmentation of the HR images, dividing them into pore and grain phases (Figure 4-2a and Figure 4-2b). The calculated porosity of the BS rock sample in the HR images was 13.7% and of the EBC rock sample 28.2%, and of the ILS rock sample 9.0%, respectively. The second step involved multi-phase segmentation of the LR images (Figure 4-2c and Figure 4-2d). In the LR images of the BS rock sample, the porosity of the pore and unresolved sections was 12.9% and 9.3%, respectively. For the EBC rock sample, these values were 21.0% and 22.6%, respectively. Moreover, for the ILS rock sample, the porosity of the pore and unresolved sections was 8.25% and 6.0%, respectively. EBC rock showed a higher porosity in the unresolved phase due to the greater resolution difference between the LR and HR images. This difference resulted in a larger porosity discrepancy between the HR and LR images for the EBC rock (7.2%) compared to the BS rock (0.8%) and ILS rock sample (2.25%). In the EBC rock, the HR image had a permeability of 160 mD, while the LR image had a lower permeability of 94 mD. This indicates that the macro-pores in the LR image had lower connectivity because many connections with micro-pores were classified as unresolved porosity. For the BS rock, the smaller resolution difference between the LR and HR images resulted in less unresolved porosity (9.3%) and better connectivity between macro- and micro-pores. The HR image had a permeability of 147 mD, and the LR image showed higher permeability (170 mD) due to a wide range of larger pores. Like the EBC rock sample, in the ILS rock sample, the HR image had a permeability of 271 mD, while the LR image had a lower permeability of 141 mD. Segmented LR and HR images for all rocks are shown in Figure 4-2.

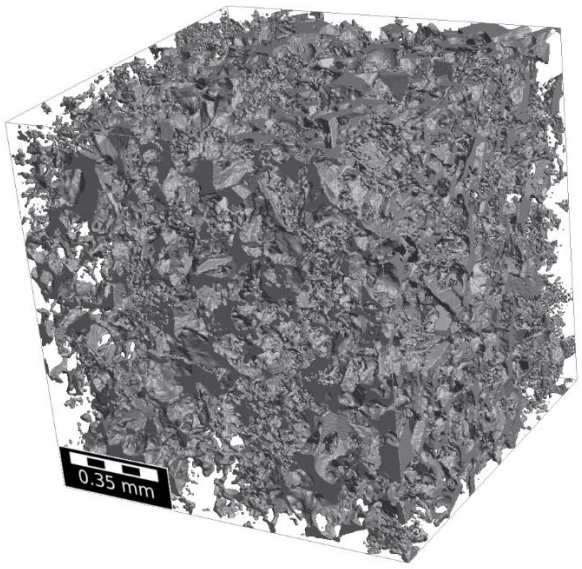

(a)

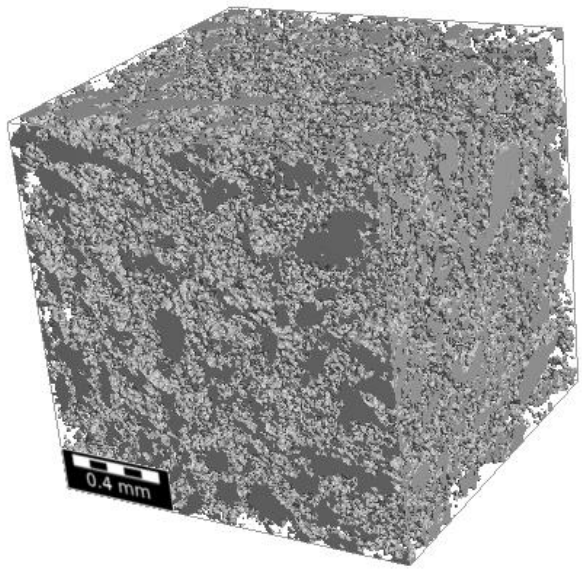

(b)

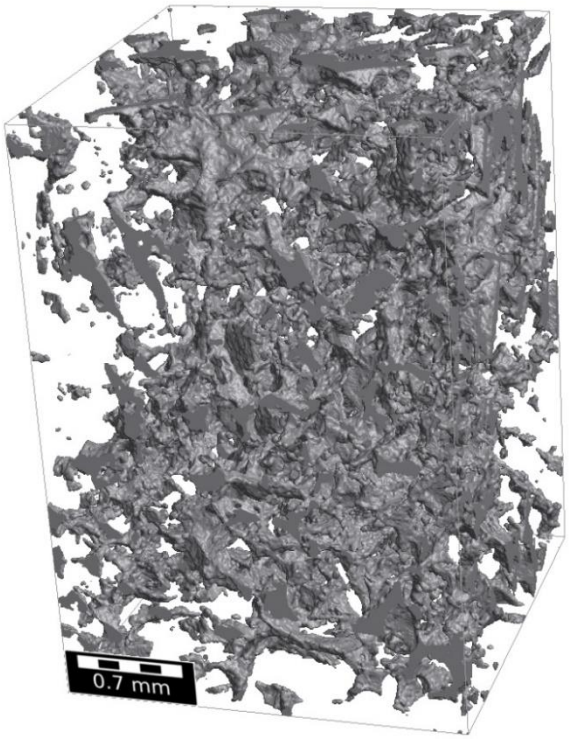

(c)

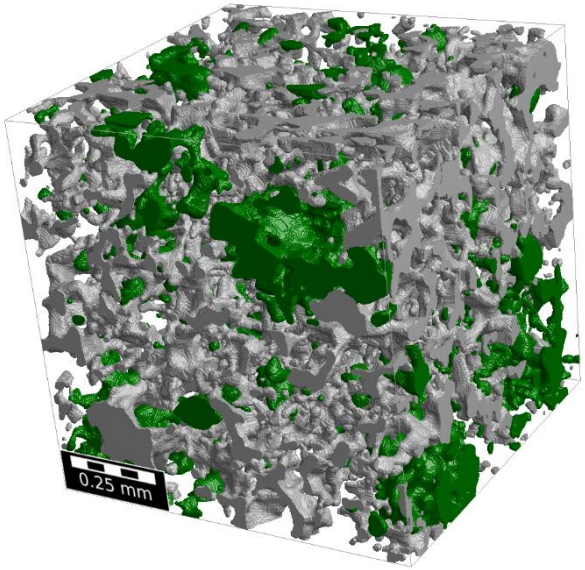

(d)

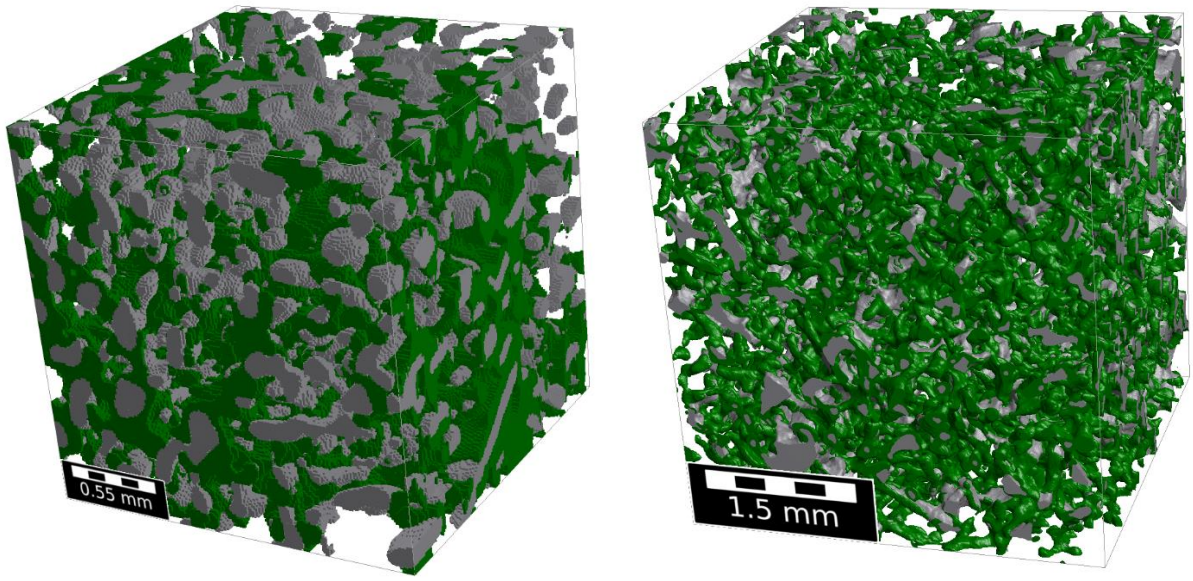

(e) (f)

Figure 4-2 Segmentation of the HR scan for the (a) BS, (b) EBC and (c) ILS rock samples, along with multi-phase segmentation of the LR scan for the (d) BS, (e) EBC and (f) ILS rock samples. The green colour pixels in the three bottom images show the unresolved porosity.

Table 4-5 Porosity and permeability of the BS, EBC and ILS rock samples for both LR and HR scans after applying the segmentation

			BS	**EBC**	**ILS**
Total Porosity (%)	HR image		13.7	28.2	9.0
Total / Unresolved Porosity (%)	LR image		12.9 / 9.3	21.0 / 22.6	8.25 / 6.00
Permeability (mD)	HR image	X-direction	115	189	295
		Y-direction	91	98	219
		Z-direction	235	194	299
		average	147	160	271
	LR image	X-direction	100	0	138
		Y-direction	71	0	165
		Z-direction	338	280	120
		average	170	94	141

4.3 Watershed segmentation

4.3.1 CWMR

The watershed algorithm partitioned the unresolved porosities of the LR images into smaller regions. This step reduces memory allocation and facilitates the fusion of HR images into LR images. The watershed method identified unresolved templates in the LR image. Some templates were distinct, while others were connected, allowing the determination of unresolved clusters. The unresolved templates and regions for each rock sample were then calculated.

Table 4-6 Unresolved porosity data before and after the watershed algorithm. The number of unresolved templates and unresolved regions is presented for both the BS and EBC rock samples, and the dimensions of the largest one for each unresolved template and unresolved region are provided.

Sample	Numbers of		Largest dimensions (voxels)					
	Unresolved templates	Unresolved regions	Unresolved templates			Unresolved regions		
			Width	Height	Depth	Width	Height	Depth
BS	1,797	488	176	152	140	648	726	760
EBC	2,080	212	360	584	168	876	964	772

Table 4-6 shows the number of unresolved regions and masks after applying the watershed segmentation. The EBC rock had 2,080 unresolved templates, more than the 1,797 found in the BS rock. However, the EBC rock had fewer unresolved regions (212) compared to the BS rock (488). This indicates that the watershed algorithm divided the unresolved porosity into larger sections in the EBC rock, and both unresolved templates and regions in the LR images of this rock were more connected.

Additionally, in the BS rock, the number of unresolved templates (1,797) is approximately 3.6 times higher than the number of unresolved regions (488). In the EBC rock, the number of unresolved templates (2,080) is about 9.8 times higher than the number of unresolved regions (212). This discrepancy likely results from the abundance of unresolved sections in the EBC rock at the boundary of resolved porosity. Each unresolved section around a macro-pore can be subdivided into numerous unresolved templates. Figure 4-2d appears mostly green for two reasons. First, the EBC rock has more unresolved porosity due to the significant resolution difference

between LR and HR images. Second, more unresolved voxels are located around the boundaries in the EBC rock image. Table 4-6 shows that the dimensions of the largest unresolved region are greater than those of the largest unresolved template in both rocks. This implies that in the modified Wu et al. method, the required HR image to select unresolved regions must be larger in each dimension compared to the CWMR approach. This difference can significantly impact computational cost and memory consumption, making the CWMR approach more efficient. The following sections will discuss the analysis based on the results presented in Table 4-6 in more detail.

4.3.2 OCWMR

In OCWMR, the optimized watershed algorithm was used to partition unresolved porosity phase in the LR image into smaller regions. Unlike the CWMR approach, the watershed algorithm was performed on the LR image with a large pixel size, so we expect that the number of unresolved templates will be different compared to the CWMR approach and have also different sizes for the Gaussian filter sigma as well as the maximum filter spherical radius (r_{max}). According to Moslemipour, Sadeghnejad [156], we reconstructed multi-scale images by CWMR with sigma = 0.4 and r_{max} = 4 for both rocks, of which porosity and permeability values are summarized in Table 4-7.

Table 4-7 Porosity and permeability of multi-scale reconstructed images using CWMR with sigma = 0.4 and r_{max} = 4 for the BS and the EBC rock samples

CWMR	Porosity (%)	Permeability (mD)
BS	14.3	141
EBC	27.3	165

To reconstruct more accurate images in the OCWMR approach, we first performed a sensitivity analysis on the porosity and permeability for both rocks on the sigma and r_{max} parameters. Table 4-8 summarizes the results of this sensitivity analysis. By comparing the porosity and permeability of multi-scale reconstructed images via the OCWMR with that of the HR image properties (13.7 % and 147 mD for the BS rock, and 28.2 % and 160 mD for the EBC rock, respectively), it can be concluded that the multi-scale reconstructed images for both rocks with sigma = 0.3 and r_{max} = 3

represent the best match with properties closest to that of the HR image (13.9 % and 147 mD for the BS rock, and 27.6 % and 161 mD for the EBC rock, respectively). These values are more like that of the HR image than the OCWR predictions (summarized in Table 4-7).

It is worth mentioning that the unresolved porosity should not be divided into too many (sigma = 0.1, r_{max} = 1) or too few segments (sigma = 0.7, r_{max} = 7). If they are divided into too many segments, it will cause the selected templates to become very small and the unresolved templates in LR images will not be adequately replaced. On the other hand, if they are divided into too few segments, it will cause the selected templates to not become the best-match templates for the desired template in LR images. This is due to the little overlap in OL compared to the size of the templates, and it causes larger pores to be included in the reconstructed image and have a weak connectivity between the added pores. Therefore, we will consider sigma = 0.3 and r_{max} = 3 parameters for further computation using the OCWMR.

Table 4-8 Sensitivity analysis on sigma and r_{max} parameters of watershed segmentation method by calculating porosity and permeability in multi-scale images reconstructed by OCWMR

Sigma / r_{max}	**BS**		**EBC**	
	Porosity (%)	Permeability (mD)	Porosity (%)	Permeability (mD)
0.1 / 1	14.6	122	28.1	176
0.2 / 2	14.4	136	27.9	169
0.3 / 3	**13.9**	**147**	**27.6**	**161**
0.4 / 4	14.1	150	27.5	157
0.5 / 5	14.3	159	27.7	142
0.6 / 6	14.4	162	28.2	135
0.7 / 7	14.6	164	28.5	128

The number of unresolved templates could have a significant effect on the connectivity created in the multi-scale reconstructed images. As it was mentioned, their optimal number can cause more suitable templates to be selected with an appropriate number of micropores. The number of unresolved templates after applying the watershed algorithm by CWMR with sigma = 0.4 and r_{max}

= 4 and OCWMR with sigma = 0.3 and r_{max} = 3 is shown in Table 4-9. As evident from this table, the OCWMR approach exhibits a lower number of unresolved templates. This is due to the larger pixel size in the LR image compared to the CWMR approach, resulting in the division of the unresolved phase into larger sections and subsequently reducing the number of unresolved templates.

One key aspect to consider when comparing the OCWMR and CWMR approaches is resampling. In the OCWMR approach, resampling is not performed on the LR image and reconstruction is carried out on the Octree structure. On the other hand, the CWMR approach involves resampling, which can cause some changes in the properties of the LR image.

Table 4-9 The number of unresolved templates for both BS and EBC rock samples after watershed segmentation using CWMR and OCWMR approaches

Sample	Numbers of unresolved templates	
	CWMR	OCWMR
BS	1,797	1,424
EBC	2,080	1,939

4.4 Multi-scale Image reconstruction

4.4.1 CWMR

For each rock sample, two multi-scale images were reconstructed using the modified Wu et al. (2019) method and the CWMR approach. Figure 4-3 shows the final multi-scale images. A workstation with 32 Intel® Xeon® Platinum 8160 2.1 GHz CPU cores and 1 TB RAM were used for the reconstructions. For the BS rock sample, the modified Wu et al. method took about 12 days, while the CWMR approach took approximately 5 days. For the EBC rock sample, these processes took about 23 and 18 days, respectively. Table 4-10 summarizes the run time and memory consumption for image reconstruction.

Table 4-10 Run time and memory consumption of both reconstruction approaches for the BS and EBC rock samples.

Sample	Run time (CPU core hours)		Memory consumption (GB)	
	Modified Wu et al.	CWMR	Modified Wu et al.	CWMR
BS	432	120	87	65
EBC	552	288	297	276

The CWMR method is significantly faster than the modified Wu et al. method for several reasons. The CWMR divides unresolved porosity into smaller sections using the watershed method and uses unresolved templates to calculate the CCF equation on the cropped HR image. These templates are smaller than the unresolved regions used in the modified Wu et al. method. Table 4-6 shows that the dimensions of the largest unresolved template are significantly smaller than those of the largest unresolved region. This allows us to perform image reconstruction with smaller HR image sizes in our approach. In contrast, the modified Wu et al. method may require a larger HR image to find a suitable template due to the larger unresolved regions. The CWMR method reduces the number of pixels needed for solving the CCF equation, leading to faster computational speed and lower memory consumption. The CWMR approach has a shorter run time for the BS rock (120 CPU hours) compared to the EBC rock (288 CPU hours) due to the smaller size of unresolved templates. Despite having more unresolved regions, the modified Wu et al. method has a lower run time for the BS rock (432 CPU hours) than for the EBC rock (552 CPU hours) because of the larger unresolved regions in the EBC rock sample. The higher memory consumption in the EBC rock is due to the larger size of the LR and HR images.

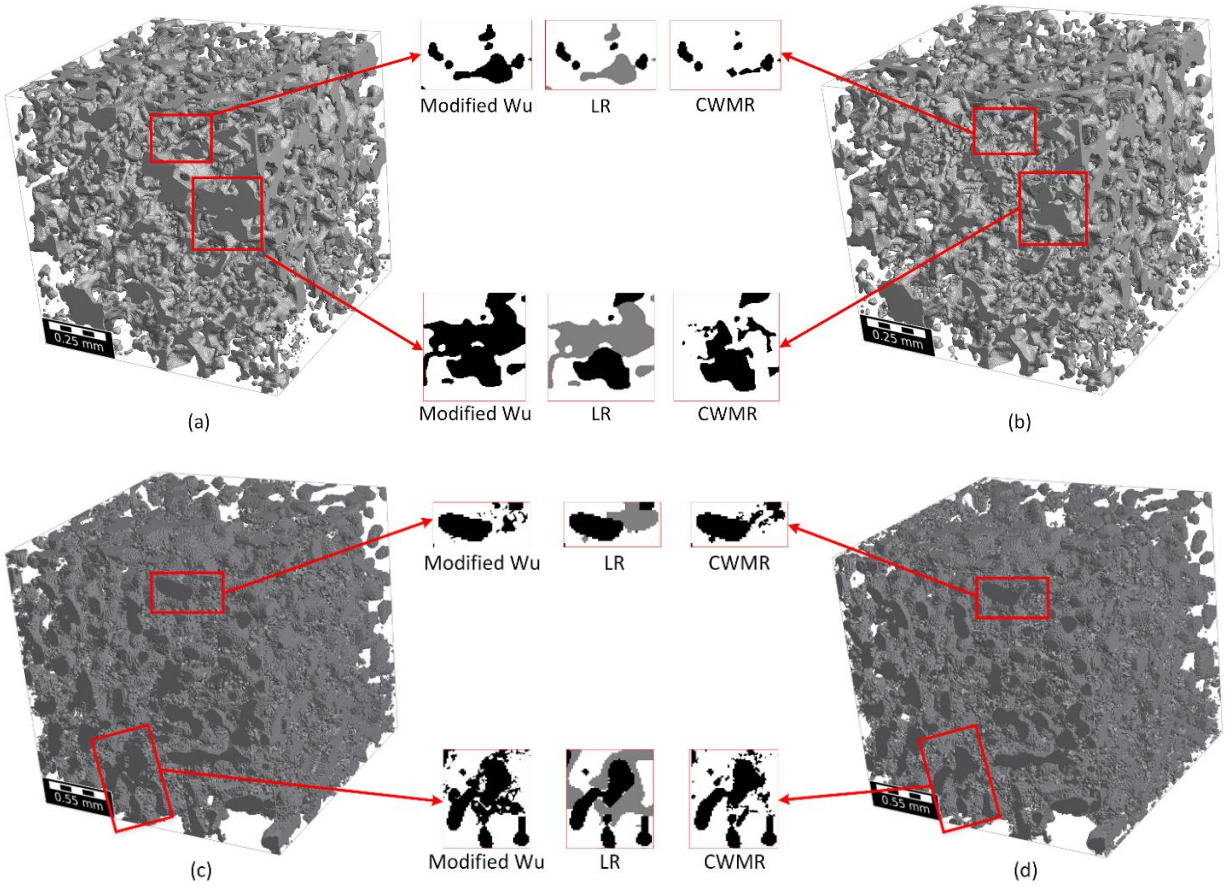

Figure 4-3 Final multi-scale images constructed using (a) the modified Wu et al. and (b) the CWMR method for the BS rock sample, as well as the final multi-scale images constructed using (c) the modified Wu et al. and (d) the CWMR method for the EBC rock sample. Some sections of the multi-scale reconstructed images have been zoomed in and displayed alongside their corresponding sections in the LR image.

In the CWMR method, a different selection process is used compared to the modified Wu et al. method for addressing the OL region. This preserves the connection between resolved and unresolved regions and selects unresolved templates with more micro-pores, resulting in a more realistic final image. As shown in Figure 4-3, some sections of the reconstructed multi-scale images are zoomed in and displayed alongside their corresponding LR image sections. The modified Wu et al. method treats most pixels in some unresolved regions as pores. In contrast, the CWMR method selects templates with more micro-pores in the unresolved regions. However, in the EBC rock, the multi-scale reconstructed images from both methods look similar due to the larger size of unresolved templates and regions. This results in a larger FoV from the HR image being chosen in the templates for both methods, introducing micro-pores into the multi-scale reconstructed images. As shown in the selected templates for the EBC rock, the modified Wu et

al. method adds more isolated micro-pores compared to the CWMR approach because of the larger size of unresolved regions compared to unresolved templates.

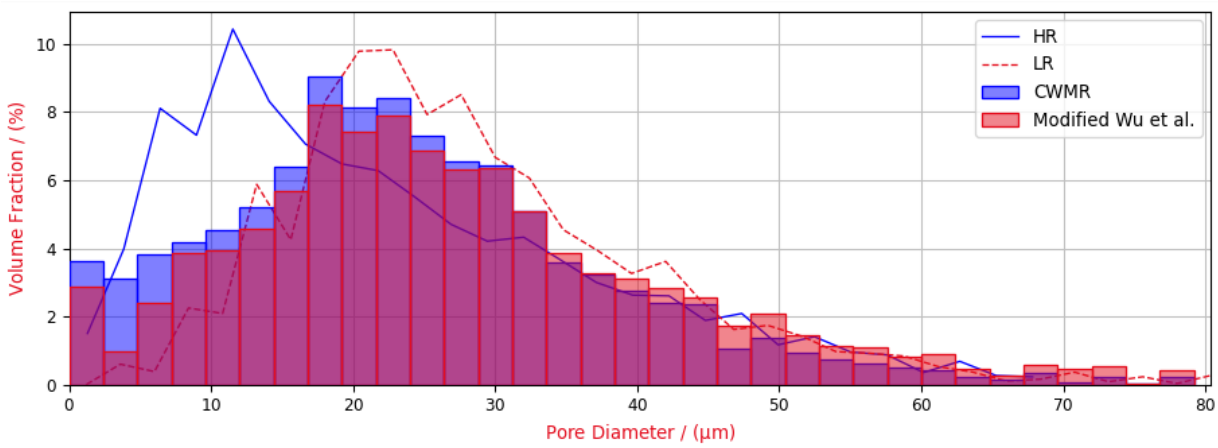

(a)

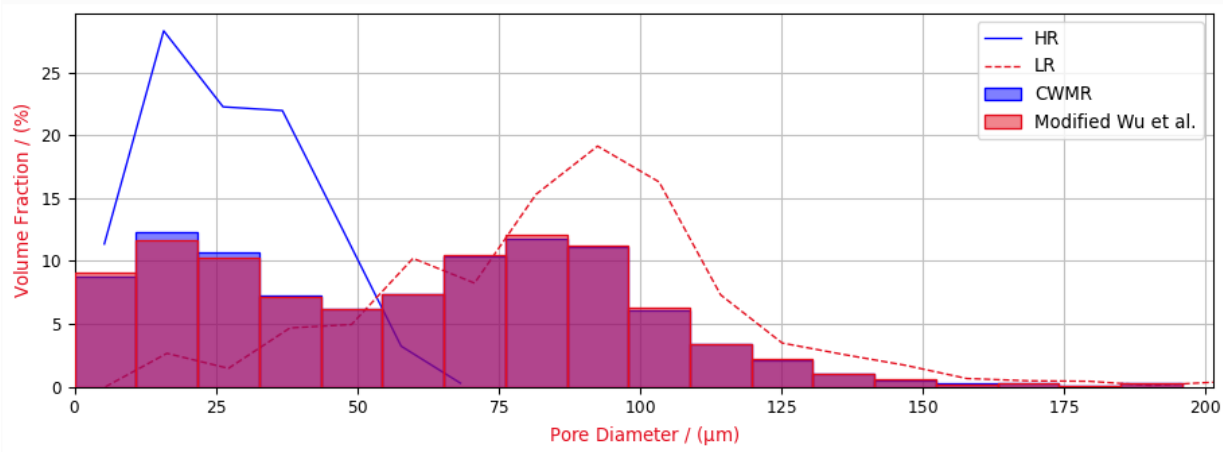

(b)

Figure 4-4 Pore size distribution curves for the reconstructed, HR, and LR images of the (a) BS and (b) EBC rock sample.

To validate the reconstructed images, we used properties such as porosity, absolute permeability, pore size distribution, and Euler number calculated from the HR image. The HR image contains small pores and closely resembles the actual structure of the rock. Therefore, properties calculated using the DNS method for this image closely match the rock's actual properties.

Figure 4-4 illustrates the pore size distribution of the reconstructed, LR, and HR images. The CWMR method effectively incorporates smaller pores into the LR image, resulting in a pore size

distribution more similar to the HR image. Conversely, the modified Wu et al. method selects templates with larger pores and fewer smaller pores. This occurs because selecting templates with the highest CCSIM value leads to incorporating larger pores (macro-pores). In the EBC rock, the final multi-scale reconstructed images show pore size distributions that look more similar to each other due to the larger unresolved templates and regions, leading to the selection of larger templates from the HR image. This increases the likelihood of including large and small pores equally in these templates. At the boundaries, the modified Wu et al. method selects templates that renders the macro-pores (over 75 μm) to appear larger, resulting in more of these pores in the image compared to the CWMR approach. Consequently, the CWMR approach includes more micro-pores (0-35 μm). Comparing the pore size distribution curves of the two rocks reveals that the multi-scale reconstructed image in the BS rock is closer to the HR image and better captures smaller-sized pores. This discrepancy is due to the higher resolution difference in the EBC rock images, resulting in a limited overlap between LR and HR pores. Therefore, only a portion of the smaller pores can be added to the LR image in the EBC rock.

4.4.1.1 Petrophysical Property Evaluation based on Multi-Scale Model

Table 4-11 presents the computed porosity and permeability of the multi-scale reconstructed images. The modified Wu et al. method yields higher porosity for both rocks (16.0% for BS and 27.6% for EBC) compared to the CWMR approach (14.4% for BS and 27.1% for EBC). This difference arises from the larger pores and greater number of pores in the templates selected by the modified Wu et al. method. Moreover, the reason for the difference between the porosity in the multi-scale reconstructed images and the HR image in the BS rock (13.7 %) is due to the existence of some large pores (20 – 30 μm, as shown in Figure 4-4a) that was present only in the LR images (and not the HR image). In contrary, in the EBC rock, when looking at the pore size distribution of the HR image, there are more small-sized pores in the range of 0 to 20 μm, as can be seen in Figure 4-4b. Consequently, a higher porosity of 28.2% results compared to the multi-scale reconstructed images.

The CWMR approach increases the permeability to 161 mD in the EBC rock by establishing fine connections between pores. Conversely, the modified Wu et al. method results in a higher permeability of 258 mD because of the addition of macro-pores, which significantly impacts permeability. The larger discrepancy in the EBC rock is due to the greater resolution difference

between the HR and LR images. The LR image contains macro-pores, and the selected HR templates inserted into the LR image affect permeability. If these templates are not chosen correctly, they can create non-existent throats between macro-pores, causing a sudden permeability increase like a fracture. The modified Wu et al. method's use of large unresolved regions makes it more likely to select templates with large pores that fit between macro-pores in the LR image, creating fracture-like throats.

In the BS rock, adding micro-pores during CWMR reconstruction reduces permeability to 145 mD. The modified Wu et al. method results in a smaller permeability reduction to 159 mD due to the addition of larger pores. In the BS rock, adding micro-pores decreases permeability, while in the EBC rock, it increases permeability. This occurs because the EBC rock's LR image has low connectivity of large pores and continuous unresolved porosity. Thus, micro-pores in the unresolved area control the flow in the multi-scale reconstructed images, creating connections between pores and increasing permeability.

In the EBC rock, macro-pores (over 75 μm) have low connectivity and little effect on the multi-scale reconstructed image permeability. The permeability of multi-scale reconstructed images should be close to those of the HR images because the connections created by selected HR templates increase permeability.

Table 4-11 Porosity and permeability of the multi-scale reconstructed images for the BS and the EBC rock samples

			BS	**EBC**
Total Porosity (%)	Modified Wu et al.		16.0	27.6
	CWMR		14.4	27.1
Permeability (mD)	Modified Wu et al.	X-direction	132	209
		Y-direction	96	100
		Z-direction	250	466
		average	159	258
	CWMR	X-direction	112	117
		Y-direction	69	73
		Z-direction	253	292
		average	145	161

The Berea Sandstone exhibited some bedding planes in the *z*-direction. The plugging also was along these bedding planes which shows higher permeability in this direction than in the *x* and *y* directions. Moreover, the carbonate rock was also heterogeneous naturally and the permeability thus differed in three directions.

4.4.1.2 Morphological Evaluation of Multi-scale Images

The relationship between the Euler number and permeability has long been a challenge [157, 158]. For example, a correlation between the permeability of 2D porous structures of randomly packed overlapping monodisperse circular or elliptical grains and the Euler number [159, 160]. According to this equation, a more negative Euler number corresponds to larger permeability. However, other researchers could not validate this topological model on 3D porous media [161]. Another study by Zhao [162] introduced a correlation linking permeability with the Euler number in complex structures. Their correlation indicates that the trend of permeability changes with Euler number can vary across different samples and highly depends on geometric properties of rocks [162]. In fact, Slotte, Berg and Khanamiri [163] found a very low correlation (45 %) between Minkowski functionals and permeability. It is worth mentioning that permeability is a tensor and direction-dependent, whereas the Euler number is a scalar and does not account for anisotropy in porous media. In principle, seeking a relation between these two parameters in anisotropic porous media is therefore meaningless.

Nonetheless, the Euler number can be a good parameter for the complicity or heterogeneity of samples, because it accounts for the number of isolated pores and flow loops inside of a rock sample [14, 161, 164]. To exemplify this feature, Table 4-12 presents Euler numbers computed for the BS and EBC rock images. In the EBC rock, the LR image shows some isolated macro-pores, resulting in a relatively small positive Euler number of 754. In contrast, for the HR image a larger Euler number of 66,180 was calculated. Figure 4-4b shows that the HR image in this rock contains many small pores. Accordingly, the large Euler number indicates numerous isolated small pores. Therefore, the reconstructed images using the CWMR and the modified Wu et al. approaches have high positive Euler number values (45,938 for the CWMR and 58,062 for the modified Wu et al. approaches). On the other hand, in the BS rock, increasing the resolution creates more flow loops, especially between micro-pores, increasing the pore space complexity and lowering the Euler number (-209 to -1,884). Therefore, the reconstructed images using the CWMR and the modified

Wu et al. approaches have negative Euler number values (-1,891 for the CWMR and -798 for the modified Wu et al. approach) in this rock.

Table 4-12 Euler numbers for the reconstructed, HR, and LR images of the BS and the EBC rock samples

Sample	Euler number			
	LR image	HR image	Modified Wu et al.	CWMR
BS	-209	-1,884	-798	-1,891
EBC	754	66,180	58,062	45,938

4.4.2 OCWMR

The images were reconstructed on a workstation equipped with 32 Intel® Xeon® Platinum 8160 2.1 GHz CPU cores and 1 TB of RAM. For the BS rock sample, the CWMR took approximately 5 days, while OCWMR approach completed the process in around 1.5 days, i.e. 3.3 times faster. In the case of the EBC rock sample, the reconstruction processes took approximately 12 and 4 days to complete (3-fold speedup in OCWMR), respectively. Moreover, for the BS multi-scale image reconstruction, the CWMR consumed 65 GB of memory, while OCWMR completed the process by consuming 2.9 GB of memory, i.e. 22.5 times less. For the EBC multi-scale image reconstruction, the CWMR consumed 276 GB of memory, while OCWMR completed the process by consuming 2.4 GB of memory, 131.4 times less. Runtime and memory consumption details for image reconstruction are summarized in Table 4-13.

Table 4-13 Run time and memory consumption of both reconstruction approaches for BS and EBC rock samples.

Sample	Run time (Days)		Memory consumption (GB)	
	CWMR	OCWMR	CWMR	OCWMR
BS	5	1.5	65	2.9
EBC	12	4	276	2.4

Given the CWMR approach, increasing the number of unresolved templates and subsequently their smaller size could decrease the computational cost and runtime. Therefore, it might be expected

that in this context, the OCWMR approach would have a higher computational cost and runtime compared to the CWMR one. However, there is another point that not only increases the computational cost and runtime in the OCWMR approach compared to CWMR but also significantly reduces them. In the OCWMR approach, calculations are specifically performed to identify various unresolved templates on the LR image with a large voxel size. Moreover, using the Octree structure, only the unresolved templates are computed separately from the rest of the phases in the image. Consequently, this approach involves less computational cost and runtime than CWMR. Furthermore, the computational cost and runtime for the EBC rock sample, despite having more unresolved templates, are lower than those for the BS rock sample, contrary to the CWMR approach. This discrepancy is due to the smaller size (voxels) LR image in the EBC rock compared to the LR image of the BS rock. Since the OCWMR approach operates on the LR image, the computational cost and runtime in the EBC rock are less than those in the BS rock. Thus, the OCWMR approach reduces computational cost, addressing one of the significant challenges in previous multi-scale image reconstruction approaches, such as CWMR, especially in rocks with greater resolution differences between LR and HR images. As discussed earlier, the OCWMR approach utilizes a smaller number of larger unresolved templates due to the application of the watershed algorithm on the original LR image with large voxel size.

Ten realizations of the multi-scale images were reconstructed for each rock sample using the OCWMR approach. An example of both 3D realization of the multi-scale reconstructed image using OCWMR, and the multi-scale reconstructed image using CWMR, are shown for each rock sample in Figure 4-5. Moreover, two random 2D layers of the images are displayed alongside their corresponding LR image layers for comparison purposes. The visual analysis of the images indicates that both approaches have effectively chosen appropriate templates for the unresolved areas. In both rocks, the reconstructed images by both approaches exhibit fine and coarse pores, and suitable connectivity exists between all pores. Therefore, it is expected that there would be a slight difference in the properties of the multi-scale images reconstructed by both approaches. However, since the OCWMR approach has fewer unresolved templates (1,424 and 1,797 for the BS and EBC, respectively) compared to the CWMR (1,939 and 2,080 for the BS and EBC, respectively), it is expected that the number of fine pores in the image reconstructed by OCWMR would be somewhat less than CWMR. By comparing the permeability values in Table 4-7 and Table 4-8, the OCWMR approach obviously provides results closer to the actual value of the HR

image (Figure 4-5). This is due to the higher number of unresolved templates in the CWMR approach, resulting in more fine isolated pores and throats that have been added to the image. In addition, greater permeability reduction happened in the BS rock of the multi-scale image reconstructed by the CWMR approach (141 mD). This shows that the added pores by the CWMR approach created more dead-end throats inside the image and couldn't make connectivity closer to the HR image. However, in the multi-scale image reconstructed by the OCWMR approach, this permeability reduction is less and equal to the permeability of the HR image (147 mD). In the EBC rock, the permeability of the image after adding fine pores in the CWMR approach has increased more (165 mD) because more unnecessary throats have been added, leading to a greater increase in permeability. However, in the multi-scale image reconstructed by the OCWMR approach, the increase in permeability is less and closer (161 mD) to the permeability of the HR image (160 mD).

			Multi-scale images	
Rock	**Image**	**LR image**	**CWMR**	**OCWMR**
BS	3D	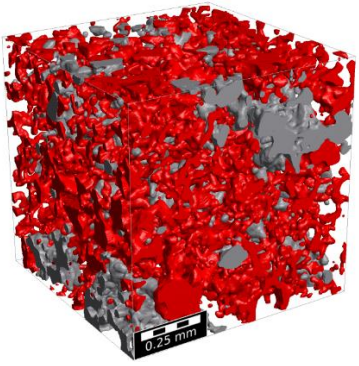		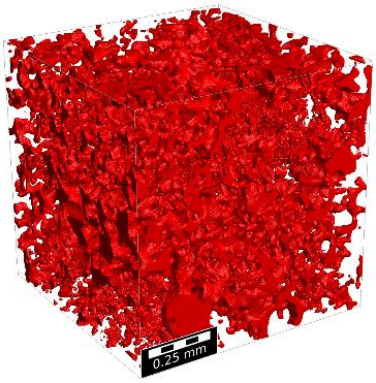
	2D Layer 1	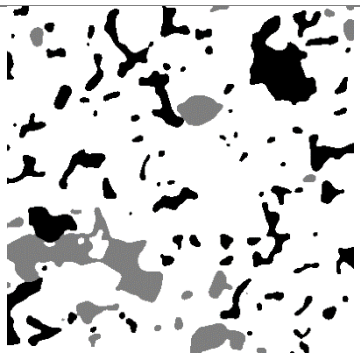	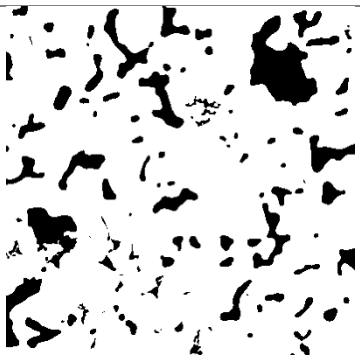	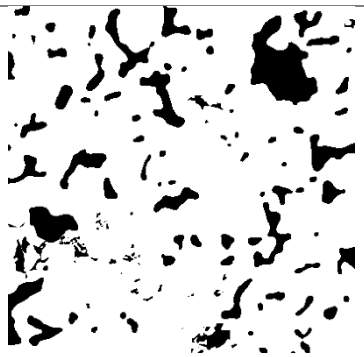

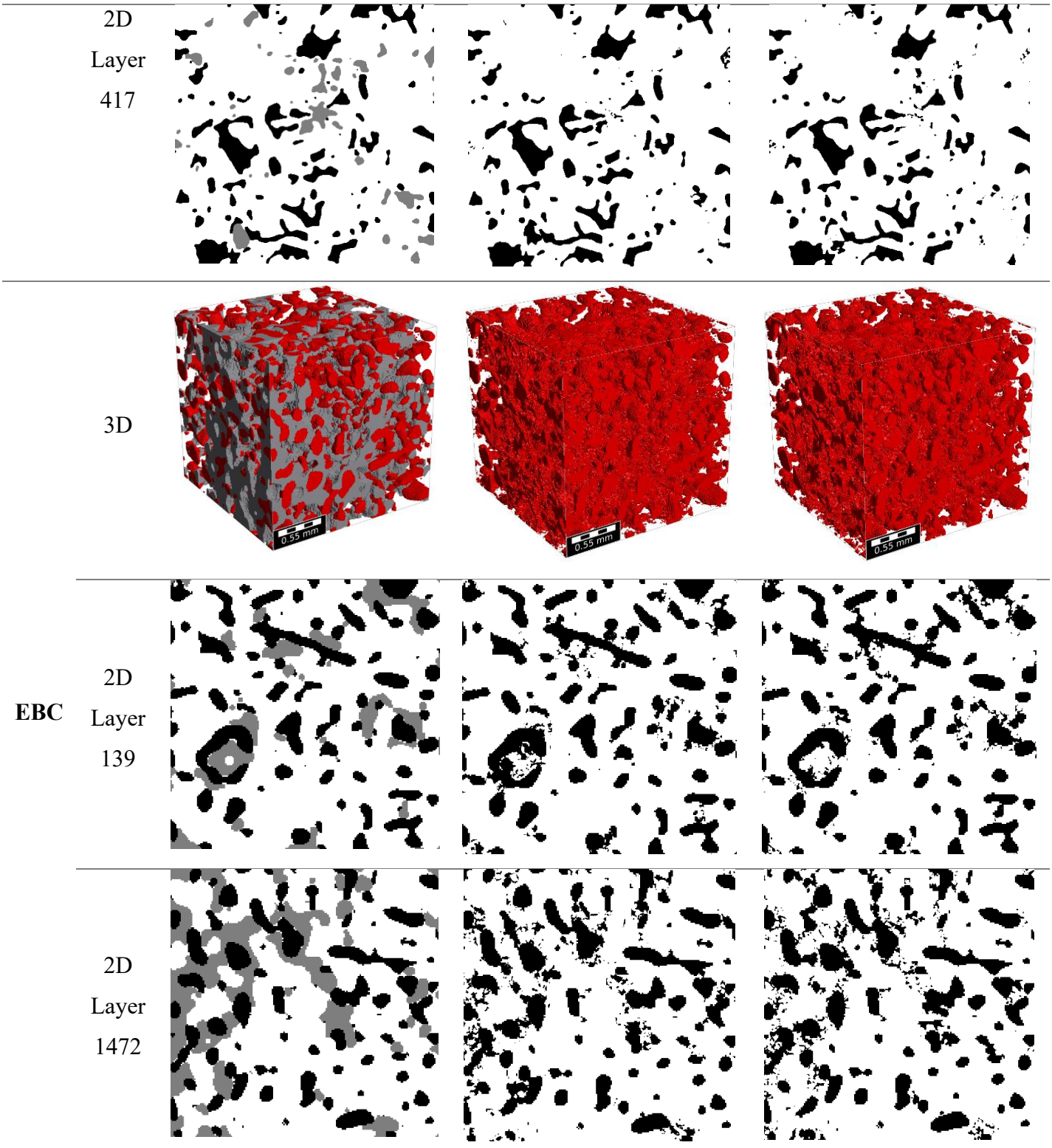

Figure 4-5 Multi-scale 3D and 2D images reconstructed using the OCWMR and the CWMR approaches for the BS and EBC rock samples. Some 2D layers of the reconstructed images have been displayed alongside their corresponding layers in the LR image.

Furthermore, single- and two-phase flow properties were calculated to assess the quality of the reconstructed images. Figure 4-6 shows the absolute permeability distribution of the 10 multi-scale images reconstructed using the OCWMR for both the BS and the EBC rock samples. As evident, the average permeability calculated over 10 reconstructed images by the OCWMR approach shows close agreement to the permeability of the HR images in both rocks. This confirms the accuracy of the proposed approach in multi-scale reconstruction of rock images.

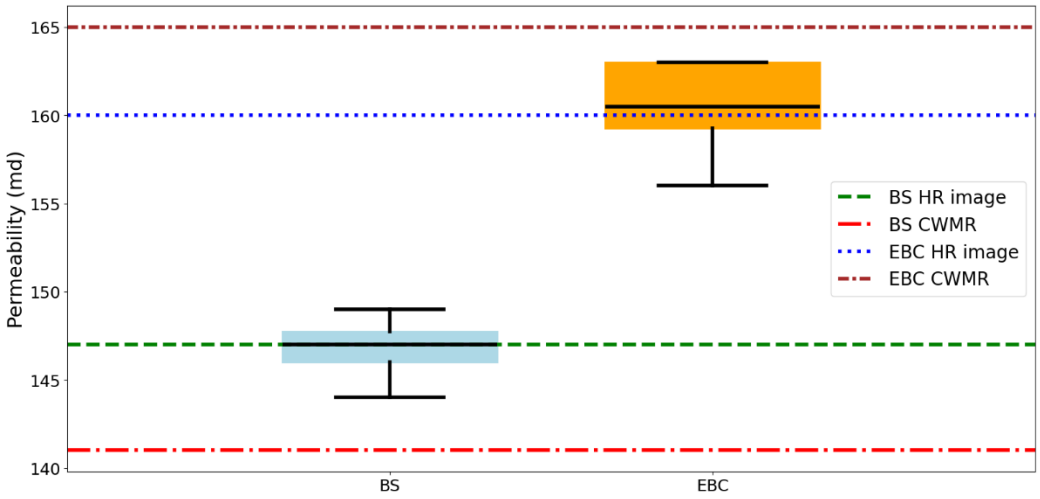

Figure 4-6 The permeability distribution of all multi-scale image realizations reconstructed using the OCWMR for the BS and the EBC rock samples

4.4.2.1 Two-phase flow properties evaluation

We further calculated the properties of the two-phase flow including the capillary pressure and relative permeability curves for both rocks. For this purpose, we considered the 3D realization with best permeability (Figure 4-6) for the OCWMR approach to calculate the two-phase flow properties. Figure 4-7a and Figure 4-7b show the capillary pressure curve for the BS and the EBC rocks, respectively. These curves were obtained on the HR image as well as the reconstructed images using the CWMR and the OCWMR approaches. In these simulations, water and air phases have been considered and these curves were obtained during the drainage process. These curves show that in both rocks, the highest capillary pressure value in the image reconstructed using the CWMR is higher than the image reconstructed using the OCWMR. This is due to the existence of

smaller size pores in the reconstructed images using CWMR and inverse relationship between capillary pressure and pore-throat sizes. In Figure 4-7a, the residual water saturation value of the BS in the OCWMR is lower than that of the CWMR. This shows that in the reconstructed image using the OCWMR, the number of isolated smaller size pores are fewer, and as a result, there are less dead-end throats. Therefore, this has caused a better recovery of the water phase in the image compared to the reconstructed image using the CWMR. However, in Figure 4-7b, the amount of residual water saturation in the OCWMR is higher than that by the CWMR in the EBC rock. This confirms that in the EBC rock, the presence of smaller pores has caused more connectivity between the pores inside the reconstructed image. Therefore, in the reconstructed image using the CWMR, more water has been recovered due to high connectivity. In addition, in both images, the capillary pressure curve in the HR image is closer to the capillary pressure curve in the image reconstructed using the OCWMR.

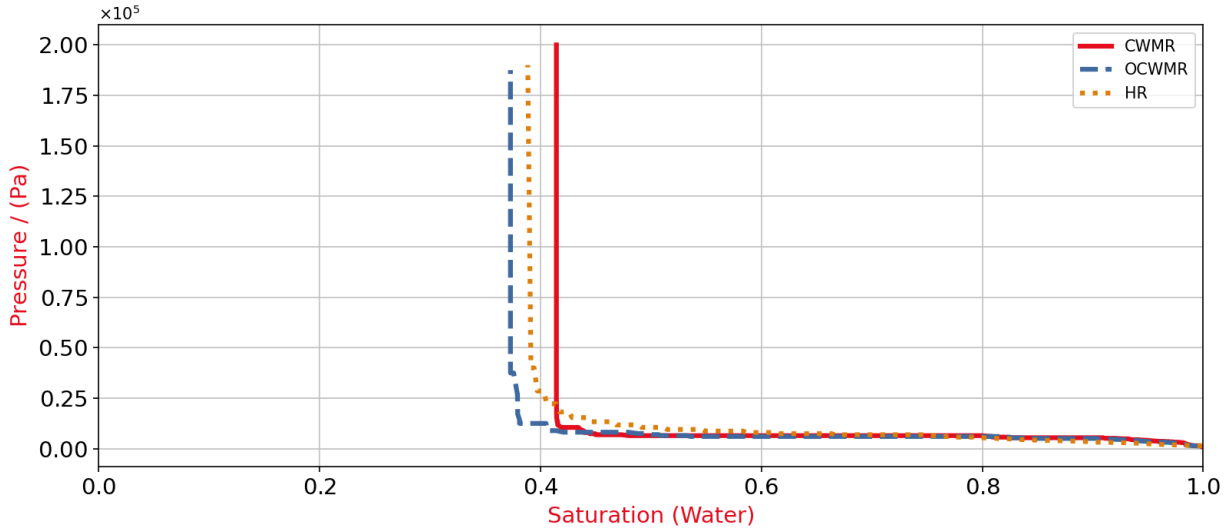

(a)

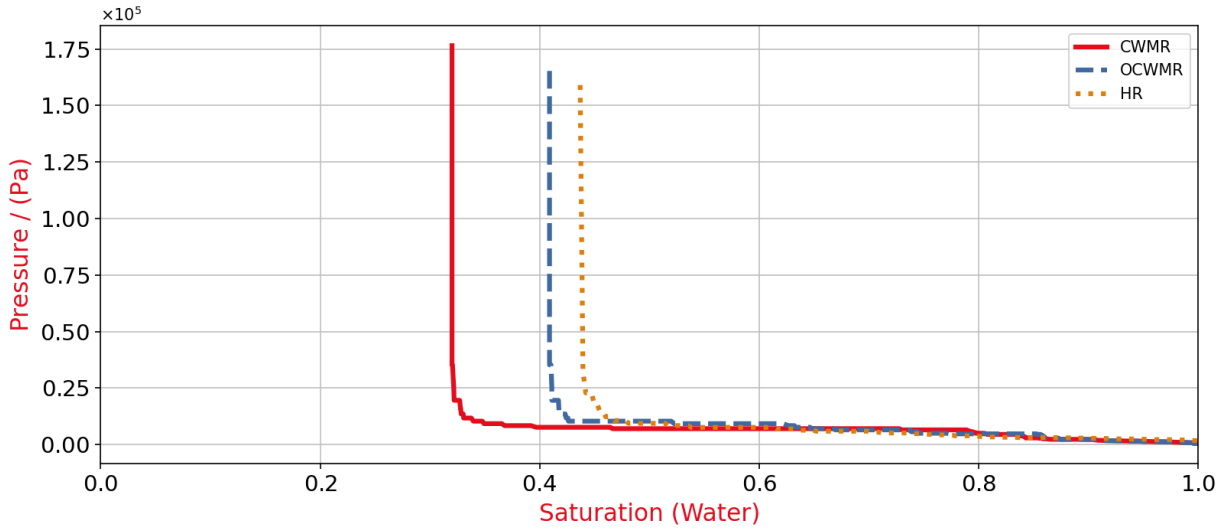

(b)

Figure 4-7 The capillary pressure curves of the HR image as well as reconstructed images using the OCWMR and the CWMR approaches for (a) the BS and (b) the EBC rock sample

Figure 4-8a and Figure 4-8b show the relative permeability curves for the BS and the EBC rocks, respectively. These curves also were obtained on the HR image as well as the reconstructed images using the CWMR and the OCWMR approaches. In these simulations, water and air phases have been considered, and the curves of the drainage and imbibition processes have been shown. In Figure 4-8a, the water relative permeability curve of the image reconstructed using the OCWMR is placed above the image reconstructed using the CWMR in the BS rock. This shows again that the image reconstructed using the CWMR has more isolated smaller size pores and dead-end throats. Therefore, the water relative permeability values have more reductions at higher water saturations. However, in Figure 4-8b for the EBC rock, the water relative permeability curve in the image reconstructed using the OCWMR is lower than that of the reconstructed image by the CWMR at higher water saturations. This shows the greater effect of smaller size pores in increasing the permeability in the reconstructed image using the CWMR by improving the connectivity between the larger size pores. Moreover, in both rocks the relative permeability curves in the HR image are closer to the relative permeability curves in the image reconstructed using the OCWMR.

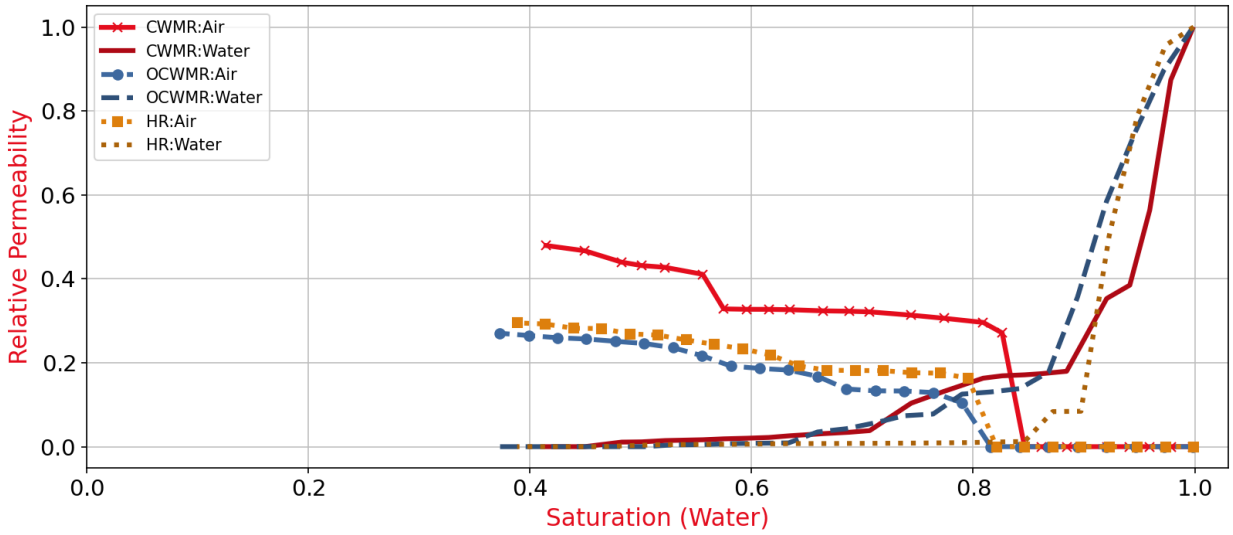

(a)

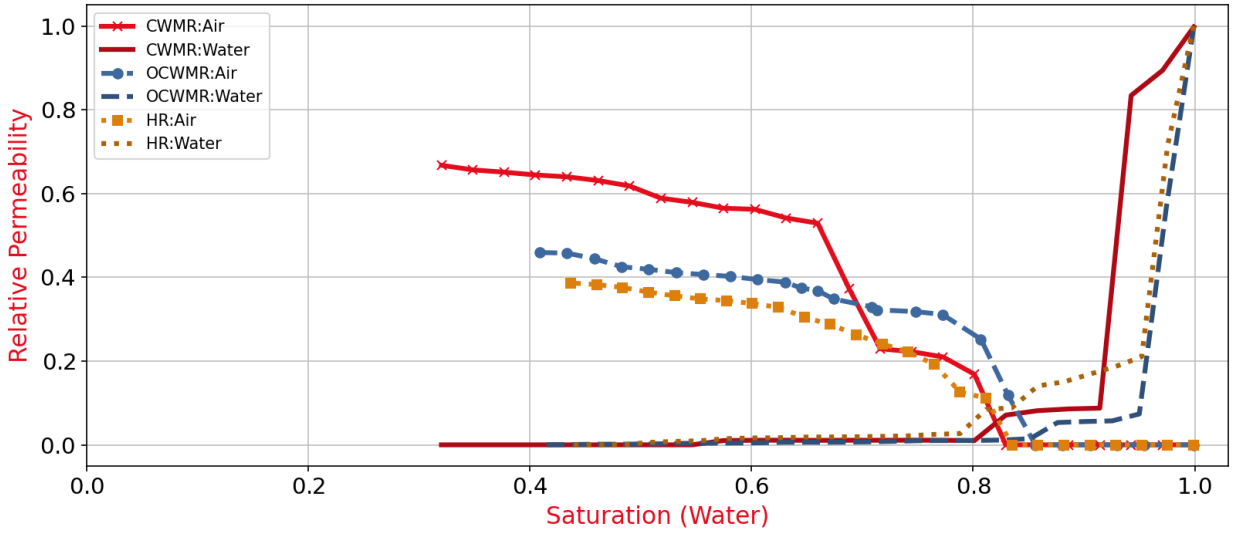

(b)

Figure 4-8 The relative permeability curves of the HR image as well as reconstructed images using the OCWMR and the CWMR approaches for (a) the BS and (b) the EBC rock samples

4.5 Muli-scale PNM reconstruction

As described, 30 different realizations of the multi-scale PNM were reconstructed using three statistical-MPR, ANN-MPR and ANN-Octree-MPR methods for the ILS rock. Ten realizations were reconstructed with each method. At first, to show the importance of scale connection, the permeability of reconstructed pore networks was calculated in all realizations of statistical-MPR

and ANN-MPR methods, which is shown in Table 4-14. The ANN-MPR method produces an average permeability value of 252 mD, closely matching the experimental permeability of 259 mD, while the average permeability value of statistical-MPR method is 308 mD. Additionally, the permeability values from the ANN-MPR method have a standard deviation of 3, significantly lower than 38, which is the standard deviation with the statistical-MPR method. This shows that the correct connection between the scales is much more important than the PNM that is added into the unresolved area and the existence of bias in these connections causes the error in the reconstruction to increase. Moreover, the ANN-MPR method shows a lower standard deviation in porosity (0.05) compared to the statistical-MPR method (0.11). The difference in porosity values between both methods and the experimental value (18.9%) arises because pores smaller than 3.9 μm are unresolved in the image.

Table 4-14 Permeability values of the reconstructed multi-scale PNMs using statistical-MPR and ANN-MPR methods in 10 different realizations for the ILS rock sample

Realization	Porosity (%)		Permeability (mD)	
	Statistical-MPR	**ANN-MPR**	**Statistical-MPR**	**ANN-MPR**
1	11.8	11.1	293	251
2	11.8	11.1	302	252
3	11.7	11.1	275	247
4	11.8	11.1	368	252
5	11.7	11.2	288	255
6	11.7	11.1	305	257
7	11.8	11.0	301	251
8	12.0	11.1	377	252
9	11.9	11.1	266	255
10	11.6	11.2	310	252
Average	11.78 ± 0.11	11.11 ± 0.05	308 ± 38	252 ± 3

Table 4-15 shows the experimental porosity and permeability for the ILS rock sample. According to Tables 4-14 and 4-15, it is obvious that the networks reconstructed using the ANN-MPR method

have permeability values closer to the experimental permeability of the rock compared to the statistical-MPR method. Before connecting the scales, the resolved PNM is extracted from the LR image, and micro-networks are added to the system using the same statistical-MPR method. The main difference in permeability values between the two network reconstruction methods lies in how the scales are connected. In the statistical-MPR method, this connection relies solely on the overlap between large pores and deleted small pores. This approach lacks information about the actual rock structure and images. In contrast, our method uses an ANN network trained on the extracted PNM from the HR image to create the connections. With our method, the length and diameter of the added throats are estimated by this trained network, avoiding the need for a special coefficient that could introduce bias. This approach connects pores across scales in a way that more accurately reconstructs the rock's original structure, with throat length and diameter reflecting the true characteristics of the rock. Thus, the connection method between pores at different scales is crucial to the quality of the reconstructed network.

Table 4-15 Experimental porosity and permeability values of the ILS rock sample

Rock sample	**Experimental properties**	
	Porosity (%)	**Permeability (mD)**
ILS	18.9	259

Figures 4-9 and 4-10 display the pore and throat size distributions for reconstructed networks using the statistical-MPR and ANN-MPR methods. We selected the realizations with permeability values closest to the experimental permeability of the ILS rock. For the ANN-MPR method, we chose realization number 6, which has a permeability of 257 mD. For the statistical-MPR method, we chose realization number 3, with a permeability of 275 mD. The average pore size is 103.7 μm in the ANN-MPR method and 104.4 μm in the statistical-MPR method. The standard deviation is 59.4 μm for the ANN-MPR method and 58.2 μm for the statistical-MPR method. The pore size distributions in the reconstructed networks from both methods are nearly identical. This similarity arises because the stochastic networks are reconstructed similarly, except for the way the pores are connected across scales. However, the figures reveal a slight difference between the PNMs. The stochastic network of the statistical-MPR PNM has more micropores than the ANN-MPR multi-scale PNM. This difference results from the statistical approach to generating the stchastoic PNM

for unresolved porosity. In other realizations, the ANN-MPR multi-scale PNM might contain more pores than the statistical-MPR multi-scale PNM, or the two methods might contain completely same pore size distributions. Despite the similarities in pore size distributions, the permeability values differ. Therefore, pore size distribution alone cannot determine the accuracy of a reconstructed network.

Figure 4-10 shows that the throat size distribution varies between the two methods. The average throat size is 69.0 μm in the ANN-MPR method and 62.4 μm in the statistical-MPR method. The standard deviation is 47.5 μm for the ANN-MPR method and 45.8 μm for the statistical-MPR method. This difference stems from how the throat diameters are assigned across scales. Since the throat sizes are nearly the same before adding new throats, the average throat size in the statistical-MPR method (62.4 μm) compared to the ANN-MPR method (69.0 μm) suggests that the statistical-MPR method introduces additional throats across scales. In the statistical-MPR method, the throat diameter is determined by the diameters of the connected pores, using a factor known as the shape factor. Specifically, the method sets the throat diameter as a fraction of the smaller pore diameter. This approach, however, introduces bias into the reconstruction of the multi-scale PNM. Conversely, the ANN-MPR method estimates throat diameters using an ANN, resulting in different values from those in the statistical-MPR method. Comparing permeability values shows that the ANN-MPR method, despite lacking bias, produces more accurate reconstructed networks. Additionally, the number of new throats with diameter smaller than 40μm in the statistical-MPR method is slightly higher than those in the ANN-MPR method. This results in higher permeability values for networks reconstructed with the statistical-MPR method compared to those using the ANN-MPR method.

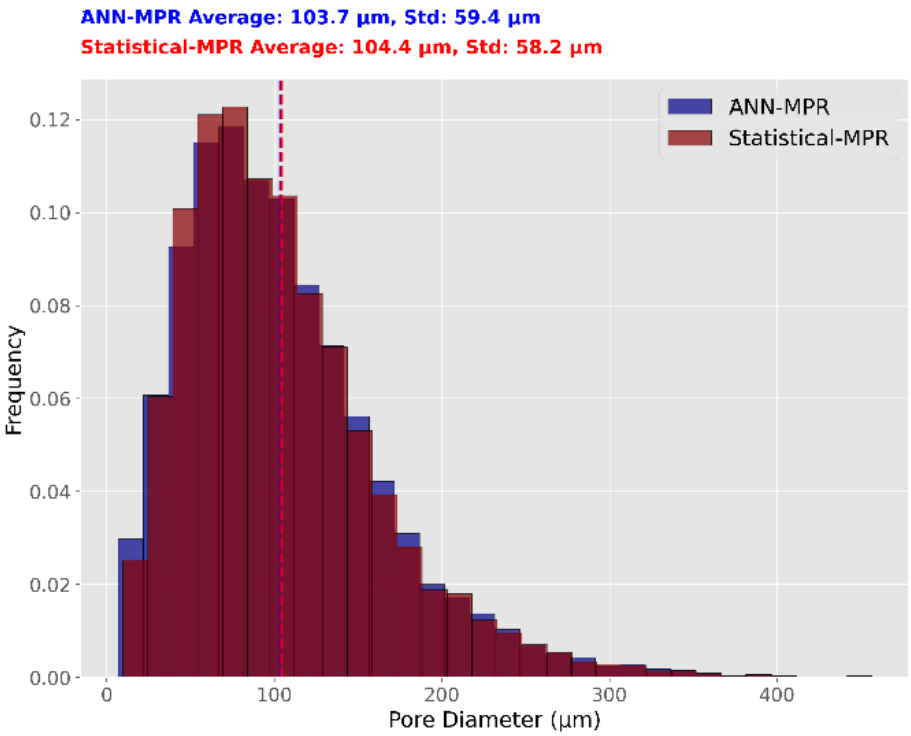

Figure 4-9 Pore size distribution for selected realization of reconstructed multi-scale PNMs using ANN-MPR and statistical-MPR methods

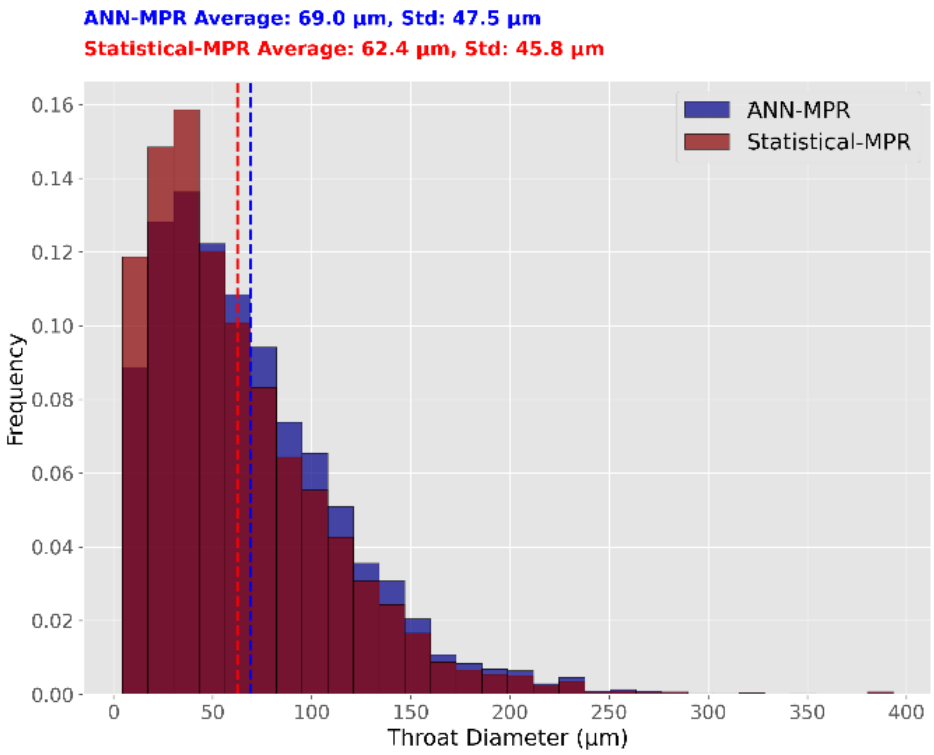

Figure 4-10 Throat size distribution for selected realization of reconstructed multi-scale PNMs using ANN-MPR and statistical-MPR methods

Figure 4-11 shows the throat length distribution curve for the selected realizations of the statistical-MPR and ANN-MPR methods. The average length of the throats in the ANN-MPR method is 160 µm and in the statistical-MPR method it is 145.6 µm. Moreover, the standard deviation in the ANN-MPR method is 83.0 µm and in the statistical-MPR method it is 92.1 µm. The number of throats in the multi-scale PNM reconstructed using ANN-MPR is 13,612, while it is 14,184 in the multi-scale PNM reconstructed using the statistical-MPR method. Therefore, the statistical-MPR method produces more throats than the ANN-MPR method. Additionally, it connects a greater number of pores in the unresolved cluster to surrounding pores. As a result, the statistical-MPR method has more throats shorter than 100 µm. Furthermore, it also generates some throats longer than 500 µm, which do not appear in the ANN-MPR method. This suggests that some pores in the unresolved cluster are connected to more distant pores within the resolved porosity. Therefore, it is crucial to base the selection of throat diameter and length on the original structure of the HR image.

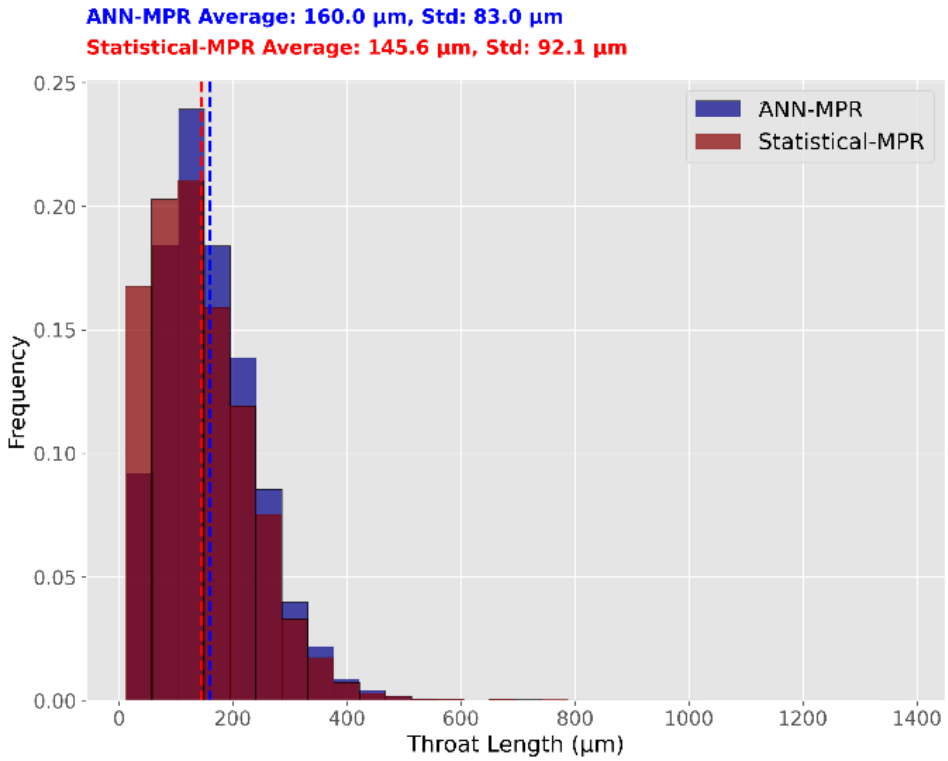

Figure 4-11 Throat length distribution for selected realization of reconstructed multi-scale PNMs using ANN-MPR and statistical-MPR methods

Moreover, Figure 4-12 displays the coordination number distribution for the selected realizations of the two methods. The coordination number distribution differs between the statistical-MPR and ANN-MPR methods. In the ANN-MPR method, the ANN determines whether two pores connect based on their size and coordinates. In contrast, the statistical-MPR method connects a large pore to all smaller pores that overlap with the small pores overlapping the large pore. As a result, the unresolved area pores in the statistical-MPR method connect to a larger number of pores, leading to higher average coordination number (2.94) compared to the ANN-MPR method (2.77). Moreover, the standard deviation is 1.75 in the ANN-MPR method and 2.3 in the statistical-MPR method. This difference is evident in the figure, where the statistical-MPR method shows higher values. The increased number of throats between pores across scales contributes to the higher permeability observed in networks reconstructed using the statistical-MPR method.

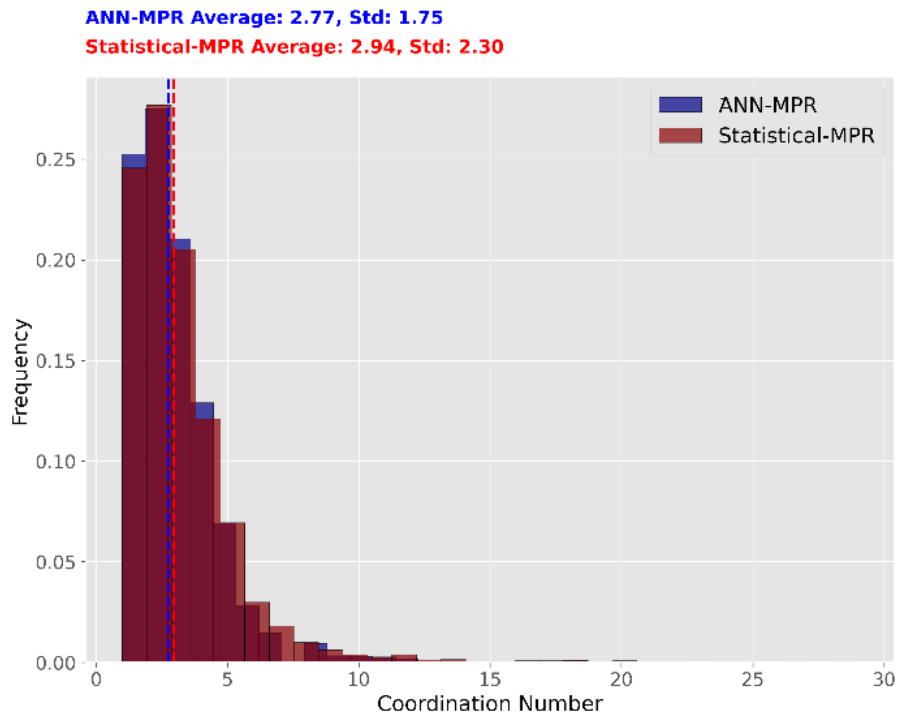

Figure 4-12 Coordination number distribution for selected realization of reconstructed multi-scale PNMs using ANN-MPR and statistical-MPR methods

The capillary pressure and relative permeability curves for the selected realization using two methods are shown in Figures 4-13 and 4-14. These simulations consider water (w) and air (nw) phases, with a focus on the drainage process. In Figure 4-13, the capillary pressure curves for both methods appear nearly identical during drainage. This similarity arises because both methods distribute pore sizes similarly, and capillary pressure depends on pore size distribution. However, the irreducible water saturation differs between methods. The reconstructed PNM using the ANN-MPR method has a higher irreducible water saturation (0.63) than the one using the statistical-MPR method (0.6). This is due to higher permeability in the statistical-MPR PNM, which allows air to displace more water. Figure 4-14 shows that the water relative permeability curve is higher for the statistical-MPR method than for the ANN-MPR method. This suggests that the PNM reconstructed with the ANN-MPR method has lower effective permeability for water, allowing air to displace water more easily. Conversely, the air relative permeability curve is lower for the statistical-MPR method than for the ANN-MPR method at the end of drainage. As the system approaches irreducible water saturation, the statistical-MPR method, with more small throats (under 100 μm), has difficulty displacing the water. This reduces its relative permeability

compared to the ANN-MPR method. Consequently, the PNM reconstructed with the ANN-MPR method reaches its irreducible water saturation level sooner.

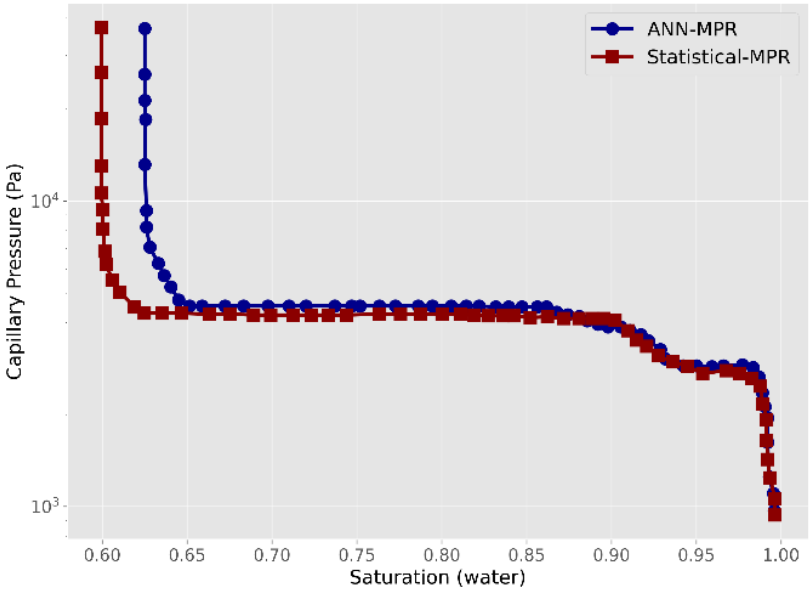

Figure 4-13 The capillary pressure curves of the reconstructed images using the ANN-MPR and the statistical-MPR methods for the ILS rock samples

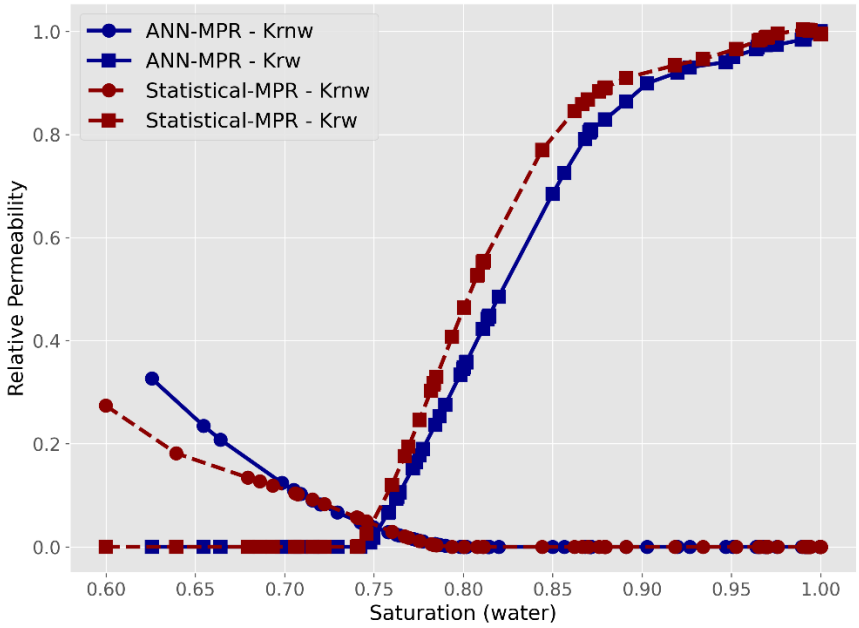

Figure 4-14 The relative permeability curves of the reconstructed images using the ANN-MPR and the statistical-MPR methods for the ILS rock samples

Therefore, according to the results, a high percentage of reconstructed PNMs using ANN-MPR method are very accurate and the permeability of the reconstructed PNMs is close to the experimental permeability of the ILS rock, but the statistical-MPR method has a lower percentage of reconstructed PNMs close to the real rock structure. This shows that the correct connection between the scales is very important and the existence of manual factor and the presence of bias in these connections causes the error in the reconstruction to increase.

Moreover, the ANN-Octree-MPR method has been used in order to reduce memory consumption in the multi-scale PNM reconstruction. For this purpose, 10 different realizations have been reconstructed using this method and compared with the reconstruction realizations with ANN-MPR method. Figure 4-15 shows the distribution of permeability values for realizations reconstructed using two methods. As is known, the ANN-Octree-MPR method has very close permeability values with the ANN-MPR method, which shows the appropriate accuracy of this method. Moreover, another point that is clear is that the reconstructed realizations have a permeability value even closer to the experimental permeability of ILS rock. The reason is the use of the OCWMR method for multi-scale image reconstruction, which considers more appropriate

templates for unresolved clusters than the ANN-MPR method. Moreover, the separate extraction of the PNM from these clusters did not reduce the accuracy of the multi-scale PNM reconstruction.

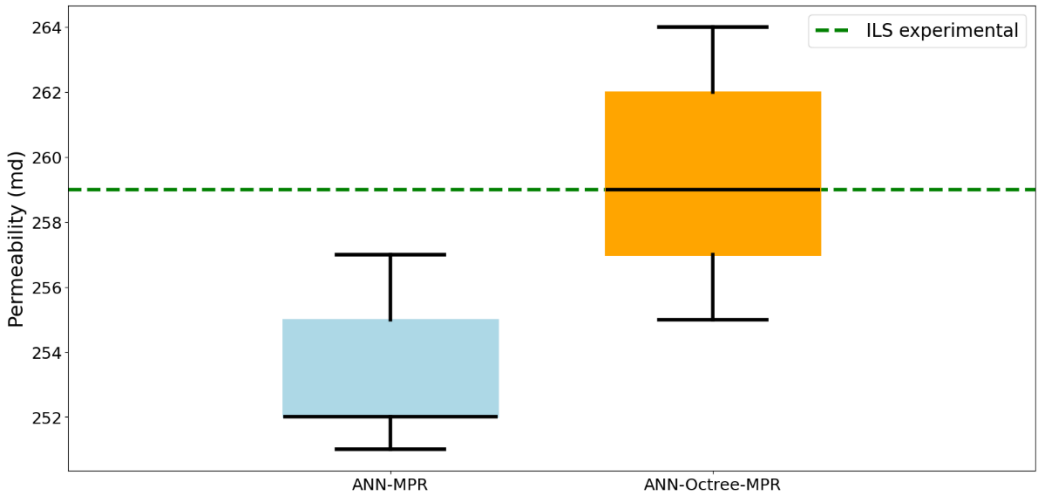

Figure 4-15 The permeability distribution of all multi-scale PNM realizations reconstructed using the ANN-MPR and ANN-Octree-MPR methods for the ILS rock sample.

But as stated, the main reason for introducing the ANN-Octree-MPR method is to reduce the memory consumption for multi-scale PNM reconstruction. For this reason, the amount of memory consumed by these two methods for one realization is shown in Table 4-16. As is known, the ANN-MPR method requires more memory than the ANN-Octree-MPR method due to the generation of an equivalent stochastic PNM that has a large size. Because in the ANN-Octree-MPR method, the PNM in the unresolved porosity is extracted from the unresolved clusters separately, and because these clusters have a smaller size compared to the LR image, they require less memory. According to Table 4-16, the ANN-MPR method consumes 142 GB and the ANN-Octree-MPR method consumes 38 GB for the multi-scale PNM reconstruction. While both methods have almost the same runtime, therefore the ANN-Octree-MPR method only reduces the memory consumption in the multi-scale PNM reconstruction and does not have much effect on the runtime.

Table 4-16 Run time and memory consumption of ANN-MPR and ANN-Octree-MPR reconstruction methods for the ILS rock sample.

Method	Run time (CPU hours)	Memory consumption (GB)
ANN-MPR	9	142
ANN-Octree-MPR	11	38

In Figure 4-16, one realization of the 3D multi-scale PNM reconstructed by each of the statistical-MPR, ANN-MPR and ANN-Octree-MPR methods is shown. Moreover, the PNM extracted from the LR image is also presented. As is clear in the figure, the reconstructed multi-scale PNM using the statistical-MPR method has added more throats between the two scales. In addition, it is clear that all statistical-MPR, ANN-MPR and ANN-Octree-MPR methods have not added a throat between its pores and the pores in the resolved porosity in some unresolved clusters. Therefore, these throats actually exist in the form of isolated clusters in the multi-scale PNM and will not have an impact on the calculation of the total permeability. Moreover, another issue that can be found from the multi-scale PNMs reconstructed by the two ANN-MPR and ANN-Octree-MPR methods is that these two networks have different PNMs in the unresolved clusters and that is why different throats are seen between the two scales. But as we observed, their permeability was close to each other. Therefore, it can be concluded that the method of adding throats between two scales is much more important than the PNM that is added into the unresolved porosity.

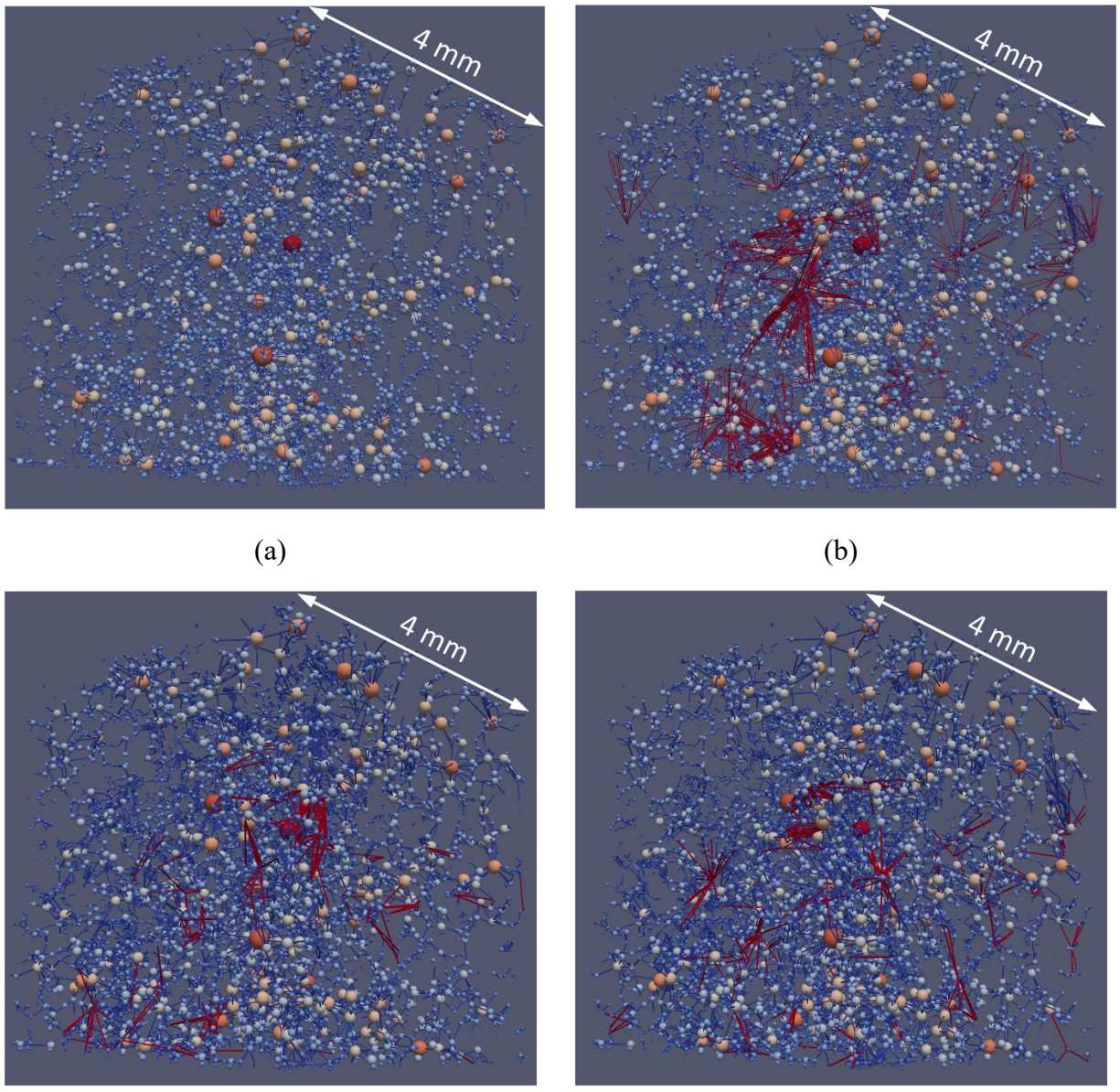

Figure 4-16 (a) The PNM extracted from the LR image. Moreover, one realization of 3D multi-scale PNMs reconstructed using the (b) statistical-MPR (b) ANN-MPR and (c) ANN-Octree-MPR methods for the ILS rock sample

4.6 Multi-scale Modeling

We have so far reconstructed multi-scale images and PNMs on rocks that contain unresolved porosity. In both the reconstruction of images and PNMs, we provided methods so that this reconstruction is done on each scale separately and finally the multi-scale reconstruction is done. But after reconstructing the structures, it is necessary to provide a method so that there is no need

to calculate the image properties on the small voxel size, or in the case of the PNM, there is no need to perform modeling on all pores and throats. Because this work, despite its high accuracy, has a very high computational cost and requires powerful systems for this work. As explained in chapter 3, in this research, two modeling methods, one for multi-scale image modeling and the other for multi-scale PNM modeling have been presented, which reduces the memory consumption and runtime for calculating properties on it. In the following, the results of these methods are given in detail along with their discussion.

4.6.1 Multi-scale DNS modeling

As discussed in Chapter 3, we calculated the permeability of 10 multi-scale images reconstructed using the MDNS-1 method for BS rock. These calculations were done on the small voxel size of the multi-scale images and were compared with the permeability of the HR image. Now, we have recalculated the permeabilities of these 10 realizations using the MDNS-2 method and compared them with the results from the MDNS-1 method. Table 4-17 presents the number of unresolved clusters and the number of unresolved clusters with zero permeability for these realizations. The data in Table 4-17 show that approximately 42% of the clusters in the realizations have zero permeability. Therefore, these clusters do not affect the overall permeability of the multi-scale image.

Table 4-17 Unresolved clusters characteristics for all realizations of multi-scale images reconstructed using the OCWMR in the BS rock sample

Realization	Unresolved clusters	Zero permeability	Percent (%)
1	488	201	41.1
2	488	203	41.5
3	488	206	42.2
4	488	198	40.5
5	488	203	41.5
6	488	210	43.0
7	488	202	41.4
8	488	201	41.1

9	488	205	42.0
10	488	199	40.7

Next, Figure 4-17 shows the permeability distribution values for 10 realizations of reconstructed images obtained using the MDNS-1 and MDNS-2 methods. The results clearly demonstrate that the multi-scale modeling of DNS using MDNS-2 method is highly accurate. The permeability values of the realizations from MDNS-2 closely match those from the MDNS-1 method. This accuracy is crucial for multi-scale DNS modeling, as the MDNS-2 method allows for the calculation of various properties on large multi-scale images with reduced time and memory usage. To proceed, we selected the best realization based on its permeability value's closeness to the HR image. Realization number 7 was chosen, with a permeability of 146 mD, calculated using the MDNS-2 method. Additionally, according to Table 4-17, this realization contains 488 unresolved clusters, of which 202 have zero permeability.

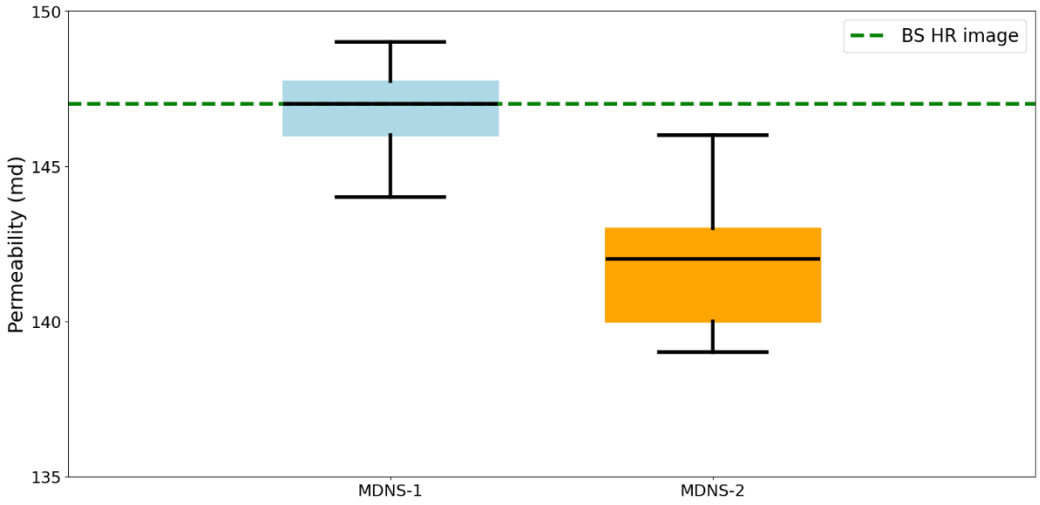

Figure 4-17 The permeability distribution of all multi-scale image realizations reconstructed using the OCWMR for the BS rock sample. The permeability values are calculated using both MDNS-1 and MDNS-2 methods

Table 4-18 shows the computationsl cost of two MDNS-1 and MDNS-2 methods for calculating permeability on the selected realization. As is known, the MDNS-1 method has more computational cost than the MDNS-2 method. The MDNS-1 method consumes 29 GB of memory for this image to calculate the permeability value in 96 minutes, while the MDNS-2 method requires 13 GB of memory to calculate the permeability value for this image in 12 minutes.

Table 4-18 Run time and memory consumption of MDNS-1 and MDNS-2 modeling methods for the BS rock sample.

Method	Run time (Mins)	Memory consumption (GB)
MDNS-1	96	29
MDNS-2	12	13

The following section presents the capillary pressure and relative permeability curves for the selected realization. Figure 4-18 shows the capillary pressure curve, while Figure 4-19 illustrates the relative permeability curve for both methods applied to the BS rock sample. As evidenced by these curves, the MDNS-2 method closely aligns with the capillary pressure and relative permeability curves obtained using the MDNS-1 method, demonstrating the accuracy of the MDNS-2 approach. Notably, the MDNS-2 method results in a lower irreducible water saturation compared to the MDNS-1 method. This difference arises because, in GeoDict software, the calculation of capillary pressure values considers only the resolved porosity of the image, as the main structure of the unresolved clusters is not available. As a result, the MDNS-2 method accounts for fewer small pores, leading to slightly lower irreducible water saturation and a reduced maximum capillary pressure.

Furthermore, the MDNS-2 method calculates relative permeability by removing the existing structure within the resolved cluster and relying solely on the total permeability value of this space to determine permeability values at different saturations. In contrast, the MDNS-1 method, which incorporates smaller pores, results in a higher degree of trapping within the multi-scale image structure, causing more water to remain in the image. The presence of small pores in the BS rock contributes to a decrease in the permeability of the LR image. The MDNS-1 method, which directly calculates on these small pores, reflects this decrease more accurately than the MDNS-2

method. Consequently, the relative permeability curve in the MDNS-2 method is slightly higher than that of the MDNS-1 method.

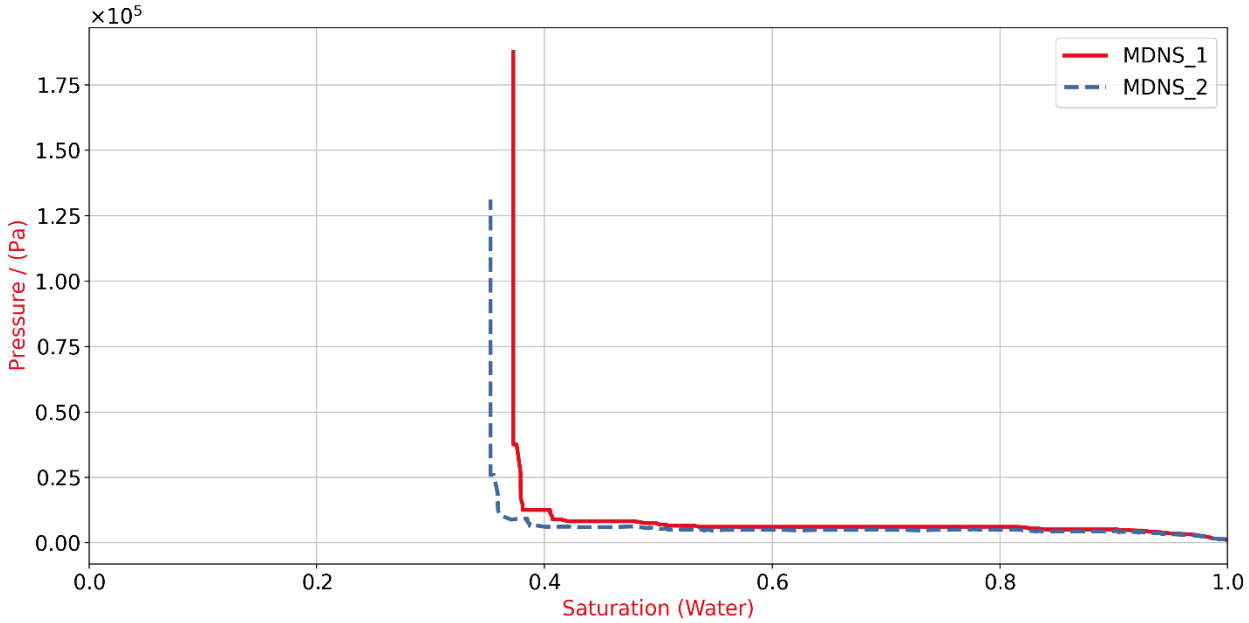

Figure 4-18 The capillary pressure curves of the reconstructed image which calculated using the MDNS-1 and MDNS-2 methods for the BS rock sample

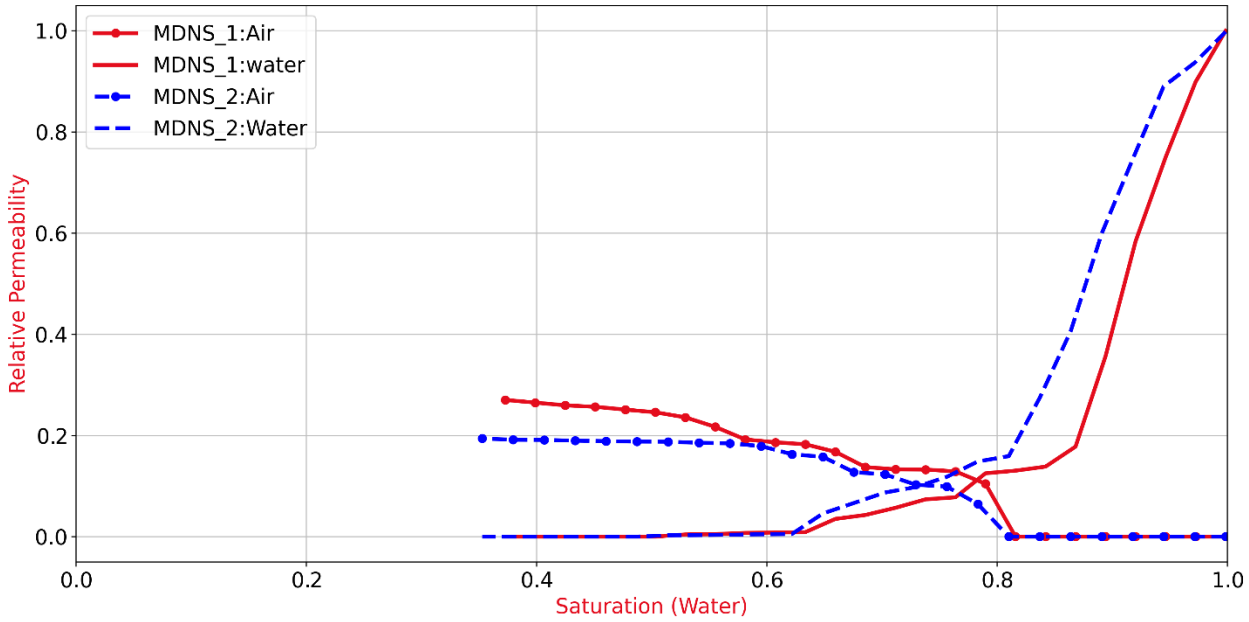

Figure 4-19 The relative permeability curves of the reconstructed image which calculated using the MDNS-1 and MDNS-2 methods for the BS rock sample

4.6.2 Multi-scale PNM modeling

To verify the accuracy of the upscaled multi-scale PNM modeling method, we compared the properties calculated by this method with those obtained from the regular PNMs using the ANN-MPR method across 10 different realizations. For this comparison, we applied our upscaling PNM method to reconstruct PNMs in all 10 realizations. Table 4-19 presents the characteristics of one realization for both methods. According to this table, the upscaled PNM contains 5,641 pores, whereas the ANN-MPR regular PNM has 13,737 pores. Similarly, the upscaled PNM has 6,231 throats, compared to 13,697 in the ANN-MPR regular PNM. As expected, the upscaling process significantly reduces the number of pores and throats, lowering the computational cost of property calculations. Consequently, this reduction decreases the porosity in the upscaling method, dropping it from 11.1% to 8.6%.

It is important to note the difference between the porosity of the ANN-MPR regular PNM and the experimental porosity of the ILS rock, which is 18.9%. This discrepancy arises from the absence of pores smaller than 3.9 μm. Furthermore, the permeability of the upscaled PNM, measured at 254 mD, is nearly identical to that of the reconstructed PNM using the ANN-MPR method, which is 255 mD. Additionally, the number of throats in the regular PNM (13,697) is slightly less than the number of pores (13,737). This is due to the presence of PNMs in unresolved clusters, which do not add throats between themselves and the pores in the resolved porosity. As a result, these isolated clusters do not influence the network's permeability.

Table 4-19 Regular and upscaled PNMs characteristics

Property	**PNM**	
	Regular PNM	**Upscaled PNM**
Number of pores	13,737	5,641
Number of throats	13,697	6,231
Porosity (%)	11.1	8.6
Permeability (mD)	255	254

In Figure 4-20, one realization of the 3D multi-scale ANN-MPR regular PNM is shown next to the upscaled 3D multi-scale PNM. As is clear in the figure, the upscaled PNM considers a base pore in each unresolved cluster and connects the surrounding pores directly to it. In these two PNMs, an unresolved cluster is shown as zoomed in the regular PNM. As it is clear, in the up-scaled PNM, a base pore has been replaced by this PNM of the unresolved cluster, and according to the method described in section 3.12.2, throats have been added to the PNM of the resolved porosity around it.

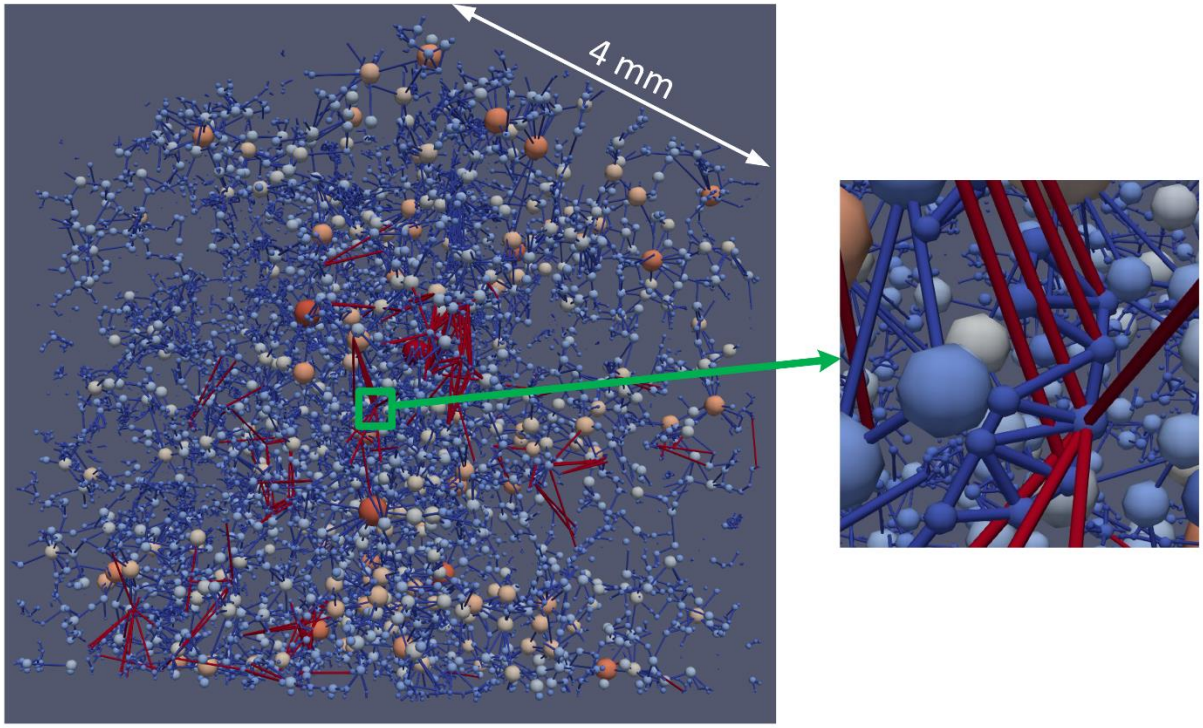

(a)

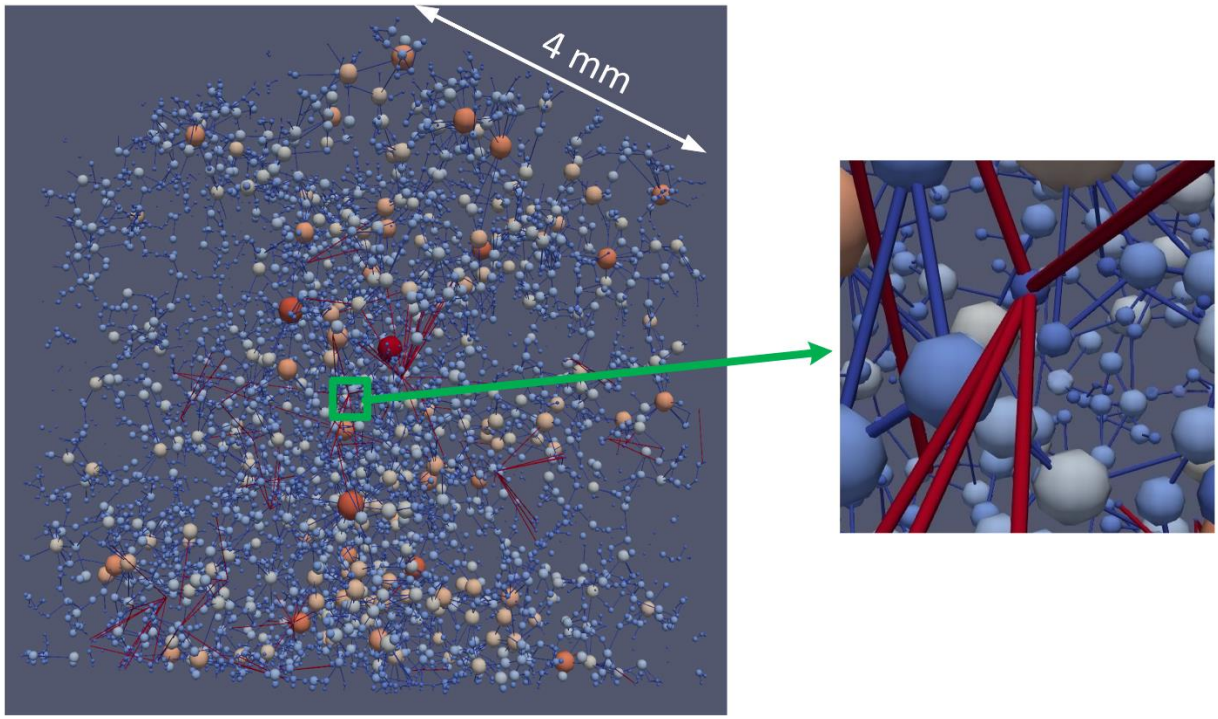

(b)

Figure 4-20 One realization of the (a) 3D multi-scale ANN-MPR regular PNM is shown along with the (b) upscaled 3D multi-scale PNM

Table 4-20 shows the computational cost of two ANN-MPR regular PNM and upscaled PNM modeling methods for calculating permeability on the selected realization. As it is known, the ANN-MPR regular PNM has more computational cost than the upscaled PNM modeling method. The ANN-MPR regular PNM consumes 25 GB of memory for this image to calculate the permeability value in 5 minutes, while the upscaled PNM modeling method requires 8 GB of memory to calculate the permeability value for this image in 3 minutes.

Table 4-20 Run time and memory consumption of regular and upscaled PNMs modeling methods in one realization for the ILS rock sample.

PNM	Run time (CPU-Second)	Memory consumption (GB)
Regular PNM	312	25
Upscaled PNM	190	8

Figure 4-21 shows the distribution of permeability values of reconstructed PNMs in all 10 realizations for both methods. As it is clear, the permeability values for the regular PNMs and the upscaled PNMs are almost equal to each other. The average of permeability values in multi-scale regular PNM is 252.4 mD, compared to 251.8 mD in multi-scale upscaled PNMs. This shows that the upscaling method for multi-scale PNM modeling is highly accurate for permeability prediction. The permeability in the upscaled PNM decreases because we remove a series of throats and pores from unresolved areas in the network. These removed throats have only a minor effect on permeability, as the throats connected to the base pore had the highest hydraulic conductance in these regions. However, their absence slightly lowers the permeability distribution in upscaled PNMs compared to regular PNMs. In the following, it will be shown how the upscaling PNM modeling method works in predicting the rest of the properties.

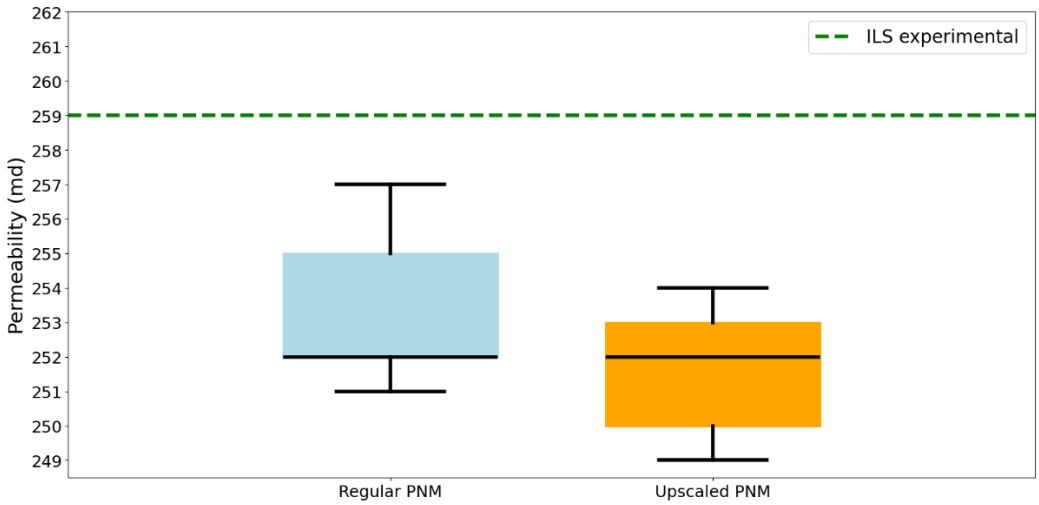

Figure 4-21 Permeability value distribution of the reconstructed regular PNM and upscaled PNM for the selected realization of the ILS rock sample

Figures 4-22 and 4-23 display the pore and throat size distribution in one reconstructed realization of the two PNMs. The average size of pores in regular PNM is 103.7 µm and in upscaled PNM is 107.5 µm. Moreover, the standard deviation in regular PNM method is 59.4 µm and in upscaled PNM method is 58.6 µm. Therefore, the upscaled PNM shows a lower percentage of small pores, while the regular PNM has fewer medium-sized pores compared to the upscaled PNM. This outcome was expected, as the upscaling process removed many small pores, reducing their

percentage in the upscaled multi-scale PNM. A similar trend is observed for throats. The average size of the throats in regular PNM is 69.0 µm and in upscaled PNM is 71.2 µm. Moreover, the standard deviation in regular PNM method is 47.5 µm and in upscaled PNM method is 47.4 µm. Therefore, the throat size distribution indicates fewer small size throats in the upscaled PNM, while the regular PNM has more medium-sized throats. However, as shown in Figure 4-21, the reported permeability of this network suggests that the removal of throats has been compensated by adding throats between large pores and base pores. These added throats have an equivalent hydraulic conductance that offsets the absence of medium-sized pores and throats.

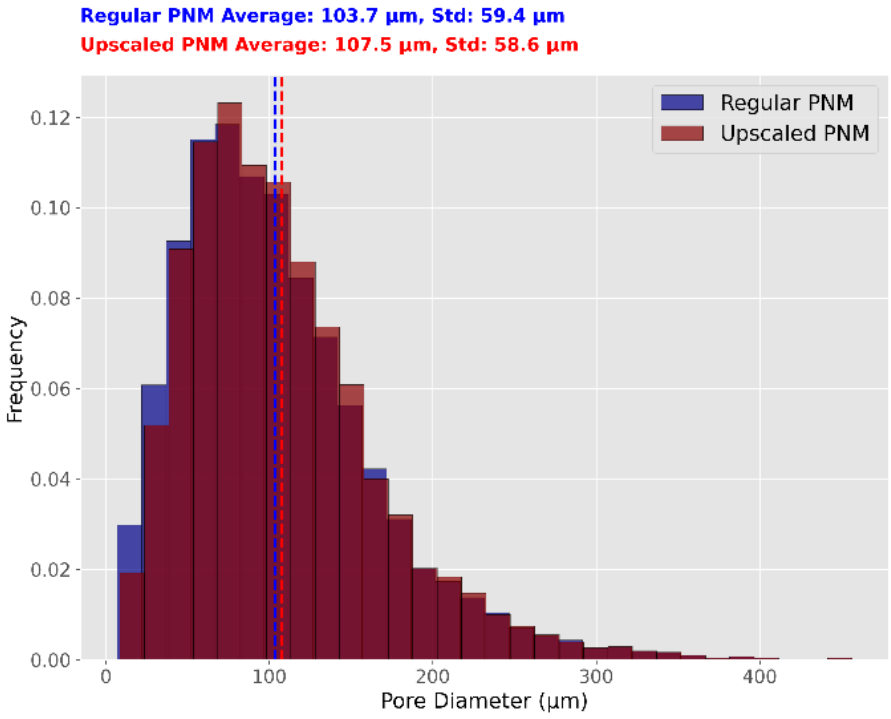

Figure 4-22 Pore size distribution of the reconstructed regular PNM and upscaled PNM for the selected realization of the ILS rock sample

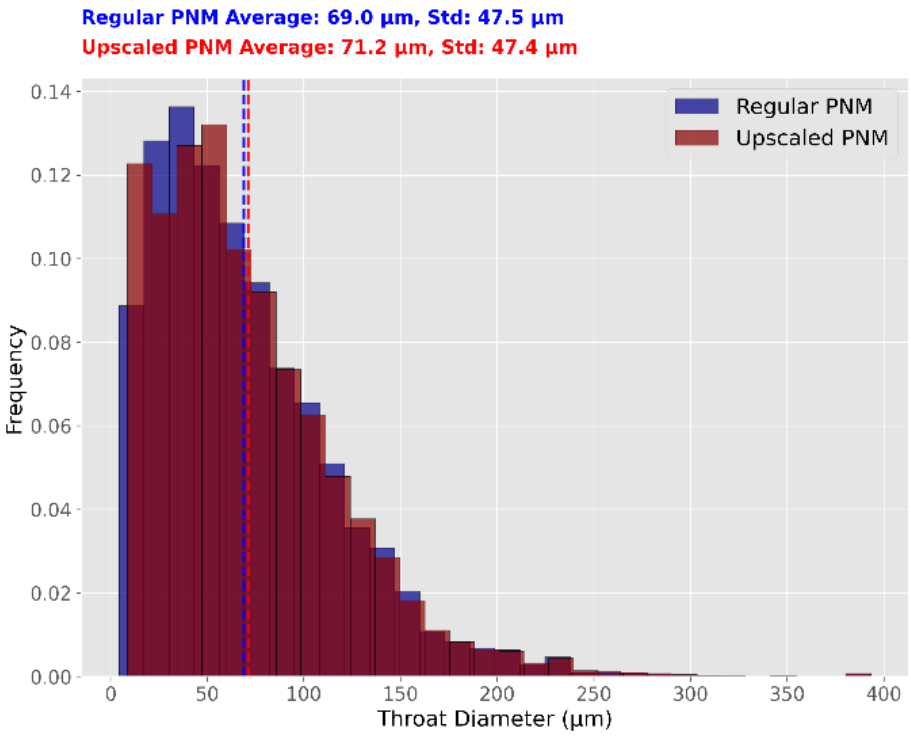

Figure 4-23 Throat size distribution of the reconstructed regular PNM and upscaled PNM for the selected realization of the ILS rock sample

Moreover, in Figure 4-24, the throat length distribution curve in the selected realization of the ANN-MPR regular PNM and upscaled PNM is displayed. In the upscaled PNM, the PNM within the unresolved area is removed. These networks primarily had throats shorter than 100 µm. Moreover, the throats connected to the base pore are relatively long, exceeding 100 µm. The average length of throats in regular PNM is 160.0 µm and less than the average length of throats in upscaled PNM which is 164.8 µm. Moreover, the standard deviation in regular PNM method is 83.0 µm and in upscaled PNM method is 81.3 µm. As a result, the figure shows a decrease in the distribution of throats shorter than 100 µm and a relative increase in the number of throats between 100 and 200 µm.

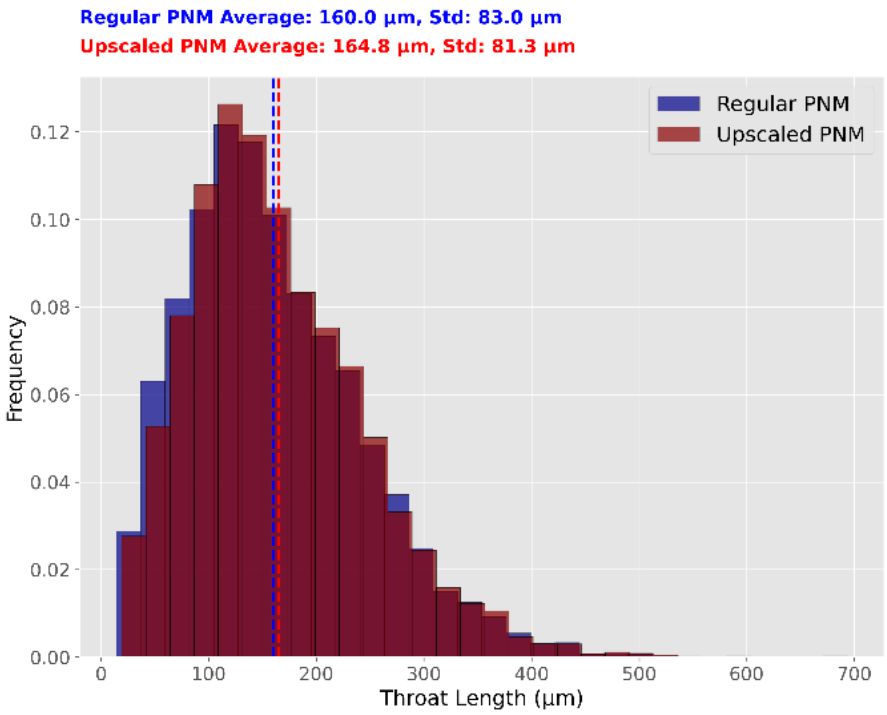

Figure 4-24 Throat length distribution of the reconstructed regular PNM and upscaled PNM for the selected realization of the ILS rock sample

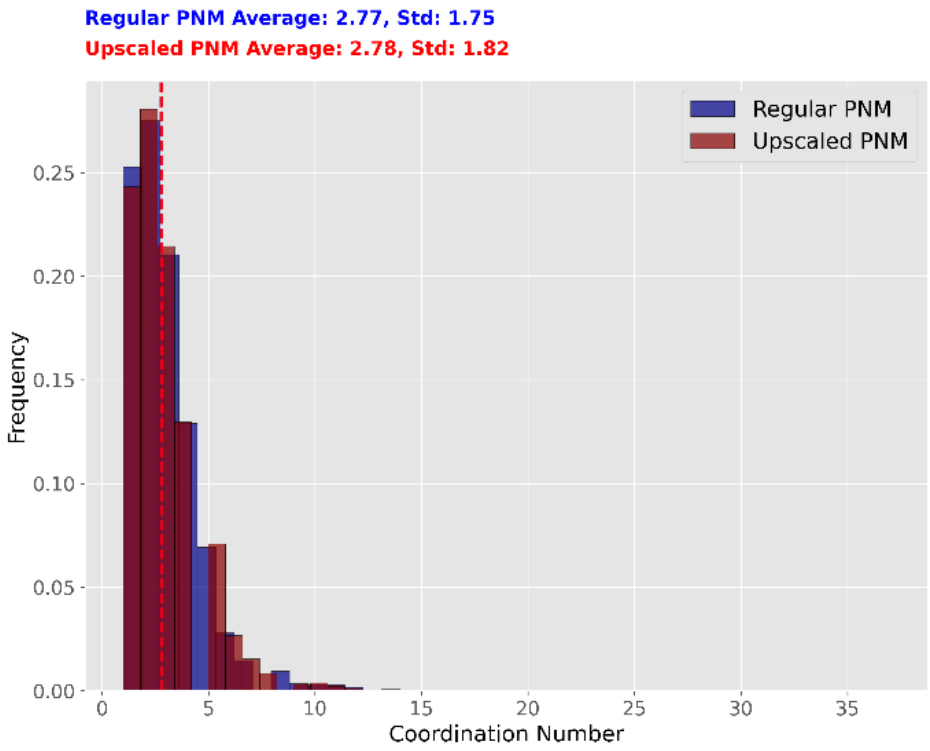

Figure 4-25 Coordination number distribution of the reconstructed regular PNM and upscaled PNM for the selected realization of the ILS rock sample

Moreover, Figure 4-25 shows the coordination number distribution in the selected realization of the ANN-MPR regular PNM and the upscaled PNM. The distribution in these two methods differs a bit. The average coordination number in regular PNM is 2.77 and is less than upscaled PNM which is 2.78. Moreover, the standard deviation is 1.75 in regular PNM and 1.82 in upscaled PNM. Removing a large number of pores and throats alters the coordination number of large pores connected to the PNMs in unresolved clusters. The figure reveals that the distribution of coordination numbers above 5 is higher in the upscaled PNM than in the regular PNM. This is because the pores in the unresolved area, which had coordination numbers less than 5, have been removed. Additionally, coordination numbers greater than 15 appear in the upscaled PNM, indicating that some base pores are connected to resolved pores with a large number of throats.

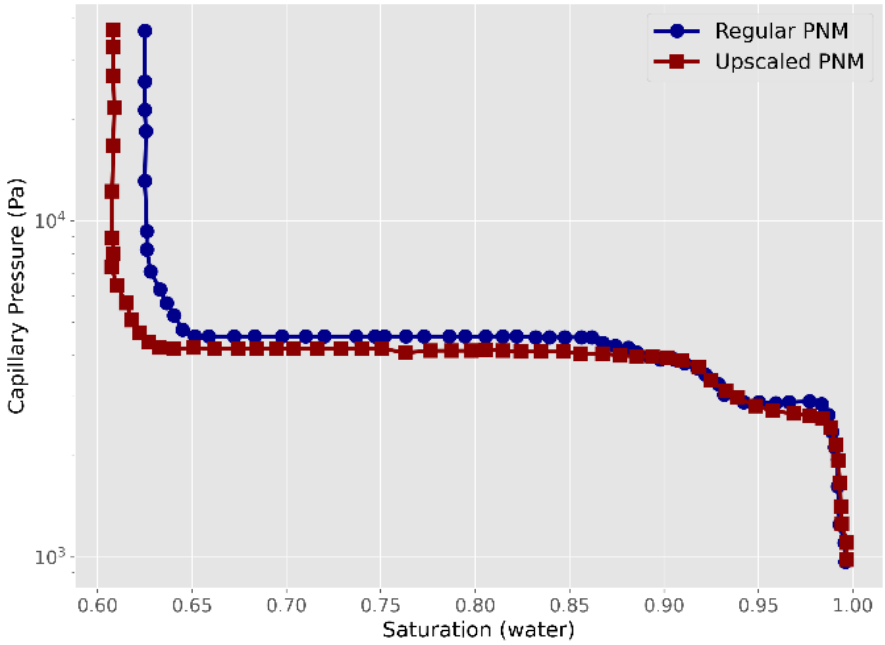

Figure 4-26 Capillary pressure curve of the reconstructed regular PNM and upscaled PNM for the selected realization of the ILS rock sample

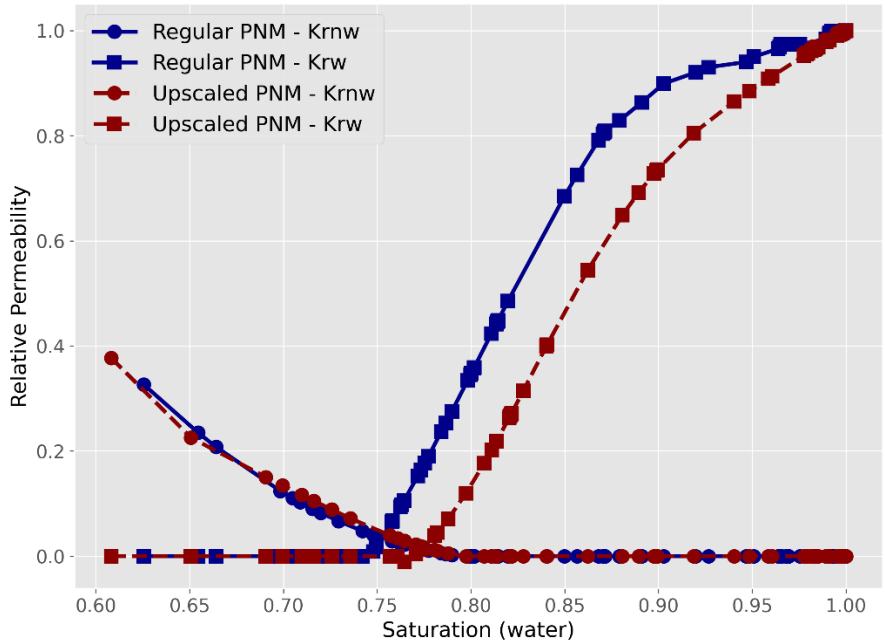

Figure 4-27 Relative permeability curve of the reconstructed regular PNM and upscaled PNM for the selected realization of the ILS rock sample

In addition, the capillary pressure and relative permeability curves for the selected realization for the regular and upscaled PNMs are shown in Figures 4-26 and 4-27. These simulations analyze water (w) and air (nw) phases, focusing on the drainage process. In Figure 4-26, the capillary pressure curve of the regular PNM sits slightly above that of the upscaled PNM. This difference occurs because the regular PNM includes more small pores and throats, slightly raising the curve. The regular PNM also has a higher irreducible water saturation (0.63) than the upscaled PNM (0.61). In both PNMs, fluid displacement begins in large pores. For this reason, the capillary pressure curves remain similar until reaching irreducible water saturation. However, regular PNM contains more small pores and throats and is more heterogeneous. This structure results in a shorter transition zone and slower water displacement by air.

In Figure 4-27, the water relative permeability curve is lower for the upscaled PNM than for the regular PNM. In contrast, the air relative permeability curve remains nearly the same in both PNMs. This suggests the regular PNM has higher effective permeability for water, allowing air to displace water more easily. This increased permeability in the regular PNM makes it easier for air to move water. Moreover, the same air relative permeability in both PNMs likely results from the new equivalent upscaled throats, enabling water in these throats to drain similarly to those in the regular network. Consequently, the regular PNM reaches its irreducible water saturation value sooner.

Chapter 5

Conclusion

Conclusion and future work

5.1 Conclusion

In this research, at first, two approaches of multi-scale image reconstruction were introduced. In the first multi-scale image reconstruction approach, a CCSIM Watershed-based Multi-scale Reconstruction (CWMR) approach was introduced for more efficient pore-scale modeling of heterogeneous rock samples. Additionally, a modified Wu et al. 2019 (Modified Wu et al.) reconstruction method was used for comparison. Both approaches reconstructed the multi-scale image by fusing images recorded at two different resolutions. First, in the CWMR method, the LR images were resampled based on the voxel size of the HR images. Then, the unresolved templates selected from the HR images by the multi-scale reconstruction approach were placed in the unresolved masks of the LR image. The unresolved templates of the LR images were segmented using the watershed segmentation algorithm. Finally, to validate the proposed algorithm, the petrophysical and morphological properties including porosity, absolute permeability, pore size distribution, and Euler number of the multi-scale reconstructed images were compared to the HR image properties of the rock sample.

The results showed that the multi-scale image reconstructed by the CWMR approach showed geometrical properties closer to the measured HR image properties. It efficiently preserved the connection between pores at various scales. Additionally, the proposed methodology was computationally faster and memory allocation for computations was lower than with the modified Wu et al. method for three reasons. First, the CWMR used smaller OL regions between unresolved templates in the LR image. Second, it replaced only the unresolved templates without using large unresolved regions, which require more pixels. Lastly, the CWMR used cropped HR images to select the best-match templates.

However, in the second multi-scale image reconstruction approach, an Octree CCSIM Watershed-based Multi-scale Reconstruction (OCWMR) approach was introduced for more efficient pore-scale modeling of heterogeneous rock samples with less computational cost. We compared the predicted single-phase (porosity, permeability) and two-phase (capillary pressure, relative permeability) properties obtained using the OCWMR and CWMR approaches. Our results indicate that the OCWMR approach yields properties that are closer to those derived from HR images. This

improvement is attributed to the use of optimal parameters in the watershed segmentation algorithm, leading to higher accuracy due to fewer unresolved templates.

The number of unresolved templates differed slightly between the OCWMR and CWMR approaches. This difference was crucial for aligning the properties closer to those of the HR image. The OCWMR approach resulted in fewer unresolved templates. Consequently, it added fewer isolated small pores and dead-end throats to the BS image. Conversely, it added fewer unnecessary small pores and throats to the EBC image compared to the CWMR approach. These changes led to a smaller permeability reduction and residual water saturation value in the BS rock. It also caused a smaller increase in permeability and larger residual water saturation value in the EBC rock. Additionally, the OCWMR approach significantly reduced computational cost and runtime compared to the CWMR approach. This was especially true for images with greater resolution differences between LR and HR images. Thus, the OCWMR approach is more efficient and practical for multi-scale image reconstruction in rock property prediction.

Moreover, in this research, two methods were introduced for the multi-scale PNM reconstruction. In the first method, a method called ANN Multi-scale PNM Reconstruction (ANN-MPR) was introduced. In this method, the PNM in the unresolved clusters is created by stochastically generating the PNM from the PNM extracted from the HR image. After generating the unresolved PNM, it is connected to the resolved PNM extracted from the LR image. For this connection, an ANN network was used, which was trained on the PNM extracted from the HR image. In the second method, a method called ANN Octree Multi-scale PNM Reconstruction (ANN-Octree-MPR) was introduced. In this method, unlike the ANN-MPR method, the PNM is extracted from the unresolved clusters separately. For this reason, at first, the multi-scale image is reconstructed using the OCWMR method, and then performed PNM extraction from the unresolved clusters. After this extraction, the unresolved PNM is connected to the resolved PNM using the ANN, similar to the process used in the ANN-MPR method.

For this purpose, we reconstructed various realizations of multi-scale PNM from ILS rock. After comparing the permeability values, we found that the permeability obtained using the ANN-MPR method closely matched the experimental permeability of the rock. This indicates that the ANN effectively connected the two scales. Additionally, the ANN-Octree-MPR method produced similar results to the ANN-MPR method, demonstrating its accuracy. The key advantage of the

ANN-Octree-MPR method, however, was its ability to reduce memory consumption during the reconstruction process.

To reduce the computational cost of calculating various properties on the multi-scale images and multi-scale PNMs, two methods for multi-scale modeling on images and PNMs were introduced. The first method, designed for multi-scale image reconstruction, calculates permeability values for each unresolved cluster separately. It then applies these permeability values to the governing flow equations on the LR image. By comparing the results of this method with the normal method of calculating properties on the image, the accuracy of this method was confirmed. The most significant advantage of this method over the standard approach is its reduced computational cost. Moreover, the proposed method for multi-scale PNM reconstruction performs modeling by taking a base pore for each unresolved cluster and connecting it to the resolved pores of the LR image. Different results were also calculated on these upscaled networks and had a good accuracy with the reconstructed ANN-MPR regular PNM. As expected, this method also caused a significant reduction in the computational cost for calculating various properties on the multi-scale PNMs.

5.2 Future work

- It is possible to reconstruct the images and the PNMs on more scales. For this purpose, it is necessary to prepare different images in different resolutions of the heterogeneous rocks.
- The described reconstruction methods can be applied to fractured rocks, allowing for the examination of different parameters specific to these types of rocks.
- Octree structure can be changed in such a way that there is no need to resampling the images for the multi-scale reconstruction of the images and the PNM and the accuracy of the modeling is higher.
- Octree structure can be improved to combine images of different resolutions.
- Multi-scale modeling on images can performed directly on the Octree structure. For this purpose, it is necessary to develop a code that can solve the governing flow equations on the Octree structure.
- It is possible to create a code that not only solves flow equations but also implements reactive transport equations on the Octree structure, significantly reducing the computational cost of solving these equations.

References

1. Blunt, M.J., et al., *Pore-scale imaging and modelling.* Advances in Water resources, 2013. **51**: p. 197-216.
2. Blunt, M.J., et al., *Detailed physics, predictive capabilities and macroscopic consequences for pore-network models of multiphase flow.* Advances in Water Resources, 2002. **25**(8-12): p. 1069-1089.
3. Sharqawy, M.H., *Construction of pore network models for Berea and Fontainebleau sandstones using non-linear programing and optimization techniques.* Advances in Water Resources, 2016. **98**: p. 198-210.
4. Aghaei, A. and M. Piri, *Direct pore-to-core up-scaling of displacement processes: Dynamic pore network modeling and experimentation.* Journal of hydrology, 2015. **522**: p. 488-509.
5. Bultreys, T., et al., *Investigating the relative permeability behavior of microporosity-rich carbonates and tight sandstones with multiscale pore network models.* Journal of Geophysical Research: Solid Earth, 2016. **121**(11): p. 7929-7945.
6. Ramandi, H.L., et al., *Impact of dissolution of syngenetic and epigenetic minerals on coal permeability.* Chemical Geology, 2018. **486**: p. 31-39.
7. Sadeghnejad, S., M. Ashrafizadeh, and M. Nourani, *Improved oil recovery by gel technology: Water shutoff and conformance control*, in *Chemical Methods*. 2022, Elsevier. p. 249-312.
8. Tahmasebi, P ,.M. Sahimi, and J. Caers, *MS-CCSIM: accelerating pattern-based geostatistical simulation of categorical variables using a multi-scale search in Fourier space.* Computers & Geosciences, 2014. **67**: p. 75-88.
9. Wu, Y., et al., *Multiscale modeling of shale samples based on low-and high-resolution images.* Marine and Petroleum Geology, 2019. **109**: p. 9-21.
10. Bagheri, M., et al., *Direct pore-scale simulation of the effect of capillary number and gas compressibility on cyclic underground hydrogen storage & production in heterogeneous aquifers.* Advances in Water Resources, 2023. **181**: p. 104547.
11. Esfandi, T., S. Sadeghnejad, and A. Jafari, *Effect of reservoir heterogeneity on well placement prediction in CO2-EOR projects using machine learning surrogate models* :

Benchmarking of boosting-based algorithms. Geoenergy Science and Engineering, 2024. **233**: p. 212564.

12. Karsanina, M.V., et al., *Enhancing image resolution of soils by stochastic multiscale image fusion.* Geoderma, 2018. **314**: p. 138-145.
13. Khaled, A.-R .and K. Vafai, *The role of porous media in modeling flow and heat transfer in biological tissues.* International Journal of Heat and Mass Transfer, 2003. **46**(26): p. 4989-5003.
14. Qin, Z., M. Arshadi, and M. Piri, *Near-miscible supercritical CO2 injection in oil-wet carbonate: A pore-scale experimental investigation of wettability state and three-phase flow behavior.* Advances in Water Resources, 2021. **158**: p. 104057.
15. Agrawal, P., et al., *Evolution of pore-shape and its impact on pore conductivity during CO2 injection in calcite: Single pore simulations and microfluidic experiments.* Advances in Water Resources, 2020. **136**: p. 103480.
16. Cai, J., et al., *Shale gas transport model in 3D fractal porous media with variable pore sizes.* Marine and Petroleum Geology, 2018. **98**: p. 437-447.
17. Song, W., et al., *Multiscale image-based fractal characteristic of shale pore structure with implication to accurate prediction of gas permeability.* Fuel, 2019. **241**: p. 522-532.
18. Tahmasebi, P., *Nanoscale and multiresolution models for shale samples.* Fuel, 2018. **217**: p. 218-225.
19. Zhao, P., et al., *Multifractal analysis of pore structure of Middle Bakken formation using low temperature N2 adsorption and NMR measurements.* Journal of Petroleum Science and Engineering, 2 :176 .019p. 312-320.
20. Moslemipour, A. and S. Sadeghnejad, *Dual-scale pore network reconstruction of vugular carbonates using multi-scale imaging techniques.* Advances in Water Resources, 2021. **147**: p. 103795.
21. Sadeghnejad, S., F. Enzmann, and M. Kersten, *Digital rock physics, chemistry, and biology: challenges and prospects of pore-scale modelling approach.* Applied Geochemistry, 2021. **131**: p. 105028.
22. Sadeghnejad, S. and J. Gostick, *Multiscale reconstruction of vuggy carbonates by pore-network modeling and image-based technique.* SPE Journal, 2020. **25**(01): p. 253-267.

23. Jacob, A., et al., *Analysis of variance of porosity and heterogeneity of permeability at the pore scale.* Transport in Porous Media, 2019. **130**(3): p. 867-887.
24. Jiang, Z., et al ,.*Stochastic pore network generation from 3D rock images.* Transport in porous media, 2012. **94**: p. 571-593.
25. Mehmani, Y. and K. Xu, *Capillary equilibration of trapped ganglia in porous media: A pore-network modeling approach.* Advances in Water Resources, 2022. **166**: p. 104223.
26. Feng, X., et al., *Resolution effect on image-based conventional and tight sandstone pore space reconstructions: origins and strategies.* Journal of Hydrology, 2020. **586**: p. 124856.
27. Huang, J., L. Wang, and X. Liu, *Lattice Boltzmann method for solute transport in dual-permeability media.* Journal of Hydrology, 2023. **619**: p. 129339.
28. Jivkov, A.P., et al., *A novel architecture for pore network modelling with applications to permeability of porous media.* Journal of Hydrology :486 .2013 ,p. 246-258.
29. Liu, Y., et al., *Effects of grain shape and packing pattern on spontaneous imbibition under different boundary conditions: Pore-scale simulation.* Journal of Hydrology, 2022. **607**: p. 127484.
30. McClure, J.E., et al., *Geometric state function for two-fluid flow in porous media.* Physical Review Fluids, 2018. **3**(8): p. 084306.
31. McClure, J.E., et al., *Modeling geometric state for fluids in porous media: Evolution of the euler characteristic.* Transport in Porous Media, 2020. **133**: p.250-229 .
32. Mehmani, A., R. Verma, and M. Prodanović, *Pore-scale modeling of carbonates.* Marine and Petroleum Geology, 2020. **114**: p. 104141.
33. Moslemipour, A., et al., *Pore network extraction from multiscale images: an efficient approach based on artificial neural network*.
34. Raeini, A.Q., et al., *Validating the generalized pore network model using micro-CT images of two-phase flow.* Transport in Porous Media, 2019. **130**(2): p. 405-424.
35. Schlüter, S., et al., *Pore-scale displacement mechanisms as a source of hysteresis for two-phase flow in porous media.* Water Resources Research, 2016. **52**(3): p. 2194-2205.
36. Zhao, Z. and X.-P. Zhou, *Pore-scale diffusivity and permeability evaluations in porous geomaterials using multi-types pore-structure analysis and X-μCT imaging.* Journal of Hydrology, 2022. **615**: p. 128704.

37. Gostick, J., et al., *OpenPNM: a pore network modeling package.* Computing in Science & Engineering, 2016. **18**(4): p. 60-74.
38. Lindquist, W.B., et al., *Medial axis analysis of void structure in three-dimensional tomographic images of porous media.* Journal of Geophysical Research: Solid Earth, 1996. **101**(B4): p. 8297-8310.
39. Silin, D. and T. Patzek, *Pore space morphology analysis using maximal inscribed spheres.* Physica A: Statistical mechanics and its applications, 2006. **371**(2): p. 336-360.
40. de Vries, E.T., A. Raoof, and M.T. van Genuchten, *Multiscale modelling of dual-porosity porous media; a computational pore-scale study for flow and solute transport.* Advances in water resources, 2 :105 .017p. 82-95.
41. Prodanović, M., W. Lindquist, and R. Seright, *3D image-based characterization of fluid displacement in a Berea core.* Advances in Water Resources, 2007. **30**(2): p. 214-226.
42. Yan, P., et al., *Multiscale reconstruction of porous media based on multiple dictionaries learning.* Computers & Geosciences, 2023: p. 105356.
43. Zhang, L., et al., *A hybrid pore-network-continuum modeling framework for flow and transport in 3D digital images of porous media.* Advances in Water Resources, 2024 :p. 104753.
44. Li, H., P.-E. Chen, and Y. Jiao, *Accurate reconstruction of porous materials via stochastic fusion of limited bimodal microstructural data.* Transport in Porous Media, 2018. **125**(1): p. 5-22.
45. Sadeghnejad, S., F. Enzmann, and M. Kersten ,*Numerical simulation of particle retention mechanisms at the sub-pore scale.* Transport in Porous Media, 2022. **145**(1): p. 127-151.
46. Hassannayebi, N., et al., *Relationship between microbial growth and hydraulic properties at the sub-pore scale.* Transport in porous media, 2021. **139**: p. 579-593.
47. Guo, F.-q., et al., *A spherical harmonic-random field coupled method for efficient reconstruction of CT-image based 3D aggregates with controllable multiscale morphology.* Computer Methods in Applied Mechanics and Engineering, 2023. **406**: p. 115901.
48. Huang, T., et al., *A novel method for multiscale digital core reconstruction based on regional superposition algorithm.* Journal of Petroleum Science and Engineering, 2022. **212**: p. 110302.

49. Lin, W., et al., *Multiscale digital porous rock reconstruction using template matching.* Water Resources Research, 2019. **55**(8): p. 6911-6922.
50. Ruspini, L., et al., *Multiscale digital rock analysis for complex rocks.* Transport in Porous Media, 2021. **139**(2): p. 301-325.
51. Zhang, W., L. Song, and J. Li, *Efficient 3D reconstruction of random heterogeneous media via random process theory and stochastic reconstruction procedure.* Computer Methods in Applied Mechanics and Engineering, 2019. **354**: p. 1-15.
52. Fu, J., et al., *Stochastic reconstruction of 3D microstructures from 2D cross-sectional images using machine learning-based characterization.* Computer Methods in Applied Mechanics and Engineering, 2022. **390**: p. 114532.
53. Guan, K.M., et al., *Reconstructing porous media using generative flow networks.* Computers & Geosciences, 2021. **156**: p. 104905.
54. Mosser, L., O. Dubrule, and M.J. Blunt, *Reconstruction of three-dimensional porous media using generative adversarial neural networks.* Physical Review E, 2017. **96**(4): p. 043309.
55. Shams, R., et al., *Coupled generative adversarial and auto-encoder neural networks to reconstruct three-dimensional multi-scale porous media.* Journal of Petroleum Science and Engineering, 2020. **186**: p. 106794.
56. Wang, Y., et al., *CT-image of rock samples super resolution using 3D convolutional neural network.* Computers & Geosciences, 2019. **133**: p. 104314.
57. Xia, P., H. Bai, and T. Zhang, *Multi-scale reconstruction of porous media based on progressively growing generative adversarial networks.* Stochastic Environmental Research and Risk Assessment, 2022: p. 1-21.
58. Yang, Y., et al., *Multi-scale reconstruction of porous media from low-resolution core images using conditional generative adversarial networks.* Journal of Natural Gas Science and Engineering, 2022. **99**: p. 104411.
59. Zhang, T., et al., *A 3D reconstruction method of porous media based on improved WGAN-GP.* Computers & Geosciences, 2022. **165**: p. 105151.
60. Gerke, K.M., M.V. Karsanina, and D. Mallants, *Universal stochastic multiscale image fusion: an example application for shale rock.* Scientific reports, 2015. **5**(1): p. 1-12.

61. Zhao, T., et al., *Permeability prediction of numerical reconstructed multiscale tight porous media using the representative elementary volume scale lattice Boltzmann method.* International Journal of Heat and Mass Transfer, 2018. **118**: p. 368-377.
62. Okabe, H. and M.J. Blunt, *Pore space reconstruction of vuggy carbonates using microtomography and multiple-point statistics.* Water Resources Research, 2007. **43**.(12)
63. Ji, L., et al., *A multiscale reconstructing method for shale based on SEM image and experiment data.* Journal of Petroleum Science and Engineering, 2019. **179**: p. 586-599.
64. Tahmasebi, P., *HYPPS: A hybrid geostatistical modeling algorithm for subsurface modeling.* Water Resources Research, 2017. **53**(7): p. 5980-5997.
65. Tahmasebi, P., F. Javadpour, and M. Sahimi, *Multiscale and multiresolution modeling of shales and their flow and morphological properties.* Scientific reports, 2015. **5**(1): p. 1-11.
66. Tahmasebi, P., F. Javadpour, and M. Sahimi, *Three-dimensional stochastic characterization of shale SEM images.* Transport in Porous Media, 2015. **110**: p. 521-531.
67. Tahmasebi, P., et al., *Multiscale study for stochastic characterization of shale samples.* Advances in Water Resources, 2016. **89**: p. 91-103.
68. Yan, P., et al., *Multiscale reconstruction of porous media based on multiple dictionaries learning.* arXiv preprint arXiv:2205.08278, 2022.
69. Li, X., et al., *Three-dimensional multiscale fusion for porous media on microtomography images of different resolutions.* Physical Review E, 2020. **101**(5): p. 053308.
70. Wang, Y., et al., *Three-dimensional porous structure reconstruction based on structural local similarity via sparse representation on micro-computed-tomography images.* Physical Review E, 2018. **98**(4): p. 043310.
71. Jiang, Z., et al., *Representation of multiscale heterogeneity via multiscale pore networks.* Water resources research, 2013. **49**(9): p. 5437-5449.
72. Prodanović, M., A. Mehmani, and A.P .Sheppard, *Imaged-based multiscale network modelling of microporosity in carbonates.* Geological Society, London, Special Publications, 2015. **406**(1): p. 95-113.
73. Bultreys, T., L. Van Hoorebeke, and V. Cnudde, *Multi-scale, micro-computed tomography-based pore network models to simulate drainage in heterogeneous rocks.* Advances in Water resources, 2015. **78**: p. 36-49.

74. Bultreys, T., et al. *A multi-scale, image-based pore network modeling approach to simulate two-phase flow in heterogeneous rocks*. in *2015 International symposium of the Society of Core Analysts (SCA 2015)*. 2015. Society of Core Analysts (SCA).
75. Alqahtani, N., et al., *Machine learning for predicting properties of porous media from 2d X-ray images.* Journal of Petroleum Science and Engineering, 2020. **184**: p. 106514.
76. Alqahtani, N., R.T. Armstrong, and P. Mostaghimi. *Deep learning convolutional neural networks to predict porous media properties*. in *SPE Asia Pacific oil and gas conference and exhibition*. 2018. OnePetro.
77. Rabbani, A. and M. Babaei, *Hybrid pore-network and lattice-Boltzmann permeability modelling accelerated by machine learning.* Advances in water resources, 2019. **126**: p. 116-128.
78. Sudakov, O., E. Burnaev, and D. Koroteev, *Driving digital rock towards machine learning* :*Predicting permeability with gradient boosting and deep neural networks.* Computers & geosciences, 2019. **127**: p. 91-98.
79. Liu, S., et al., *Application of neural networks in multiphase flow through porous media: Predicting capillary pressure and relative permeability curves.* Journal of Petroleum Science and Engineering, 2019. **180**: p. 445-455.
80. Bryant, S., C. Cade, and D. Mellor, *Permeability prediction from geologic models.* AAPG bulletin, 1993. **77**(8): p. 1338-1350.
81. Finney, J.L., *Random packings and the structure of the liquid state*. 1968, Birkbeck (University of London).
82. Bakke, S. and P.-E. Øren, *3-D pore-scale modelling of sandstones and flow simulations in the pore networks.* Spe Journal, 1997. **2**(02): p. 136-149.
83. Øren, P.-E. and S. Bakke ,*Process based reconstruction of sandstones and prediction of transport properties.* Transport in porous media, 2002. **46**(2): p. 311-343.
84. Sun, Q., et al., *Structural regeneration of fracture-vug network in naturally fractured vuggy reservoirs.* Journal of Petroleum Science and Engineering, 2018. **165**: p. 28-41.
85. Feng, J., et al., *An end-to-end three-dimensional reconstruction framework of porous media from a single two-dimensional image based on deep learning.* Computer Methods in Applied Mechanics and Engineering, 2020. **368**: p. 113043.

86. Li, Z., et al., *Sparse representation-based volumetric super-resolution algorithm for 3D CT images of reservoir rocks.* Journal of Applied Geophysics, 2017. **144**: p. 69-77.
87. Schlüter, S., et al., *Image processing of multiphase images obtained via X-ray microtomography: a review.* Water Resources Research, 2014. **50**(4): p. 3615-3639.
88. Yi, Z., et al., *Pore network extraction from pore space images of various porous media systems.* Water Resources Research, 2017. **53** :(4)p. 3424-3445.
89. Park, S.C., M.K. Park, and M.G. Kang, *Super-resolution image reconstruction: a technical overview.* IEEE signal processing magazine, 2003. **20**(3): p. 21-36.
90. Sun, J., Z. Xu, and H.-Y. Shum. *Image super-resolution using gradient profile prior*. in *2008 IEEE Conference on Computer Vision and Pattern Recognition*. 2008. IEEE.
91. Yan, Q., et al., *Single image superresolution based on gradient profile sharpness.* IEEE Transactions on Image Processing, 2015. **24**(10): p. 3187-3202.
92. Yang, J ,.et al., *Image super-resolution via sparse representation.* IEEE transactions on image processing, 2010. **19**(11): p. 2861-2873.
93. Yang, J., et al. *Image super-resolution as sparse representation of raw image patches*. in *2008 IEEE conference on computer vision and pattern recognition*. 2008. IEEE.
94. Da Wang, Y., R.T. Armstrong, and P. Mostaghimi, *Enhancing resolution of digital rock images with super resolution convolutional neural networks.* Journal of Petroleum Science and Engineering, 2019. **182**: p. 106.261
95. Niu, Y., et al., *An innovative application of generative adversarial networks for physically accurate rock images with an unprecedented field of view.* Geophysical Research Letters, 2020. **47**(23): p. e2020GL089029.
96. Wang, Y.D., R.T. Armstrong, and P. Mostaghimi, *Boosting resolution and recovering texture of 2D and 3D micro-CT images with deep learning.* Water Resources Research, 2020. **56**(1): p. e2019WR026052.
97. Su, C., et al., *Rock classification in petrographic thin section images based on concatenated convolutional neural networks.* Earth Science Informatics, 2020. **13**(4): p. 1477-1484.
98. Dong, C., et al., *Image super-resolution using deep convolutional networks.* IEEE transactions on pattern analysis and machine intelligence, 2015. **38**(2): p.307-295 .

99. Zhu, J.-Y., et al. *Unpaired image-to-image translation using cycle-consistent adversarial networks*. in *Proceedings of the IEEE international conference on computer vision*. 2017.
100. Dosovitskiy, A. and T. Brox, *Generating images with perceptual similarity metrics based on deep networks.* Advances in neural information processing systems, 2016. **29**: p. 658-666.
101. Johnson, J., A. Alahi, and L. Fei-Fei. *Perceptual losses for real-time style transfer and super-resolution*. in *European conference on computer vision*. 2016. Springer.
102. Ledig, C., et al. *Photo-realistic single image super-resolution using a generative adversarial network*. in *Proceedings of the IEEE conference on computer vision and pattern recognition*. 2017.
103. Yu, J., et al ,.*Wide activation for efficient and accurate image super-resolution.* arXiv preprint arXiv:1808.08718, 2018.
104. Da Wang, Y., R. Armstrong, and P. Mostaghimi, *Super resolution convolutional neural network models for enhancing resolution of rock micro-ct images.* arXiv preprint arXiv:1904.07470, 2019.
105. Janssens, N., M. Huysmans, and R. Swennen, *Computed tomography 3D super-resolution with generative adversarial neural networks: implications on unsaturated and two-phase fluid flow.* Materials, 2020. **13** :(6)p. 1397.
106. Da Wang, Y., et al., *Physical accuracy of deep neural networks for 2D and 3D multi-mineral segmentation of rock micro-CT images.* arXiv preprint arXiv:2002.05322, 2020.
107. Niu, Y., et al., *Digital rock segmentation for petrophysical analysis with reduced user bias using convolutional neural networks.* Water Resources Research, 2020. **56**(2): p. e2019WR026597.
108. Varfolomeev, I., I. Yakimchuk, and I. Safonov, *An application of deep neural networks for segmentation of microtomographic images of rock samples.* Computers, 2019. **8**(4): p. 72.
109. Bultreys, T., W. De Boever, and V. Cnudde, *Imaging and image-based fluid transport modeling at the pore scale in geological materials: A practical introduction to the current state-of-the-art.* Earth-Science Reviews, 2016. **155**: p. 93-128.
110. Cnudde, V. and M.N. Boone, *High-resolution X-ray computed tomography in geosciences: A review of the current technology and applications.* Earth-Science Reviews, 2013. **123**: p. 1-17.

111. Hébert, V., et al. *Digital core repository coupled with machine learning as a tool to classify and assess petrophysical rock properties*. in *E3S Web of Conferences*. 2020. EDP Sciences.
112. Jackins, C.L. and S.L. Tanimoto, *Oct-trees and their use in representing three-dimensional objects.* Computer Graphics and Image Processing, 1980. **14**(3): p. 249-270.
113. de Hoop, S., E. Jones, and D. Voskov, *Accurate geothermal and chemical dissolution simulation using adaptive mesh refinement on generic unstructured grids.* Advances in Water Resources, 2021. **154**: p. 103977.
114. Karimi-Fard, M. and L. Durlofsky. *Unstructured adaptive mesh refinement for flow in heterogeneous porous media*. in *ECMOR XIV-14th European conference on the mathematics of oil recovery*. 2014. European Association of Geoscientists & Engineers.
115. Bahrainian, S.S. and A.D. Dezfuli, *A geometry-based adaptive unstructured grid generation algorithm for complex geological media.* Computers & geosciences, 2014. **68**: p. 31-37.
116. Trangenstein, J.A., *Multi-scale iterative techniques and adaptive mesh refinement for flow in porous media.* Advances in Water Resources, 2002. **25**(8-12): p. 1175-1213.
117. Pau, G.S.H., et al., *An adaptive mesh refinement algorithm for compressible two-phase flow in porous media.* Computational Geosciences :16 .2012 ,p. 577-592.
118. Sammon, P.H. *Dynamic grid refinement and amalgamation for compositional simulation*. in *SPE Reservoir Simulation Conference?* 2003. SPE.
119. Christensen, J., et al. *Applications of dynamic gridding to thermal simulations*. in *SPE Western Regional Meeting*. 2004. SPE.
120. van Batenburg, D.W., et al. *Application of dynamic gridding techniques to IOR/EOR-processes*. in *SPE Reservoir Simulation Conference?* 2011. SPE.
121. Berrone, S., A. Borio, and F. Vicini, *Reliable a posteriori mesh adaptivity in discrete fracture network flow simulations.* Computer Methods in Applied Mechanics and Engineering, 2019. **354**: p. 904-931.
122. ; Available from: https://en.wikipedia.org/wiki/Octree.
123. Jayaraman, P.K., et al. *Quadtree convolutional neural networks*. in *Proceedings of the European Conference on Computer Vision (ECCV)*. 2018.
124. Wang, P.-S., et al., *O-cnn: Octree-based convolutional neural networks for 3d shape analysis.* ACM Transactions On Graphics (TOG), 2017. **36**(4): p. 1-11.

125. Ghadai, S., A. Jignasu, and A. Krishnamurthy, *Direct 3D printing of multi-level voxel models.* Additive Manufacturing, 2021. **40**: p. 101929.
126. Schwarz, M. and H.-P. Seidel, *Fast parallel surface and solid voxelization on GPUs.* ACM transactions on graphics (TOG), 2010. **29**(6): p. 1-10.
127. Churcher, P., et al. *Rock properties of Berea sandstone, Baker dolomite, and Indiana limestone*. in *SPE International Symposium on Oilfield Chemistry*. 1991. OnePetro.
128. Hashemi, L., M. Blunt, and H. Hajibeygi, *Pore-scale modelling and sensitivity analyses of hydrogen-brine multiphase flow in geological porous media.* Scientific reports, 2021. **11**(1): p. 1-13.
129. Thomson, P.-R., A. Aituar-Zhakupova, and S. Hier-Majumder, *Image segmentation and analysis of pore network geometry in two natural sandstones.* Frontiers in Earth Science, 2018. **6**: p. 58.
130. Xue, Y., et al., *Insights into Heterogeneity and Representative Elementary Volume of Vuggy Dolostones.* Energies, 2022. **15**(16): p. 5817.
131. Zhao, J., et al., *Simulation of quasi-static drainage displacement in porous media on pore-scale: Coupling lattice Boltzmann method and pore network model.* Journal of Hydrology, 2020. **588**: p. 125080.
132. Hupfer, S., *Spectral induced polarisation for an enhanced pore-space characterisation and analysis of dissolution processes of carbonate rocks*. 2020.
133. Maclay, R.W. and T.A. Small, *Carbonate geology and hydrology of the Edwards aquifer in the San Antonio area, Texas*. 1984, US Geological Survey.
134. Sadeghnejad, S., et al., *Minkowski functional evaluation of representative elementary volume of rock microtomography images at multiple resolutions.* Advances in Water Resources, 2023: p. 104501.
135. Moosmann, J., et al., *Time-lapse X-ray phase-contrast microtomography for in vivo imaging and analysis of morphogenesis.* Nature Protocols, 2014. **9**(2): p. 294-304.
136. Schneider, C.A., W.S. Rasband, and K.W. Eliceiri, *NIH Image to ImageJ: 25 years of image analysis.* Nature methods, 2012. **9**(7): p. 671-675.
137. Broesch, J.D., *Digital signal processing: instant access*. 2008: Elsevier.

138. Buades, A., B. Coll, and J.-M. Morel. *A non-local algorithm for image denoising*. in *2005 IEEE computer society conference on computer vision and pattern recognition (CVPR'05)*. 2005. Ieee.
139. Gonzalez, R.C ,.*Digital image processing*. 2009: Pearson education india.
140. Parsania, P. and P.V. Virparia, *A review: Image interpolation techniques for image scaling.* International Journal of Innovative Research in Computer and Communication Engineering, 2014. **2** :(12)p. 7409-7414.
141. Keys, R., *Cubic convolution interpolation for digital image processing.* IEEE transactions on acoustics, speech, and signal processing, 1981. **29**(6): p. 1153-1160.
142. Lekien, F. and J. Marsden, *Tricubic interpolation in three dimensions.* International Journal for Numerical Methods in Engineering, 2005. **63**(3): p. 455-471.
143. Reinhardt, M., et al., *Benchmarking conventional and machine learning segmentation techniques for digital rock physics analysis of fractured rocks.* Environmental Earth Sciences, 2022. **81**(3): p. 71.
144. Ronneberger, O., P. Fischer, and T. Brox. *U-net: Convolutional networks for biomedical image segmentation*. in *Medical Image Computing and Computer-Assisted Intervention–MICCAI 2015: 18th International Conference, Munich, Germany, October 5-9, 2015, Proceedings, Part III 18*. 2015. Springer.
145. Serra, J., *Image analysis and mathematical morphol-ogy.* (No Title), 1982.
146. Tahmasebi, P. and M. Sahimi, *Reconstruction of nonstationary disordered materials and media: Watershed transform and cross-correlation function.* Physical Review E, 2015. **91**(3): p. 032401.
147. Gostick, J.T., et al., *PoreSpy: A python toolkit for quantitative analysis of porous media images.* Journal of Open Source Software, 2019. **4**(37): p. 1296.
148. Tahmasebi, P., A. Hezarkhani, and M. Sahimi, *Multiple-point geostatistical modeling based on the cross-correlation functions.* Computational Geosciences, 2012. **16**(3): p. 779-797.
149. Zhang, J., et al., *Direct point-cloud-based numerical analysis using octree meshes.* Computers & Structures, 2023. **289**: p. 107175.
150. Gostick, J.T., *Versatile and efficient pore network extraction method using marker-based watershed segmentation.* Physical Review E, 2017. **96**(2): p. 023307.

151. Serra, J., *Image analysis and mathematical morphology*. 1983: Academic Press, Inc.
152. Al-Kharusi, A.S. and M.J. Blunt, *Network extraction from sandstone and carbonate pore space images.* Journal of petroleum science and engineering, 2007. **56**(4): p. 219-231.
153. Dong, H. and M.J. Blunt, *Pore-network extraction from micro-computerized-tomography images.* Physical Review E—Statistical, Nonlinear, and Soft Matter Physics, 2009. **80**(3): p. 036307.
154. Linden, S., A. Wiegmann, and H. Hagen, *The LIR space partitioning system applied to the Stokes equations.* Graphical Models, 2015. **82**: p. 58-66.
155. Linden, S., H. Hagen, and A. Wiegmann. *The LIR space partitioning system applied to Cartesian grids*. in *International Conference on Mathematical Methods for Curves and Surfaces*. 2012. Springer.
156. Moslemipour, A., et al., *Image-Based Multi-scale Reconstruction of Unresolved Microporosity in 3D Heterogeneous Rock Digital Twins Using Cross-Correlation Simulation and Watershed Algorithm.* Transport in Porous Media, 2024.
157. Mecke, K. and C. Arns, *Fluids in porous media: a morphometric approach.* Journal of Physics: Condensed Matter, 2005. **17**(9): p. S503.
158. Vogel, H.-J., U. Weller, and S. Schlüter, *Quantification of soil structure based on Minkowski functions.* Computers & Geosciences, 2010. **36** :(10)p. 1236-1245.
159. Scholz, C., et al., *Permeability of porous materials determined from the Euler characteristic.* Physical review letters, 2012. **109**(26): p. 264504.
160. Scholz, C., et al., *Direct relations between morphology and transport in Boolean models.* Physical Review E, 2015. **92**(4): p. 043023.
161. Armstrong, R.T., et al., *Porous media characterization using Minkowski functionals: Theories, applications and future directions.* Transport in Porous Media, 2019. **130**: p. 305-335.
162. Zhao, Y., *Estimating critical path analysis on digital topology of the connectivity of pore media.* Multimedia Tools and Applications, 2019. **78**: p. 1165-1180.
163. Slotte, P.A., C.F. Berg, and H.H. Khanamiri, *Predicting resistivity and permeability of porous media using Minkowski functionals.* Transport in Porous Media, 2020. **131**(2): p. 705-722.

164. Hansen, A., et al., *A statistical mechanics framework for immiscible and incompressible two-phase flow in porous media.* Advances in Water Resources, 2023. **171**: p. 104336.